Finite Size Effects in Platinum-group Metal Nanostructures

Shibesh Dutta

Examination Committee
Prof. dr. Andre Stesmans (Chair)
Prof. dr. ir. Wilfried Vandervorst (Supervisor)
dr. Christoph Adelmann (Co-supervisor - imec)
Prof. dr. Annelies Delabie
Prof. dr. ir. W.M.M. Kessels (TU Eindhoven)
Prof. dr. Kristiaan Temst
Prof. dr. André Vantomme

Dissertation presented in partial fulfillment of the requirements for the degree of Doctor of Science (PhD): Physics

October 2018

© 2018 KU Leuven – Faculty of Science
Uitgegeven in eigen beheer, Shibesh Dutta, Celestijnenlaan 200D, B-3001 Heverlee (Belgium)

Alle rechten voorbehouden. Niets uit deze uitgave mag worden vermenigvuldigd en/of openbaar gemaakt worden door middle van druk, fotokopie, microfilm, elektronisch of op welke andere wijze ok zonder voorafgaande schriftelijke toestemming van de uitgever.

All rights reserved. No part of the publication may be reproduced in any form by print, photoprint, microfilm, electronic or any other means without written permission from the publisher.

Acknowledgements

I have been fortunate; to be around people who know more than me, and who know better than me.

There are many who are owed gratitude. I'd rather be succinct, for words won't do justice. I would do my best to express in person to everyone.

To the examination committee – for the time invested on the manuscript and the defense. For the feedback that has indeed improved the quality of the manuscript by a notch. For probing the most fundamental aspects of the work. And for being most critical in their remarks and making me 'earn' my doctorate.

To imec – a young man only looks for an opportunity. Thank you, for providing me that opportunity.

To my promoter, Wilfried – you have always maintained high standards. You pushed me to directions I may not have otherwise explored. You have regularly challenged my ideas and my thinking. And for that, I am better today than I was yesterday.

To my advisor, Christoph – I consider myself fortunate. It's overwhelming to describe what I have learnt from you over the past half a decade. The best part of my PhD were our discussions, the times we worked together. I have received more than I could have asked for. I am happy I am graduating. In equal measures, I am at a loss. But I wish, it's turns out to be a 'small world'. Thank you, for all the time and the effort. Thank you, for being my 'guru'.

To lifelong teachers, Balakrishnan Shankar and Sundar Gopalan – for instilling in me the values that will become the guiding principles of my life.

To closest friends and dearest colleagues – Abhitosh, Alicija, Amey, Antony, Barkha, Benjamin, Christian, Claire, Davide, Dennis, Divya, Divya, Finub, Francesca, Giacomo, Gokul, Gouri-da, Goutham, Hari, Ivan, Janaki, Jehan, Job, Johan, Josephine, Juergen, Julien, Kathleen, Kirou, Kim, Kristof Moors, Krithika, Lucas, Manasi, Marc, Massimo, Manoj, Manoj, Maria, Mazhar, Michiel, Mikhail, Mitali-di, Mohit, Nadiia, Nicola, Nicolo, Nivesh, Olalla, Phalguni, Pierre, Prerna, Robert, Sadhish, Saranya, Sathish, Senthil, Shanish, Shreya, Siddharth, Silvia, Siva, Sofie, Somya, Sriram, Subhali, Sunil, Surajit, Surya, Susee, Sven, Sylvester, Tarun, Tom, Vamsi, Yoann, Zsolt

To Benjamin and Sruti – few are made like you. It's been a privilege.

To brothers – Anshul, Nivesh, Ujjal, and Vikas. Leuven would have been soulless without you.

To family – Mom, Dad, and Raja. Mom, you have always put the family above everything else. Dad, you have treated everyone with the respect and dignity they deserve. Raja, your relentless pursuit of your goal inspires me.

To you, Elisabetta. With you, words become redundant.

And finally, to the principle I try to live up to – "when the great scorer writes against your name, he sees not whether you have won or lost, but how you played the game..", paraphrased from *Alumnus Football* by Grantland Rice.

Abstract

Conductivity of nanostructures differ significantly from the bulk. One such manifestation is the resistivity scaling where the resistivity of metallic nanostructures increases drastically when the characteristic dimensions are reduced to the order of the carrier mean free path and is due to the additional scattering contributions from the interfaces and the grain boundaries. Though this phenomenon has been known for several decades, there is still no consensus over the relative importance of these scattering mechanisms in thin films and nanowires. Technologically, the increased resistivity has important implications: metallic nanowires are used as interconnect structures in microelectronic circuits and increased resistivity has led to problems such as higher latency, increased power consumption, more noise, and degraded reliability. Platinum-group metals have been proposed as promising candidates to replace the choice of metal, copper, however little is known about the scattering mechanisms in scaled structures of these metals.

This work aims to improve the current understanding of the scattering mechanisms in thin films (<30 nm) and nanowires (<100 nm^2 in cross-section area) of the platinum-group metals. The scattering mechanisms in thin platinum-group metals films are studied and compared to copper through semi-classical resistivity modeling using the Mayadas-Shatzkes (MS) model and complemented with extensive microstructural characterization. An adaptation of the MS model for thin films was proposed that can model the resistivity of nanowires. MS models for wires and thin films describe the experiments with a consistent set of parameters. For thin films, grain boundary scattering was established as the dominant scattering mechanism contributing to resistivity and assumes more importance for metals with higher melting points. However, resistivity is most sensitive to grain boundary scattering only when grain size becomes of the order of the mean free path but has little impact once the grain size becomes greater than a

factor of 4-5 of the mean free path. The choice of *cladding* on films is found to significantly alter the surface scattering behavior. A novel scheme was proposed which can be used to fabricate nanowires with sub-100 nm^2 in cross-section area. On examining the transport properties of Ru nanowires (quasi-one-dimensional metallic structures), grain boundary scattering was the dominant contributor to resistivity, except for very small cross-sectional areas where surface scattering contributes significantly due to a higher ratio of surface-to-volume. It is further understood that the resistivity was predominantly governed by the cross-sectional area of the nanowires and variations in aspect ratio (for a fixed cross-sectional area) have little impact. Furthermore, it was found that the mean free path is the single most critical parameter in determining the sensitivity of a metal to resistivity scaling. This results in a crossover where the resistivity of the platinum-group metals, though higher in bulk, become lower than that of copper at smaller dimensions. Finally, wafer-level reliability tests on ruthenium nanowires demonstrate the potential for robust reliability performance in interconnect structures.

Beknopte samenvatting

De geleidbaarheid van metalen nanostructuren verschilt significant van de geleidbaarheid van bulkmetalen. Meer bepaald neemt de resistiviteit van metalen nanostructuren sterk toe wanneer de karakteristieke afmetingen dalen tot in de orde van de vrije weglengte van de elektronen. Dit effect is te wijten aan het toenemend belang van verstrooiing aan de interfases en korrelgrenzen in deze nanostructuren. Alhoewel dit fenomeen reeds decennialang bekend is, is er tot op heden geen consensus omtrent het relatieve belang van de individuele verstrooiingsmechanismes in dunne filmen en nanodraden. De verhoogde resistiviteit van nanostructuren heeft echter belangrijke technologische gevolgen: metalen nanodraden worden gebruikt als geleiders in microelektronische schakelingen, en toenemende resistiviteit van deze geleiders leidt tot problemen zoals vertraagde signalen, toenemend stroomverbruik, verhoogde ruis, en een lagere betrouwbaarheid. Platinagroepmetalen zijn reeds voorgesteld als potentiële vervangers van het courant gebruikte koper, maar er is relatief weinig inzicht omtrent de verstrooiingsmechanismes in kleine structuren gemaakt van deze metalen.

Het doel van dit onderzoek is om het inzicht in verstrooiingsmechanismes in dunne filmen (<30 nm) en nanostructuren (<100 nm^2 in dwarsdoorsnede) van de platinagroepmetalen te verbeteren. De verstrooiingsmechanismes in dunne filmen van platinagroepmetalen worden bestudeerd en vergeleken met koper door middel van semiklassieke resistiviteitsmodellering aan de hand van het Mayadas-Shatzkesmodel (MS-model), alsmede een uitgebreide karakterisatie van de microstructuur. Dit onderzoek stelt een aanpassing van het MS-model voor dunne filmen voor, waardoor de resistiviteit van nanodraden beschreven kan worden. MS-modellen voor nanodraden en dunne filmen beschrijven hierbij de waarnemingen aan de hand van een consistente groep van parameters. In dunne filmen is korrelgrensverstrooiing het dominante verstrooiingsmechanisme dat bijdraagt tot de resistiviteit, en

het belang van dit mechanisme neemt toe met het smeltpunt van het metaal. Korrelgrensverstrooiing is echter enkel de dominante bijdrage tot resistiviteit wanneer de korrelgrootte vergelijkbaar is met de vrije weglengte van de elektronen, maar verliest aan belang wanneer de korrelgrootte meer dan 4-5 keer de vrije weglengte bedraagt. Oppervlakteverstrooiing van metalen filmen wordt sterk beïnvloed door de keus van bekleding. Dit werk stelt een nieuwe methode voor om nanodraden met een dwarsdoorsnede van minder dan 100 nm^2 te produceren. Een studie van de transporverschijnselen in Ru-nanodraden (quasi-eendimensionale metalen structuren) leert ons dat korrelgrensverstrooiing de dominante bijdrage tot resistiviteit levert, met uitzondering van structuren met een zeer kleine dwarsdoorsnede waar oppervlakteverstrooiing significant bijdraagt door een verhoogde oppervlakte-tot-volumeverhouding. De studie leert ons verder dat de resistiviteit van nanodraden voornamelijk bepaald wordt door de dwarsdoorsnede, terwijl variaties in de hoogte-breedteverhouding weinig impact hebben voor een gegeven vaste dwarsdoorsnede. Verder vormt de vrije weglengte de meest belangrijke parameter in het bepalen van de gevoeligheid van een gegeven metaal voor resistiviteitsschaling. Dit laatste fenomeen resulteert in een overgang, waarbij de resistiviteit van de platinagroepmetalen lager wordt dan die van koper voor kleine afmetingen, ondanks de hogere bulkresistiviteit. Ten slotte demonstreert dit werk het potentieel van ruthenium-nanodraden aan de hand van betrouwbaarheidstesten op waferschaal.

Abbreviations

AFM	: Atomic force microscopy
ALD	: Atomic layer deposition
BKM	: Best known method
DD	: Dual damascene
CMP	: Chemical mechanical polishing/planarization
DOE	: Design of experiment
DME	: Direct metal etch
EBECH Ru	: (ethylbenzyl) (1-ethyl-1,4-cyclohexadienyl) Ru(0)
EBSD	: Electron Backscattered Diffraction
EM	: Electromigration
FWHM	: Full width at half maximum
HAGB	: High angle grain boundary
IC	: Integrated circuit
IRDS	: International roadmap for devices and systems
ITRS	: International technology roadmap for semiconductors
LAGB	: Low angle grain boundary
MSE	: Mean sum of squared errors
PAS	: Positron annihilation spectroscopy
PVD	: Physical vapor deposition
PGM	: Platinum-group metals
RBS	: Rutherford backscattered spectroscopy
RMS	: Root mean square

SD	: Single damascene
SSE	: Sum of squared errors
TEM	: Transmission electron microscopy
ULSI	: Ultra large-scale integration
XRD	: X-Ray diffraction
XRR	: X-Ray reflectivity

List of Symbols

d	: Interplanar distance
ξ	: Lateral correlation length
e	: Electronic charge
E_p	: Potential energy of a barrier
E_{vf}	: Vacancy formation energy
E_{vm}	: Vacancy migration energy
f	: Roughness factor
g	: Linear (grain boundary) intercept length
h	: Film thickness
$\hbar$	: Reduced plank's constant
κ	: Dielectric constant
k_F	: Fermi wave-vector
l	: Characteristic length
λ_0	: Electron mean free path in bulk
λ_F	: Electron fermi wavelength
p	: Surface specularity parameter
p	: Momentum
m^*	: Effective mass
n	: Electron density
r	: Surface roughness
R	: Grain boundary reflection coefficient
ρ_{bulk}	: Bulk resistivity

ρ_{GB}	: Thin film resistivity due to grain boundaries from the Mayadas-Shatzkes model
ρ_{SS}	: Thin film resistivity from the Fuchs-Sondheimer model
s	: Standard deviation
s-parameter	: Line shape parameter
S	: Strength of the scattering plane
τ_0	: Scattering time
T_m	: Melting point
T_{recrys}	: Recrystallization temperature
v_F	: Fermi velocity
w_b	: Barrier width
Y	: Yield

Table of Contents

Abstract III

Abbreviations VII

List of symbols IX

1. Introduction **1**

1.1 Resistivity scaling 2
1.2 Interconnects 3
1.2.1 Copper and the platinum-group metals 6
1.3 Motivation 9
1.3.1 Problem statements 9
1.3.2 Research objectives 10
1.4 Outline 11

2. Finite Size Effects **13**

2.1 Scattering mechanisms 14
2.1.1 Surface scattering 14
2.1.2 Grain boundary scattering 20
2.1.3 Common approaches to resistivity modeling 29
2.2 Material properties & resistivity scaling 36
2.3 Chapter summary 39

3. Microstructure & Annealing Behavior 41

3.1 Nicrostructural transformations 42

3.1.1 Microstructure of thin Ruthenium films 44

3.2 Annealing behavior 49

3.2.1 Impact on stress evolution 53

3.2.2 Impact on electrical resistance 56

3.3 Chapter summary 58

4. Scattering Mechanisms in Thin Films 61

4.1 Material characterization 62

4.2 Semi-classical resistivity modeling 66

4.2.1 Linear grain boundary distance 68

4.2.2 Results and discussion 70

4.2.3 Comparison: ALD vs PVD Ru films 79

4.2.4 Relative contribution of scattering mechanisms 88

4.2.5 Influence of the mean free path 92

4.3 Chapter summary 94

5. Highly Scaled Ruthenium Nanowires 97

5.1 Fabrication scheme 99

5.2 Nanowire fabrication with reaction ion etching 101

5.2.1 Electrical characterization 102

5.2.2 Wafer-level reliability 105

5.3 Nanowire fabrication with ion beam etching 109

5.3.1 Electrical characterization 112

5.3.2 Resistivity modeling of Ruthenium nanowires 114

5.4 Chapter summary 121

6. Conclusion **123**

6.1 Outlook 127

Appendix A. Deposition and characterization techniques 131

Appendix B. Recrystallization temperature of ALD Ru 135

Appendix C. Electrical cross-section area of nanowires 137

Appendix D. Resistivity comparison of sub-100 nm^2 nanowires..................139

Bibliography 141

List of Publications..163

Chapter 1

Introduction

One of the important *(finite) size effects* in highly scaled structures is the phenomenon that the resistivity of a conductor increases strongly when the dimensions approach the mean free path of its charge carriers, and has been a topic of research for several decades, both from a fundamental as well as from an applied point of view. While the resistivity of bulk metals is dominated by phonon (and possibly impurity) scattering at room temperature, surface scattering can become dominant when the bulk structures are scaled significantly [1]–[3]. In addition, grain sizes (i.e., the mean linear distances between the grain boundaries) in polycrystalline films or wires have typically been found to decrease for decreasing film thickness or wire diameter, which leads to an increasing contribution of grain boundary scattering to the resistivity in such structures [4], [5]. Ultimately, when the structure size becomes of the order of a few angstroms, electron confinement effects might also alter the resistivity of metallic nanostructures [3], [6]–[10].

From an applied point of view, the understanding of the resistivity of metals in reduced dimensions is crucial since metallic nanowires form interconnect structures that are used in integrated microelectronic circuits. At present, the widths of scaled interconnect wires are of the order of 20 nm and are expected to reach dimensions below 10 nm in the next decade. At such dimensions, surface and grain boundary scattering in copper, the standard conductor material presently used in interconnects, dominate over phonon scattering resulting in resistivity much larger than in the bulk [11]–[15] (**Figure 1.1**) and leading to a deterioration of the interconnect properties [16]–[19]. In addition, copper-based interconnects require diffusion barriers

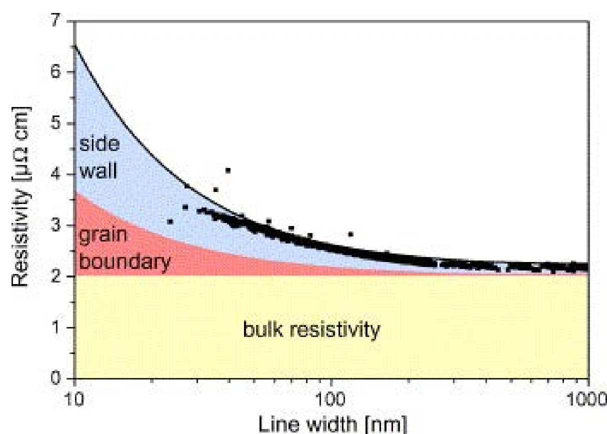

Figure 1.1 The increase in resistivity in copper interconnect lines as a function of decreasing linewidth. Contributions of bulk resistivity and electron scattering at the sidewalls (interfaces) and grain boundaries are indicated by the shaded area and the solid line as calculated by simulations using the Mayadas-Shatzkes model; data points are experimental values (Figure reproduced from [21]).

and adhesion liners to ensure their reliability. Since the resistivity of barriers and liners is typically much higher than that of copper, their contribution to the wire conductance is often negligible. Barriers and liners are difficult to scale and may occupy a significant volume when the interconnect width approaches 10 nm, reducing the volume available for copper. Therefore, alternative metals have recently elicited much interest as they could possibly serve as a barrierless replacement for copper [20].

1.1 Resistivity scaling

When the dimensions of a metallic structure are reduced (to the order of its electron mean free path), the surface-to-volume ratio increases, which in turn increases the statistical probability that an electron is scattered at the surface/interface. The scattering can either be specular or diffusive; if an electron, after scattering from the surface/interface, does not lose its momentum in the direction opposite to that of the applied electric field, such

a scattering event is referred to as specular scattering; diffusive otherwise. Specular scattering has no impact on the resistivity and only the diffusive scattering contributes to an increase in the resistivity in scaled structures.

The first study accounting for the *size effect* due to electron scattering at the interfaces for thin films was calculated for a free electron model based on the Boltzmann transport equations [1], and was later extended to wires [2]. The resulting model came to be known as the Fuchs-Sondheimer (FS) model. More on surface scattering shall be discussed in Chapter 2.

Another source of scattering in scaled structures are the grain boundaries. Grain boundaries can be classified as planar lattice imperfections (defects) and can also act as scattering centers (potential barriers) for the charge carriers. In polycrystalline materials, the grain (crystallite) size is universally known to be almost size dependent, and thus scales when the dimensions are reduced. When the grain size approaches the mean free path of the conductor, the enhanced scattering at the grain boundaries contributes to an increase in the resistivity. This effect was first reported in 1969 [4], and was later amended to incorporate the effects of scattering from the interfaces, and is now known as the Mayadas-Shatzkes (MS) model [5]. The model, along with its assumptions and limitations, will be discussed at length in the next chapter.

1.2 Interconnects

The unprecedented growth of the semiconductor industry over the past six decades has been fueled by the relentless miniaturization of the fundamental building block of any integrated circuit - the transistor. The quintessence of this growth has been captured by a rather unassuming empirical projection, came to be known as the *Moore's law* [22], that predicted the number of transistors on an integrated circuit (IC) to double every 18-24 months, and that has guided and steered long-term planning and research goals of the industry.

The unceasing scaling of the physical dimensions has made the computational devices smaller, faster, and cheaper with every iteration. For much of the semiconductor history (till about the year 2000), the basic architecture and operational principle of the transistor did not change

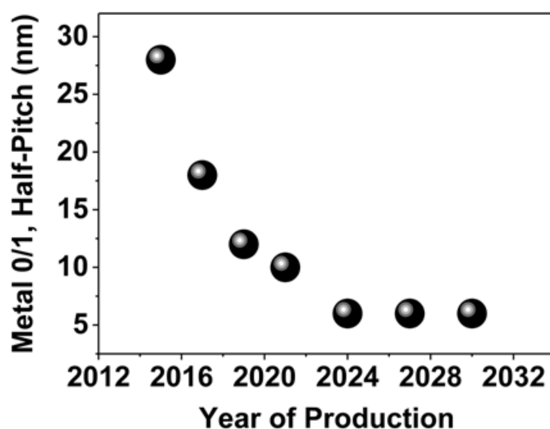

Figure 1.2 International Roadmap for Devices and Systems (IRDS)[1]: the expected trend in the interconnect half-pitch [25]. At such dimensions, scattering effects will severely degrade interconnect resistance and consequently, negatively impact latency, power consumption, cross-talk, and reliability.

significantly. However, since the beginning of this century, the scaling of the transistors has also brought along several issues and challenges that no longer guaranteed the collective benefits of cost and performance [23]. This inspired novel device architectures, ingenious circuit layouts, and material innovations that has allowed the scaling to continue.

Interconnects are conductors and are a vital building block of a ULSI circuit. They link various components across several levels, deliver power, distribute clock signals, and provide grounding. Some of the key figures of merit are resistivity, resistance per unit length, latency, power consumption, reliability, and cross-talk.

Over the years, with the downscaling of the transistors, the dimensions of the interconnects too have shrunk in tandem and are expected to continue to shrink aggressively in the future (**Figure 1.2**). Other than the economic benefits and increased functionality, the key idea behind scaling has been that

---

[1]IRDS is a successor to the ITRS (International Technology Roadmap for Semiconductors) and ITRS 2.0. As of 2017, ITRS is no longer being updated.

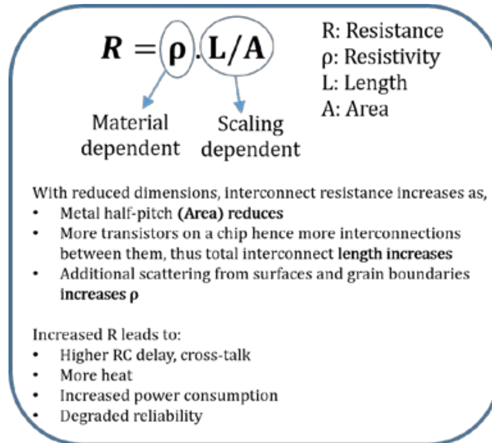

Figure 1.3 Overview: Why resistance increases in scaled conductors and its technological implications on the chip performance.

not only the drive current of a transistor available to switch its load devices linearly increases when its channel length is reduced, but, as the gate area of the transistor reduces (lower area → lower capacitance), the current requirement of the devices at the load decreases, thus improving the overall circuit performance [26]. In contrast, the scaling of the interconnect dimensions not only leads to a smaller cross-sectional area but also to increased scattering of charge carriers, both of which contribute to increased resistivity thus wire resistance, which leads to higher latency (RC delay), increased power consumption, higher heat dissipation, degraded reliability, and cross-talk (higher capacitive coupling with other nearby interconnects) [27] (**Figure 1.3**). These could be justified in the past as not only the scaling of transistor gate length led to significantly improved performance with every generation, but also the improvements in interconnect processing and technology, including material innovations[2] could limit the deterioration in interconnect performance to acceptable levels. In parallel, advancements in low-κ technology [30] reduced cross-talk and kept the RC delay in check. However, the technology now has reached a regime where the total computational delay is heavily dominated by the interconnect delay [27], and

[2]For example, replacing aluminum subtractive etch interconnect processing with copper dual-damascene [28], [29].

as such, the interconnect performance has become a bottleneck in realizing high performance circuits [27].

1.2.1 Copper and the platinum-group metals

Copper has been the choice of metal for interconnect applications over the past two decades now, replacing aluminum that has been the standard till the late 1990s. Resistivity of copper in bulk is 36% lower than that of aluminum ($\rho_{Cu\text{-}bulk}$ = 1.68 μΩcm; $\rho_{Al\text{-}bulk}$ = 2.65 μΩcm), that translated into significant gains in terms of the interconnect resistance and circuit speed (lower RC delay). Additionally, a higher cohesive energy ($E_{cohesive\text{-}Cu}$: 3.49 eV/atom; $E_{cohesive\text{-}Al}$: 3.39 eV/atom [31]), a higher vacancy migration energy ($E_{vm\text{-}Cu}$: 0.72 eV; $E_{vm\text{-}Al}$: 0.58 eV [31]), and a better interface quality of copper (with Ta) over aluminum (with low-κ) enabled superior electromigration (EM) performance and thus more robust reliability of copper interconnects over aluminum [32]. Though there were initial concerns incorporating copper in the then standard semiconductor processing flow (diffusion in silicon and low-κ, etching) [33], they were addressed by incorporating novel material and processing innovations. For example, the use of a thin Ta/TaN layer acts as a diffusion barrier between copper and the surrounding dielectric [33], and a new processing technique called the chemical-mechanical planarization/ polishing (CMP) was invented for copper removal [34], [35] as the standard etching techniques were ineffective due to the inability of copper to easily form volatile products. Since then, a combination of copper deposition and polishing processing called the *(dual-) damascene* has become the standard for fabricating copper interconnects (**Figure 1.4**).

However, copper interconnects too are susceptible to the effects of enhanced scattering at smaller dimensions [14], [15], [36]–[44] and present problems with delay, heat, and reliability [27], [33], [38]. These issues may be addressed by replacing copper with an alternative metal (material) that has a lower line resistance and a better reliability performance.

The main quest for alternatives to copper is motivated by the observation that the resistivity increase in thin films due to scattering at the interfaces and the grain boundaries depends on λ/l. Here, λ is the intrinsic mean free path of the charge carriers in the metal and the characteristic length scale l is the

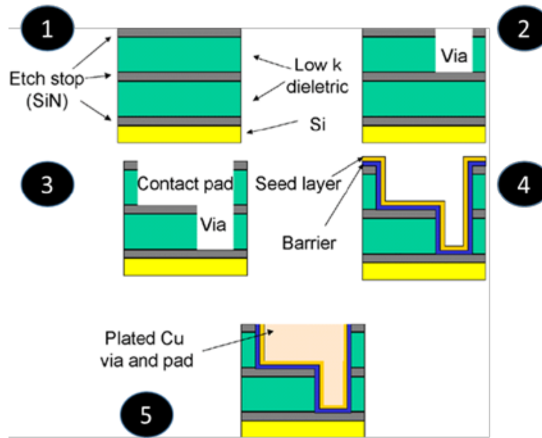

Figure 1.4 Schematic representation of the process steps to fabricate a copper dual-damascene structure and a low-κ dielectric (Figure adapted from [39], [47]).

film thickness for surface scattering or the average linear distance between the grain boundaries for grain boundary scattering. Hence, metals with shorter mean free paths should be inherently less sensitive to scattering at the interfaces and the grain boundaries for a given *l*. As a result, such metals may show lower resistivity than copper for sufficiently small dimensions despite their larger bulk resistivity [11], [45], [46]. However, such a crossover behavior has been elusive so far despite its strong interest for interconnect metallization.

Additionally, it has been shown that the melting point (T_m) of a metal is closely related to the cohesive energy, and also to the vacancy formation energy and self-diffusion kinetics [48], [49]. Thus, the melting point can provide an indication of the expected electromigration (EM) behavior and hence it was argued that the melting point can be considered a proxy for the same [48]–[50]. To that extent, a plot of various elemental metals along with their respective melting points is shown in **Figure 1.5 (a)**. Interesting alternative candidates to copper would have a low bulk resistivity and a high melting point. Among these metals, the platinum-group metals (ruthenium, rhodium, palladium, osmium, iridium, platinum; **Figure 1.5 (b)**) have high melting points (>1550°C) and reasonably low bulk resistivity (<10 μΩcm).

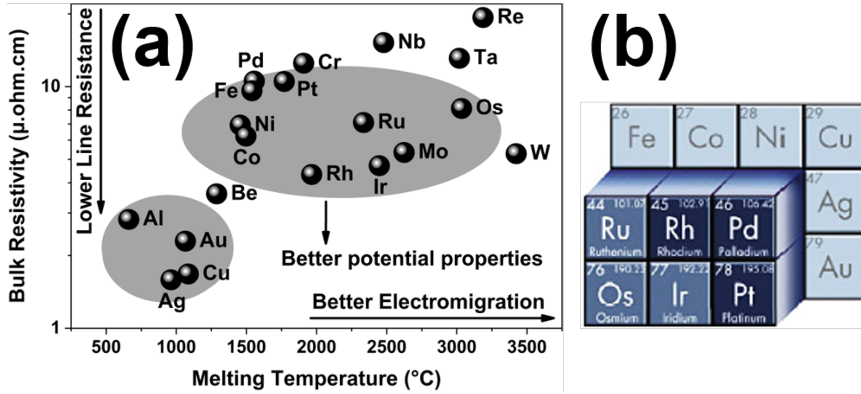

Figure 1.5 (a) Plot of various elemental metals with their bulk resistivity and melting temperature. Potential candidates to replace copper in the interconnects would have a lower bulk resistivity and a high melting point (Figure adapted from [50]). (b) Platinum-group metals (Figure reproduced from [52]).

In addition, they are known to be noble in nature and resistant (to a certain degree) to oxidation. Furthermore, a number of theoretical calculations and ab-initio simulations have also shown that the platinum-group metals could be interesting to be explored for interconnect applications [48], [49], [51].

However, despite the promise, there is little to no experimental evidence that suggests that the platinum-group metals could outperform copper in smaller dimensions. Also, only inadequate data and limited understanding exists on the properties of these metals in scaled structures (especially for highly scaled nanowires with a cross-sectional area of <100 nm^2 and sub-10 nm line width). Thus, the platinum-group metals warrant a thorough examination of their properties in reduced dimensions.

1.3 Motivation

1.3.1 Problem statements

There are several lacunae in the existing literature that provide a motivation for this dissertation, and have been outlined below:

Scattering Mechanisms in Thin Metal Films - Transport in quasi-two-dimensional structures

While the *finite size effect* is universally observed in all metals, there is still a debate over the relative importance of the various scattering contributions to resistivity even for the most studied material, copper [13]–[15], [36], [42]–[44], [53]–[55], and only few comparative studies for different metals have been reported [56]–[58]. Several studies have attributed the resistivity increase in thin copper films and nanowires to only surface scattering while others have argued the grain boundary scattering being the primary mechanism for resistivity increase in smaller dimensions. Additionally, most studies are concentrated on thicker films (>50 nm). Moreover, almost no understanding exists on the scattering behavior of the thin films of the platinum-group metals. Such understanding would be of importance to quantify the impact of various scattering mechanisms on resistivity.

Additionally, according to the model of Mayadas-Shatzkes [4], [5] that describes the scattering behavior in nanostructures, the resistivity increase at smaller dimensions is related to the density as well as the scattering potential of the grain boundaries. The grain boundary density can be controlled by *manipulating* the grain size, which can be achieved through thermal treatment[3]. In addition, the scattering potential of grain boundaries has been argued to depend on the dislocation density at the grain boundaries [59], [60]. Again, annealing has been reported to reduce the dislocation density at grain boundaries resulting in significantly reduced resistivity [61]. Thus, to successfully understand the scattering behavior in reduced dimensions, a thorough understanding of the microstructure is vital.

[3]The theoretical best-case scenario would be to convert a polycrystalline film to a fully crystalline one.

Copper has been studied extensively owing to its widespread use in the microelectronics industry [33], [62], [63], [63]–[66]. However, there is only limited understanding on the annealing behavior of thin platinum-group metal films. As platinum-group metals garner significant attention for interconnect applications, it is of interest to explore the microstructure of such thin films and their response to the applied thermal treatment.

Metallic Nanowires: Transport in quasi-one-dimensional structures

Metallic nanowires are widely used as interconnect structures in ULSI circuits and are expected to scale to the widths of 10 nm and below in the coming years. At such dimensions, the scattering effects are expected to strongly degrade the conduction as well as the reliability. Thus, to effectively tackle the problem, it is paramount to understand the transport properties in such quasi-one-dimensional structures. This understanding would also enable the prediction of the increase in resistivity as a function of dimensional parameters.

In addition, one of the *underrated* challenges that has hampered the investigation of properties in such scaled one-dimensional metallic structures[4] has been the lack of a simple, high-fidelity CMOS-compatible method to fabricate them, even for copper. The existing methods are complex and include numerous processing steps, require extensive process development, and suffer from issues with void-free filling of metal in trenches, and have typically low yield [33]. An effective solution would enable opportunities to examine the small-scale behavior of a wide-range of materials.

1.3.2 Research objectives

Drawing from the discussions above, the research objectives of this work have been outlined below:

[4]Nanowires with cross-sectional area <100 nm^2 and interconnects with sub-10 nm line width

- To investigate the microstructure and the impact induced by annealing on the mechanical and electrical properties of thin (3-30 nm) ruthenium films[5].

- To understand the contribution of various scattering mechanisms to the resistivity in thin (3-30 nm)[6] platinum-group metal films.

- To understand the electrical transport properties of quasi-one-dimensional nanostructures (highly scaled nanowires with < 100 nm^2 cross-section area of platinum-group metals) and gain an insight into their reliability performance.

1.4 Outline

The remainder of this dissertation has been broadly divided as follows:

Finite Size Effects: Chapter 2 deals with the current understanding of the resistivity modeling of thin films and nanowires. Various existing theories to model resistivity are discussed along with their limitations. Typical approaches to modeling in the literature have been reviewed and examined critically.

The latter half of the chapter focuses on the impact of material properties on the resistivity scaling. Several figures-of-merit and associated theories are discussed that aim to shortlist potentially interesting candidates based on their material or electrical properties.

Results & Discussion: The results obtained during the course of this research have been presented in the next three chapters:

---

[5]The scope of this investigation in this work is limited. It only acts to provide sufficient understanding to effectively investigate the finite size effects in thin films and nanowires, which is the primary focus of this dissertation.

[6]This thickness regime is relevant for the current technological trend and also, the effects of scattering becomes stronger when dimensions are reduced.

- In Chapter 3, the microstructural evolution of thin ruthenium films is discussed. It is explored how physical mechanisms resulting from an annealing treatment affect the mechanical and the electrical properties of the films.

- Chapter 4 presents the thickness-dependence of the resistivity of thin platinum-group metal films. Discussed in this chapter are the influence of various scattering mechanisms and their relative contribution to resistivity.

- Chapter 5 explores the properties of metallic quasi-one-dimensional systems. A novel scheme to fabricate highly scaled metallic nanowires is presented, using which the ruthenium nanowires are fabricated. The impact of the reduced dimensionality on resistivity and scattering mechanisms is discussed.

Conclusion and Outlook: The final chapter discusses the overall learnings of this work on a broader physical and technological context, and includes a discussion on the scope of future efforts.

Chapter 2

Finite Size Effects

Objective

This chapter discusses the present understanding of the two topics that are the primary research theme of this work:

- **Size dependence of resistivity:** Existing models describing the various scattering mechanisms that contribute to resistivity increase in smaller dimensions are discussed, along with their assumptions, critical parameters, and scope. This will provide sufficient background to understand the challenges associated with the modeling of thin films using the classical models.

- **Material properties and finite size effects:** A brief review of the theoretical framework examining the role of material properties on finite size effects is presented. Based on the above, figures-of merit are determined to shortlist the most promising candidates for future interconnect applications.

2.1 Scattering mechanisms

2.1.1 Surface scattering

Fuchs was the first to account and model for the increased resistivity due to electron scattering at the surface for a free electron model [1] which was later extended to metal lines by Sondheimer [2]. In reduced dimensions, the higher surface-to-volume ratio leads to increased scattering of charge carriers at the interfaces. The scattering can be specular i.e., no change in momentum (p) in the direction opposite to the flow of current and thus has no effect on the resistivity. For diffusive scattering on the other hand, the loss of momentum of the charge carriers upon scattering gives rise to an additional contribution to the resistivity which results in deviations from the bulk resistivity.

The theory has several simplifying assumptions [1]:

- the disorder in the films should be independent of the thickness
- the film should have clean and plane parallel interfaces
- the application of the Drude model (free-electron approximation) should be valid

In the Fuchs-Sondheimer model, the probability of the electrons scattered specularly at the film interfaces is described by the parameter p, called the surface specularity parameter. p=1 corresponds to fully specular scattering and p=0 is fully diffusive scattering leading to the maximum contribution of surface scattering to the resistivity. The concept, as proposed by the Fuchs-Sondheimer model, has been schematically represented in **Figure 2.1**.

The total thin film resistivity as per the Fuchs-Sondheimer model, assuming the increased resistivity is only due to the non-specular scattering of electrons at the surface, is given by the following relation:

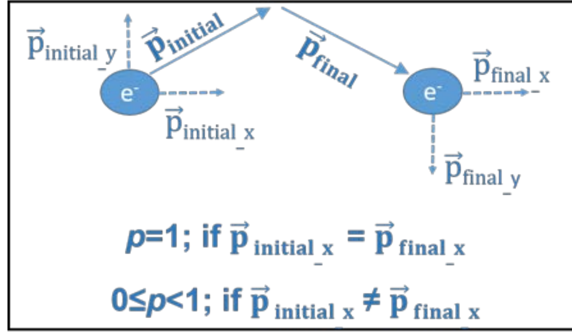

Figure 2.1 Schematic representation of electron scattering at a surface according to the Fuchs-Sondheimer model. p=1 corresponds to specular scattering where the electron conserves the momentum (p) in the direction of its motion after scattering. $p=0$ is a condition for non-specular (diffusive) scattering where the electron loses its momentum in the direction of motion after the scattering event (The direction of electric field is from right to left).

$$\rho_{SS} = \rho_{bulk}\left[1-\left(\frac{3}{2k}\right)(1-p)\int_1^{\infty}\left(\frac{1}{t^3}-\frac{1}{t^5}\right)\frac{1-e^{-kt}}{1-pe^{-kt}}dt\right]^{-1} \qquad (2.1)$$

$$k = h/\lambda_0 \qquad (2.2)$$

ρ_{bulk} is the bulk resistivity, h is the film thickness, and λ_0 is the bulk electron mean free path. t=1/cos θ, where θ is the scattering angle of electrons i.e. the angle between the surface plane and the incoming electron. For a forward moving electron (electron moving in the opposite direction of the applied electric field), θ varies between 0 and 90° and thus the lower and the upper limits of t are 1 and ∞ respectively.

If $h>>\lambda_0$ (films that are several magnitudes thicker than the mean free path), equation (2.1) reduces to:

$$\rho_{SS-thick} \approx \rho_{bulk}\left[1+\left(\frac{3}{8}\right)(1-p)\left(\frac{\lambda_0}{h}\right)\right] \qquad (2.3)$$

Based on equation (2.3) where the resistivity is inversely proportional to the film thickness ($\rho_{ss-thick} \propto 1/h$), it was often concluded that the resistivity increases linearly with decreasing film thickness.

If $h << \lambda_0$ (in case of film thickness much smaller than the mean free path), then equation (2.1) assumes the following form:

$$\rho_{SS-thin} \approx \rho_{bulk}\left[\frac{4(1-p)\lambda_0}{3(1+p)h.\ln(\lambda_0/h)}\right] \quad (2.4)$$

Within the Fuchs-Sondheimer theory of surface scattering (as used in the Mayadas-Shatzkes model), the effect of the surface is not modeled as a scattering event but as boundary conditions of the non-equilibrium distribution function in the Boltzmann equation. Therefore, the phrase "diffuse" vs. "specular" can be a bit misleading and should not be taken literally (for e.g. an angle dependence of a scattering cross-section). Essentially, $p = 0$ means that the momentum relaxation at the surface is so rapid that the non-equilibrium distribution function is equal to the equilibrium Fermi function at the surface. By contrast, $p = 1$ means that the non-equilibrium distribution function is equal to the non-equilibrium distribution function in the bulk of the conductor (i.e., the distribution function is independent of the position in the film). It is clear that in such an approach, p does not need to be directly linked to a specific scattering cross-section. The model by Soffer [67] introduces boundary conditions for the distribution function that depend on the direction of the wavevector (where as p is independent of the wavevector in the Fuchs theory). Thus, the phrase "diffuse" and "specular" cannot be directly linked to statistics of scattering angles in ballistic trajectories.

There are alternative approaches to describe surface scattering based on the calculation of scattering (relaxation) times, for example the model by Ando adapted in the thesis of Kristof Moors [68]. These models calculate relaxation times using Fermi's golden rule based on an assumption of a scattering potential. Both boundary conditions and relaxation time approaches have their advantages and disadvantages. Because relaxation time approaches start from a specific scattering potential, the resistivity can be linked directly to physical parameters such as the RMS roughness and roughness correlation lengths. However, it has been shown that the relevant length scales for surface roughness scattering are of the order of a few atomic distances [69]. Surface roughness on such small length scales are very difficult to characterize for sputtered metallic films and therefore, the calculation of the relaxation times based on experimental roughness input parameters is

essentially impossible. Also, the usage of RMS roughness, correlation lengths, as well as potential height for fitting leads to many more free parameters than in the Mayadas-Shatzkes model and to clearly less accurate results. A further advantage of the Fuchs theory is that it does not depend on the perturbation theory. By contrast, relaxation times in Ando's model are calculated typically using Fermi's golden rule. The thesis of Kristof Moors contains some discussion on the accuracy of Fermi's golden rule for the calculation of scattering rates [68]. This is however clearly beyond the scope of this experimental thesis.

The downside of the Fuchs theory (the Mayadas-Shatzkes model) is that the parameter p that describes the boundary conditions at the surfaces is fully phenomenological and cannot be directly related quantitatively to any real surface scattering processes. Qualitative comparison are however still possible, as for example done in the work by Zahid and others [70]. This will be discussed later in Chapter 4. One of the biggest challenges in understanding the impact of the *cladding* layer on surface scattering is the lack of a general predictive theory that correlates the material properties of the interface/*cladding* to the boundary conditions of the center conductor. The general consensus, derived from ab initio transport and relaxation time calculations, is that the origin of surface scattering is the geometrical roughness and an atomically smooth surface will always demonstrate $p = 1$ irrespective of the nature of the interface. Zahid et al. [70] argued, for copper, that the use of *cladding* metals which have the same density of states at the Fermi level as that of copper will electronically 'smoothen' the geometrical roughness. They showed, by ab initio methods, that the use of aluminum or palladium as capping/*cladding* on copper, whose density of states at the Fermi level matches that of copper, will result in specular scattering while the use of tantalum or ruthenium will result in diffused scattering due to the mismatch of the density of states at the fermi level. Experimentally, it was shown by Rossnagel et al. [13] that a thin tantalum layer on copper led to fully diffused surface scattering. However, when the tantalum layer was allowed to oxidize in air, the surface scattering turned specular. It shows the extremely sensitive nature of surface scattering. Chawla et al. [71] demonstrated similar results for copper with a thin tantalum layer on top. They claim that the atomically smooth interface results in a flat periodic potential that causes the conduction electrons to specularly scatter at the interface. However, the addition of a tantalum layer on copper causes a

perturbation to the smooth interface potential and results in displaced scattering centers from the original interface and cause completely diffuse surface scattering. However, since it is difficult to determine the scattering potentials of such realistic surfaces, such questions cannot be conclusively answered. Still, qualitative comparison between our results and the literature can be done and there are many similarities between our results on Cu, Ir, Ru, and Rh and previously published work essentially exclusively on Cu.

In this thesis (discussed in chapter 4), diffusive scattering was also observed for Ru with TaN cladding as well as for Ru with TiN interface. However, specular scattering was observed for Ru on SiO_2 consistently (as deposited and annealed PVD Ru on SiO_2, as well as ALD Ru on SiO_2). Similar observations were made for Ir on SiO_2 and Rh on SiO_2. This would mean that SiO_2 is able to electronically smoothen the rough metal interfaces, which is difficult to believe as SiO_2 is an insulator. This raises questions on the validity of the "electronic smoothening" model. Verifying the validity of the model would require the DOS calculations from ab initio methods that is beyond the scope of this thesis and is thus proposed in the outlook.

The model of Fuchs-Sondheimer does not explicitly account for the surface roughness in thin films. A rough surface/interface might act to reduce the surface specularity parameter and contribute to an increased resistivity. The relation between surface scattering and surface roughness has been discussed by Ziman [72], Soffer [67], and Rossnagel & Kuan [13], who offered improvements on the existing model of Fuchs-Sondheimer to account for the surface roughness. In Soffer's model, the surface scattering is assumed to be purely due to the presence of surface roughness and includes a parameter *r* that uses the roughness of the scattering surface and calculates the probability of specular reflection as a function of the angle of incidence, θ, between the surface and the charge carriers. The surface specularity parameter is then given by:

$$\boldsymbol{p_s(\cos\theta) = \exp\left[-(4\pi r/\lambda_F)^2 \cos^2\theta\right]} \qquad (2.5)$$

λ_F is the fermi wavelength of electrons. By substituting cos θ = u, the total film resistivity takes the following form:

$$\boldsymbol{\rho_{\text{Soffer}}} = \boldsymbol{\rho_{\text{bulk}}} \left[\mathbf{1} - \left(\frac{\mathbf{3}}{\mathbf{2k}}\right) \int_{\mathbf{0}}^{\mathbf{1}} \left(\mathbf{u} - \mathbf{u^3}\right) \frac{(\mathbf{1}-\boldsymbol{p}_{\mathbf{s}}(\mathbf{u}))(\mathbf{1}-\mathbf{e^{-k/u}})}{\mathbf{1}-\boldsymbol{p}_{\mathbf{s}}(\mathbf{u})\mathbf{e^{-k/u}}} \mathbf{du} \right]^{-\mathbf{1}} \qquad (2.6)$$

Additionally, the Soffer's expression to calculate the resistivity of thin films also has the provision to account for the roughnesses of the top and the bottom interfaces separately [67]. The model however has its limitations: firstly, as discussed, the model assumes that scattering at the surface is due only to the surface roughness. This means the capping or *cladding*[7] material would not influence the surface scattering behavior. It has been shown theoretically [70] as well as experimentally [73] that the surface scattering indeed depends on the *cladding* material for same (similar) roughness. And secondly, these improvements still do not account for the resistivity increase due to grain boundaries and a simple mathematical addition of resistivity contribution from grain boundaries (discussed in the next section) need not necessarily be true, as it would assume that the surface and grain boundary scattering events are independent of each other, which might not be the case in very small dimensions.

Another adaptation of the Fuchs-Sondheimer model to extend its applicability and account for additional parameters was published by Rossnagel and Kuan [13]. This offered an improvement over Soffer's method and proposed semi-empirically, based on Monte-Carlo simulations, a model that takes surface roughness (in the form of a phenomenological roughness factor *f*, that is an empirical constant greater than or equal to 1.0 and estimated from Monte-Carlo model [13]) as an input parameter and still contains *p* as a fitting parameter. In this way, the model can not only account for surface roughness but also considers the influence of the *cladding* material.

$$\boldsymbol{\rho_{\text{SS-RK}}} = \boldsymbol{\rho_{\text{bulk}}} \left[\mathbf{1} + \left(\frac{\mathbf{3}}{\mathbf{8}}\right) (\mathbf{1} - \boldsymbol{p}).\boldsymbol{f}.\left(\frac{\boldsymbol{\lambda_0}}{\boldsymbol{h}}\right) \right] \qquad (2.7)$$

The model implies that a higher roughness factor will result in a higher resistivity. However, their model suffers from the same drawback as that of the Soffer's model. Additionally, the calculation of the roughness factor is non-trivial and the methodology has not been published in the public domain (see reference 24 in [13]).

---

[7]Cladding refers to the surrounding material. For example, in a stack of TaN/Cu/TaN, TaN is the cladding material.

Other subsequent works have proposed to include two separate surface scattering parameters for the top and bottom interfaces [74], [75]. Modifications for anisotropic films (due to non-spherical fermi surface) have also been proposed [76]. However, all the above models do not account for resistivity contribution due to the scattering of charge carriers at the grain boundaries.

All the above reformulations of the Fuchs-Sondheimer model attempt to improve the overall understanding of the surface scattering. However, additional parameters describing surface conditions such as the small-scale surface roughness (of the order of electron fermi wavelength, λ_F, typically ~ 0.5 nm), surface asperities, angle of incidence are required but are case-specific and difficult to experimentally measure. Thus, improvements of the Fuchs-Sondheimer model cannot yet be used directly for evaluating surface scattering.

2.1.2 Grain boundary scattering

Generally, the (average) size of the crystallites is known to scale with the dimensions and thus, smaller structures will have a higher grain boundary density than bulk. As grain boundaries act as scattering planes for the charge carriers, an increase in resistivity is expected at smaller dimensions. This effect was first reported in 1969 [4] to explain the higher resistivity for smaller structures, and was later expanded to incorporate effects of scattering from the interfaces as well. This model is now known as the Mayadas-Shatzkes (MS) model [5].

The Mayadas-Shatzkes model defines a parameter R, the grain boundary reflection coefficient, which corresponds to the probability of an electron getting reflected at the grain boundaries. Thus, a higher R implies a lower transmission probability and thus an increased resistivity. A schematic

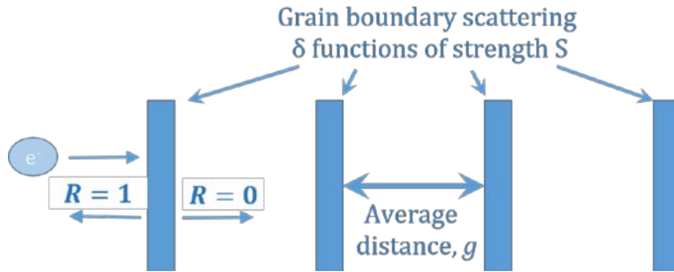

Figure 2.2 Schematic representation of electron scattering at a grain boundary according to the Mayadas-Shatzkes model [5]. Grain boundaries are visualized as scattering planes: a delta function δ with strength S, **and are regarded as effective representations for an ensemble average of grain boundaries with different shapes and orientations**. R=0 corresponds to electron being fully transmitted through the grain boundary without any loss of momentum in the direction of the electric field, thus no contribution of grain boundary scattering to resistivity. R=1 refers to electron being fully reflected from the grain boundary leading to infinite resistivity (Figure adapted from [5]).

representation of electron scattering at the grain boundaries according to the model is shown in **Figure 2.2**.

The following simplifications are made in the model:

- Electrons are scattered only at grain boundaries perpendicular to the electrical field. Other grain boundaries (scattering planes) are neglected.

- The distribution of the distances between perpendicular grain boundaries can be represented by a Gaussian distribution with a mean distance g (known as the mean linear intercept length[8] [77]) and a standard deviation s, which is assumed to be large.

---

[8]In the original paper of the Mayadas-Shatzkes [5], the linear intercept length was (incorrectly) referred to as the grain size. The linear intercept length need not necessarily be the same as the grain size. This would in turn affect the determination of the grain boundary reflection coefficient R.

- The potential of a scattering plane, V_x, at an arbitrary position x_n can be represented by $V_x = S.\delta(x-x_n)$, where S is the strength of the scattering plane and δ is a delta function.

The strength of the scattering plane is related to the grain boundary reflection coefficient by the following relation:

$$\mathbf{S} = \sqrt{\frac{\hbar^3 \boldsymbol{R}}{2\mathbf{m_e}(1-\boldsymbol{R})}\mathbf{v_F k_F}} \tag{2.8}$$

where, v_F is the fermi velocity and k_F is the fermi wave vector.

The first model of Mayadas-Shatzkes for thin film resistivity [4] considered that the resistivity increase at smaller dimensions is only due to grain boundary scattering (and fully specular scattering at external surfaces), and is given by [4]:

$$\boldsymbol{\rho_{GB}} = \boldsymbol{\rho_{bulk}}\left[1 - \left(\frac{3}{2}\alpha\right) + 3\alpha^2 - 3\alpha^3 \ln\left(1 + \frac{1}{\alpha}\right)\right]^{-1} \tag{2.9}$$

$$\boldsymbol{\alpha} = \frac{\lambda_0}{g}\frac{R}{1-R} \tag{2.10}$$

It has recently been pointed out that the expression for α in the Mayadas-Shatzkes formulation misses a factor of 2 (see supplemental information in [73]). The corrected expression of α is as below:

$$\boldsymbol{\alpha'} = \frac{\lambda_0}{g}\frac{2R}{1-R} \tag{2.11}$$

The R obtained from α' ($R_{\alpha'}$) can be compared to studies based on the original definition of α by using $R_{\alpha'} = 2R/(1 + R)$. Additionally, if p and R are correlated, this would also affect the determination of p. In this work, the corrected expression of α, i.e., α' will be used.

For very thick films, $g >> \lambda_0$, equation (2.9) can be reduced to:

$$\boldsymbol{\rho_{GB-thick} \approx \rho_{bulk}\left[1+\left(\frac{3}{2}\right)\frac{\lambda_0}{g}\left(\frac{R}{1-R}\right)\right]} \tag{2.12}$$

Equation (2.9) was later amended by the same researchers to also incorporate non-specular scattering from external surfaces and takes the final form as below [5]:

$$\boldsymbol{\rho_{tf} = \left\{\frac{1}{\rho_{GB}} - \frac{6}{\pi k_0 \rho_0}(1-p)\int_0^{\pi/2} d\varphi \int_1^{\infty} dt \frac{\cos^2\varphi}{H^2}\left(\frac{1}{t^3}-\frac{1}{t^5}\right)\frac{1-e^{-k_0 tH}}{1-pe^{-k_0 tH}}\right\}^{-1}} \tag{2.13}$$

$$\boldsymbol{H = 1 + \frac{\alpha'}{\cos\varphi\sqrt{\left(1-\frac{1}{t^2}\right)}}} \tag{2.14}$$

φ is a variable of integration and refers to the azimuthal angle of the spherical coordinate system with poles located on the z-axis. For the electrons in given energy state k` being scattered by the grain boundaries to k``, φ(k`)=f(k`)-f_0(k`) is the deviation of the distribution function f(k`) from its equilibrium value f_0(k`). (The above expression is a part in the attempt to solve the electron transport using a Boltzmann approach described elsewhere in detail [5]). All other parameters have already been defined earlier.

Equation (2.13) allows for the case when the surface and the grain boundary scattering cannot be regarded to be operating independent of each other (typically the case for very thin films), and as such, *p* and *R* are correlated. Thus, equation (2.13) does not fulfil Matthiessen's criteria; that resistivity contributions from various scattering mechanisms can be arithmetically added to obtain the total thin film resistivity. However, this also makes it non-trivial to untangle the contributions of surface scattering and grain boundary scattering to thin film resistivity from each other.

In case of sufficiently thick films (film thickness >> mean free path), the scattering of charge carriers at the surface/interface and the grain boundaries can be approximated to be independent of each other and the total film resistivity can be obtained by adopting the Matthiessen's rule, by arithmetically adding contributions of all the scattering mechanisms:

$$\boldsymbol{\rho_{thick\ film} = \rho_{bulk} + \rho_{ss-thick} + \rho_{GB-thick}} \tag{2.15}$$

However, such approximations must be adopted with caution and their applicability must be thoroughly ensured. In this work, only the full numerical formulation of the Mayadas-Shatzkes model has been used (equation 2.13) as films under investigation were of the order of or smaller than the mean free path.

As has been discussed earlier, several studies in the past have used simplified versions of the Fuchs-Sondheimer and Mayadas-Shatzkes relations (equation (2.3) and equation (2.12), respectively) [37], [40], [41], [45]. Such approximations could be deemed acceptable as the thickness ranges under investigation in those studies were of the order of hundreds of nanometers and much larger compared to their respective mean free paths. However, such simplifications could lead to erroneous inferences when film thickness approach the respective conductor's carrier mean free path.

In essentially all non-ab-initio models, GB scattering is treated via a quantum tunneling through a delta-function-like energy barrier. Thin films are then represented by an aperiodic series of delta potentials. The tunneling process is described by the parameter *R*, which is the reflection probability for an individual tunneling process and has thus a direct physical meaning. As discussed above, *R* does not depend on the conductor material only but also on the type of the grain boundary. It is completely unrelated to the surface scattering parameter *p*. The transmission of electrons through surface is negligible and so surface scattering always corresponds to full reflection.

Recently, a simple model was proposed by Zhu et al. [78] for the material dependence of *R* for polycrystalline films. Here, the grain boundary scattering is treated as the tunneling phenomena of the charge carriers through the grain boundaries with a transmission coefficient Γ. Thus, the grain boundary reflection coefficient *R* is basically 1- Γ and is as follows [79] :

$$\boldsymbol{\Gamma = 1 - R = \left[1 + \frac{E_p^2 sinh^2(\beta w_b)}{4E(E-E_P)}\right]^{-1}} \qquad (2.16)$$

E is the energy of the charge carrier; E_p is the potential energy of the barrier; w_b is the width of the barrier; and β is as follows:

$$\boldsymbol{\beta = \frac{\sqrt{2m|E_P - E|}}{\hbar}}$$

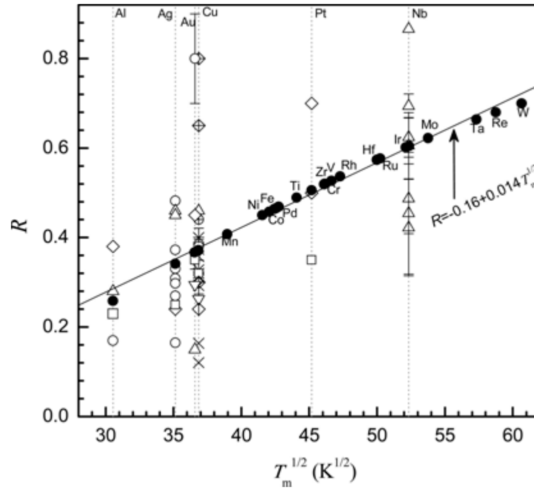

Figure 2.3 Grain boundary reflection coefficient *R* as function of $T_m^{1/2}$ given by the solid symbol (●) for selected metals, where the solid line refers to $R = -0.16 + 0.014\ T_m^{1/2}$. Other symbols show the reported fitting results of R for Al [5], [80], Ag [81], [82], Au [83]–[85], Cu [5], [13], [36], [40], [41], [43], [44], [81], [86]–[93], Pt [94], [95], and Nb [89]. T_m of metals are cited from [96] (Figure reproduced from [78])

ħ is the reduced Planck's constant. Zhu et al. further relate the potential energy of the barrier to the surface energy of a metal and eventually to its cohesive energy and melting point. The final expression for *R* takes the following form:

$$\boldsymbol{R = -0.16 + 0.014 T_m^{1/2}} \tag{2.17}$$

Since the melting point is proportional to the cohesive energy [96], *R* was linked to the bond strength of metals. Thus, higher bond strength leads to stronger scattering at the grain boundaries. This means, metals with a higher melting point will have a higher contribution of grain boundary scattering to resistivity.

In **Figure 2.3**, the predictions of the theoretical model for *R* (equation 2.17) are compared to the experimentally obtained *R* for some of the reported metals. *R* in experiments has been found to vary to a certain degree, but, in

general, is consistent with the prediction of being proportional to the melting point and that *R* is larger for more refractory metals. This enables the evaluation of resistivity of thin films and nanowires without any adjustable (fitting) parameters while assuming that the resistivity increase at smaller dimensions is only due to grain boundaries scattering. Additionally, from this model it can be inferred that the contribution of grain boundary scattering to resistivity assumes more importance for metals with higher melting points. However, due to the absence of any other parameter, this model would not be able to evaluate the effect of microstructural changes on the grain boundary reflection coefficient. Thus, this relation should rather be used qualitatively than quantitatively, meaning, a metal with a higher melting point can be expected to have a higher *R* with a certain degree of variability as has been discussed that *R* depends on the nature of the grain boundaries and is not material intrinsic.

Furthermore, in **Figure 2.3**, the reported values for *R* for metals such as aluminum, silver, gold, copper, platinum, and niobium films or wires show considerable variation (almost evenly distributed on either side of the predicted values) that could arise from a number of factors including, but not limited to: (a) amorphous or crystalline nature of the material, (b) degree of thermal treatment, (c) defect density or impurity concentration - the Mayadas-Shatzkes model assumes constant bulk density and does not account for defect density or impurities; thus, presence of impurities or a higher defect density would result in an inflated *R*, (d) diffused scattering – if contributions of surface scattering is not accounted, then the *R* would increase, (e) over/under-estimation of the linear intercept length – and underestimated *g* would result in an underestimation of *R*, (f) use of model approximations when not valid.

The tunneling description of grain boundary scattering assumes to some extent "zero roughness" of the grain boundaries. As show in [97] and discussed above, grain boundaries parallel to the current do not affect the resistivity. It is possible to introduce a "roughness" of the grain boundaries, for example via boundary conditions for the distribution function or by modifying the scattering potential. Except for a short remark in the conclusion of [97], no literature exists on this topic. This is indeed an interesting question from a theoretical point of view. Because the scattering potentials and the parameters describing the roughness of surfaces and grain

boundaries are not (necessarily) the same, there is no reason to believe that the p values for surface and grain boundary scattering would correlate. In absence of a model for "rough" grain boundaries, it is not possible to estimate the impact of this effect on the thin resistivity. From an experimental point of view, the roughness can be considered as an additional extrinsic influence on the R parameter for a metal. Hence, as already mentioned, a deduced R value should be considered as an effective value for the thin film under study. Still, the rather consistent set of R values found for a number of ruthenium thin film series with different microstructure (will be discussed in chapter 4) suggests that such extrinsic influences are not dominant.

R for tilted Grain Boundaries

Since the Mayadas-Shatzkes model is essentially a one-dimensional model, it treats only grain boundaries that are perpendicular to the current flow. A practical sample however will deviate from this assumption. It is also to be noted that even in a perfectly bamboo-like grain structure, the grain boundaries will not be perfectly perpendicular as the twist of grain around the sample normal will also lead to grain boundaries that are not perpendicular to the current direction and not all the grain boundaries will be perpendicular to the transport direction. The same applies for thin films too.

Recently Moors et al. [97] have used a quantum model to calculate the resistivity of metallic nanowires for inclined grain boundaries. The grain boundaries are described by delta-function-like barriers, similar to the Mayadas-Shatzkes model. The paper shows that tilted grain boundaries scatter less than perpendicular ones, as one would expect intuitively. This can be understood as follows: applying quantum mechanical scattering theory to a tilted grain boundary plane potential, one obtains a scattering amplitude which peaks around the direction of elastic backscattering. So, in case of reflection from a perpendicular grain boundary, the forward velocity of the electrons is (with high probability) fully reversed, implying maximum current loss and maximal resistivity. The larger the average tilt angle becomes, the less the forward velocity is affected and the lower the resistivity becomes (semi-classically, this can be construed as a reduction in R). When the tilt further increases such that the grain boundaries lie parallel to the transport direction, any grain boundary scattering event should not affect the forward velocity at all, hence the resistivity contribution from those grain boundaries

will be (close to) zero. So, in order to achieve the lowest resistivity contribution, one would like to have all the grain boundaries tilted away from the perpendicular direction as much as possible (this is very difficult to fabricate such a wire and prove experimentally).

However, for a set of grain boundaries with randomly distributed tilt, the differences to the perpendicular case are very small and can be neglected. In practical films (even if they are textured) there is no reason to assume that there will be a preferential tilt angle on a macroscopic scale that is inclined in a specific direction other than the film normal. Therefore, from this model (the only one available for this case to our knowledge), there is no reason to expect measurable differences in R due to the inclination of some gain boundaries.

In any case, the determined R value will represent an ensemble average over the microstructure. The model of Moors et al. in [97] indicates that a random distribution of tilt and twist angles does not lead to a clear modification of R and thus the different types of grain boundaries (e.g. depending on the relative tilt or twist angle between adjacent grains) appear to play a larger role. It is currently not possible to analyze this issue further. Theoretically, the relative grain orientation can be measured by TEM (the grain sizes are too small for EBSD) but the determination of the detailed grain boundary structure is non-trivial and cannot be done for a large amount of grain boundary configurations. Moreover, there is currently no real possibility to calculate an R value for a given grain boundary configuration. Some simple twin boundary configurations have been assessed by ab initio methods [98] but this assumes ideal configuration and cannot be generalized to other types of grain boundaries. Finally, there is currently no theory available how to calculate a macroscopic average of R for a distribution of grain boundaries except in the paper of Moors et al. [97] that treats twisted and tilted delta-function-like potentials. Therefore, a discussion of R can only be qualitative as done in the dissertation (Chapter 4), where a reduction of R by annealing was qualitatively (and coincidentally) linked to a reduction of the grain boundary angles, as commonly observed for recrystallization in metals.

2.1.3 Common approaches to resistivity modeling

After discussing several models of surface scattering and grain boundary scattering, it is now apt to briefly discuss the various approaches taken in the literature while modeling the thickness dependence of resistivity.

In the past, while employing the Fuchs-Sondheimer and the Mayadas-Shatzkes theories to model the thickness dependence of resistivity in thin films and nanowires, several studies have employed the approximations of both these models (usually, equation (2.3) for the Fuchs-Sondheimer model, and equation (2.12) for the Mayadas-Shatzkes model) instead of using the full numerical solutions [37], [40], [41], [45]. As a reminder, such approximations are only valid when the film thickness is several factors greater than the mean free path of electrons. However, implementing the above approximations incorrectly could lead to large discrepancies in the p and R values while modeling the same material (typically, employing the approximate version of the Mayadas-Shatzkes model with specular interfacial scattering, the fitted R would be an overestimation so as to compensate for the neglected higher order terms).

Another common approach has been the use of Matthiessen's rule to combine the contributions of surface scattering and grain boundary scattering [37], [40], [41], [45], [99], which, in other words, implies that the scattering of charge carriers at the surfaces and at the grain boundaries are independent of each other. This is only applicable when the film thickness is much larger compared to their respective electron mean free paths. For smaller structures, it has been shown that the surface specularity parameter and the grain boundary reflection coefficient are strongly correlated [53]. An incorrect assumption of the validity of the Matthiessen's rule here would correspond to neglecting the interaction between the surface scattering and the grain boundary scattering (such interaction leads to a higher resistivity[9])

[9]The resistivity contribution from the second term on the RHS of equation (2.13), that is the contribution of surface scattering convoluted with the grain boundary scattering, is greater than the resistivity contribution from the surface scattering alone, as described in equation (2.1).

that would result either in a reduced p or/and an increased R to compensate accordingly. Such a comparative study was published elsewhere [44].

Next, in the Mayadas-Shatzkes model, an important experimental input is the mean linear intercept length (the average distance between the grain boundaries in the direction of current flow; equation (2.10)). This has been often equated to the film thickness, or (in-plane or out-of-plane) grain size, presumably due to lack of experimental data. As linear intercept length is closely related to the evaluation of grain boundary reflection coefficient, incorrect inputs could lead to erroneous outcomes as described in the previous section. Moreover, for smaller structures where grain boundary scattering could be correlated to surface scattering, an incorrect linear intercept length could also affect the assessment of the nature of surface scattering. Only a few research articles have experimentally accounted for the linear intercept length while modeling thin films modeled using the Mayadas-Shatzkes model [42]–[44].

In addition to the above, there are a few general issues associated with modeling the size-dependence of resistivity. Another input parameter in the Fuchs-Sondheimer as well as in the Mayadas-Shatzkes model is the bulk resistivity. Usually, Fermi surfaces for metals are assumed to be spherical for the sake of simplicity but is widely known to be otherwise. For polycrystalline films, this translates into a texture dependence of the bulk resistivity. For example, in ruthenium (hcp crystal structure), vastly different fermi wavelengths in directions parallel and perpendicular to the hexagonal axis result in significantly different resistivity values [100]–[102]. A lower value for the bulk resistivity would force the p to reduce and/or R to increase (and vice-versa) to match the experimental value. Hence, accurate microstructural analysis of nanostructures under investigation is another important aspect of resistivity modeling. Furthermore, thermal treatment can alter the microstructure and the grain size (thus the linear intercept length) which could influence the assessment of the scattering mechanisms.

Approach to size-dependent resistivity modeling in this work and critical analysis of the Mayadas-Shatzkes model

In both the Fuchs-Sondheimer theory as well as Ando's model [103], grain boundary scattering is not included. In relaxation time models, the grain

boundary scattering can be added via the classical Mayadas-Shatzkes approach (for $p = 0$) using Matthiessen's rule. No calculations without the need for Matthiessen's rule have been published. However, the Mayadas-Shatzkes model does not require the assumption of the validity of Matthiessen's rule for surface and grain boundary (or phonon) scattering. Matthiessen's rule only needs to be valid between grain boundary and phonon scattering, as experimentally typically observed [83]. As a matter of fact, the Mayadas-Shatzkes model does not satisfy Matthiessen's rule as it cannot be separated into surface scattering and grain boundary scattering contributions. In the original paper [5], Mayadas and Shatzkes argue that there is a physical reason why this is the case, namely the "renormalization" of the mean free path that determines surface scattering in a polycrystal with grain boundary scattering. The argument is discussed in the thesis later in Chapter 4. Experimental papers that use Matthiessen's rule approximations of the Mayadas-Shatzkes model [43], [44] find rather different p and R values for the same data set. Thus, the usage of the full Mayadas-Shatzkes model is strongly preferred over Matthiessen's rule approximations and in fact over any theory assuming the validity of Matthiessen's rule.

In this work, the full numerical formulation of the Mayadas-Shatzkes model (equation (2.13); that considers the surface and the grain boundary scattering to be simultaneously operative) [5] is used to model the resistivity of thin films as the thickness regime of interest (3-30 nm) for the platinum-group metals and copper is of the order of or less than their respective mean free paths [73], [100]. Moreover, the use of the Mayadas-Shatzkes relation in entirety allows for the study of possible correlations between the surface scattering and the grain boundary scattering events in thin films (which are not necessarily observed for thicker films). Finally, extensive microstructural data on the films that are modeled have been collected (and have shown that typical assumptions such as grain size being roughly equal film thickness needn't necessarily be accurate and can lead to large errors). Such data collection is critical as incorrect assumptions could lead to erroneous conclusions. It is also reckoned that such assumptions, along with incorrect use of approximations of the fitting models, could be the reasons for the dissenting reports on the nature of surface and grain boundary scattering reported in the literature for copper.

As far as the approximations in the model are concerned, there are two main approximations involved. First, the assumption of a spherical Fermi surface may not be appropriate. The Fermi surface of copper is somewhat spherical but the Fermi surfaces of ruthenium and iridium strongly deviate from it [100]. Being an hcp crystal, ruthenium also shows a strong anisotropy in the Fermi surface and thus in the conductivity. Presently, there is no theory available to predict the resistivity of "thick" metallic films in the presence of grain boundary and surface scattering using actual Fermi surfaces of metals such as copper and in particular ruthenium. An improvement on the semi-classical Mayadas-Shatzkes model for ellipsoidal Fermi surfaces was applied to the experimental data [104]. As it is shown in the paper, the non-spherical shape of the ruthenium Fermi surface does not affect the p and R values within errors even for a strongly anisotropic metal as that of ruthenium.

Additionally, the Mayadas-Shatzkes model ignores the modification of the Fermi surface due to the quantum confinement effects. Quantum confinement effects can affect the experimental data in several ways. First, they could lead to oscillations in the thickness dependence of the resistivity (as discussed in the paper by Trivedi and Ashcroft [8]). Such quantum effects should be noticeable for thin films with thicknesses of the order of the mean free path. This is the case for the thinnest films in this dissertation, even at room temperature. However, the period of the oscillations is half the Fermi wavelength (for metals, the Fermi wavelength is ~5 Å). This means that the period should be of the order of around 2-3 Å. Such effects have been seen in epitaxial ultrathin films [8] but typically fade away for thicknesses of the order of 1 nm due to roughness build up, making the thickness non-uniform. In sputtered films with thicknesses of the order of a few nm and RMS roughnesses of a few Å, it is clear that such effects will not be observed.

Furthermore, when quantum effects are present, they modify the density of states and the Fermi surface and may thus affect the scattering rates at the surface and grain boundaries. Quantum models within an isotropic effective mass approximation (i.e. neglecting realistic band structures) using a different approach to describe surface scattering based on Ando's model [103] show that quantum effects led to significant modifications of surface scattering rates when the number of occupied subbands at the Fermi level was about 10 or less [105] (the treatment of grain boundary scattering was however identical to that of Mayadas and Shatzkes). Of course, it is clear that no sharp

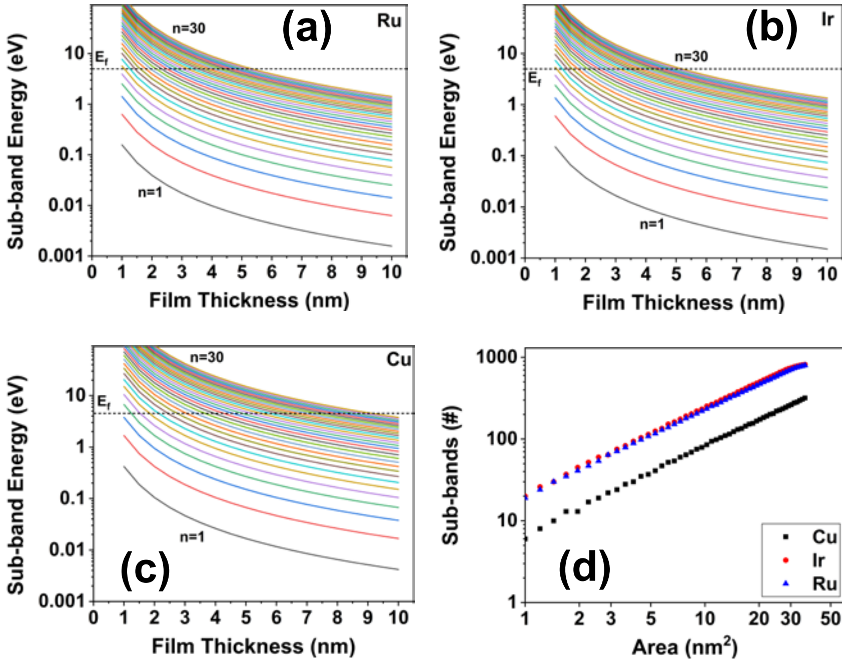

Figure 2.4 Sub-band energy levels in z-axis for film thicknesses between 1 and 10 nm for (a) ruthenium (b) iridium, and (c) copper (d) For nanowires, the number of sub-bands below the fermi energy across the conductive cross-section as a function of the cross-section area.

transition from semiclassical to quantum regimes can be identified. However, in this range, effects would become large enough so that the experimental points should start to deviate from "thick film" trendlines within typical experimental precision.

Films are only confined in one dimension (z-axis) and have continuous range in the other two directions. Therefore, confinement effects on the surface scattering should be weaker than in wires. To assess this further, the energy of the 30 lowest sub-bands in the confined dimension were calculated for ruthenium, iridium, and copper in an effective mass approximation using the following equation,

$$E_n = \frac{n^2 h_p^2}{8m^* h^2} \tag{2.18}$$

E_n is the subband energy, n is the subband index, h_p is the Planck's constant, m* is the effective mass (2.36 for ruthenium, 2.51 for iridium, and 0.9 for copper [106]), and 'h' is the film thickness. Fermi energies were also determined from ab initio calculations [106]. Given the energy difference between the bottom of the band and the Fermi level, one can see from the plot (**Figure 2.4 (a) – (c)**) how many sub-bands can be filled. For the thinnest ruthenium and iridium films of 3 nm, around 20 subbands are filled. For 3 nm copper, due to the lower effective mass, about 10 subbands are filled and some weak quantum effects cannot be fully excluded. However, copper films of 5 nm and above should be rather well described by semiclassical models.

For the smallest ruthenium nanowire produced in this work of ~33 nm² (~6 nm x 6 nm square wire), the total number of subbands in the confined two dimensions below the Fermi energy (5 eV) is 797 (**Figure 2.4 (d)**) as calculated from the following equation:

$$\boldsymbol{E_{n,m}} = \frac{(\boldsymbol{n^2}+\boldsymbol{m^2})\ \boldsymbol{h_p^2}}{\boldsymbol{8m^*h^2}} \tag{2.19}$$

For grain boundary scattering rates, a much weaker modification by quantum effects than for surface scattering is expected [97]. This can be understood that grain boundary scattering mainly involves forward or backward scattering in a direction that is not affected by quantum confinement. Note that the model describing tilted and twisted grain boundaries [97] takes quantum confinement into account and is thus not affected by angled grain boundaries. Therefore, the semiclassical description of grain boundary scattering appears fully justified.

For very small nanowires, quantum effects will also affect the ballistic conductance due to a reduction of the transmission channels. This was shown recently by ab initio calculations by Zhou et al. [107] and Lanzillo [98] for copper wires with diameters in the 1 to 3 nm range. No transition to classical behavior was shown in these papers since sufficiently large systems could not be studied. These wires are still much smaller than even the smallest wires studied experimentally in this dissertation. The effects were rather small (~17% conductivity reduction for a 3 nm wire in Lanzillo [98]) with respect to the increase in resistivity due to surface and grain boundary scattering. Also, for thin films, effects can be safely expected to be much smaller due to

weaker confinement, so given the current theoretical status, it appears acceptable to use the bulk resistivity in the Mayadas-Shatzkes model.

For electron-phonon scattering, quantization effects are not expected to have a drastic impact, because a standard acoustic phonon spectrum will basically be able to scatter a state into any other k_x value, and this is not affected by quantizing the electron spectrum.

Thus, the usage of the semiclassical Mayadas-Shatzkes model appears justified for essentially all thin films and nanowires except possibly the thinnest copper film(s). Therefore, subsets of the data have been individually fitted, e.g. by omitting the thinnest films and studying whether a clear dependence of the parameters p and R on the film thickness could be identified. It should be noted that this would not necessarily be a sign for quantum effects since other factors (surface roughness, microstructure) may also show a thickness dependence. However, within experimental precision, no thickness dependence of p or R could be evidenced. Since a large part of the films were in a thickness range > 5nm, where quantum effects can be safely neglected, this indicates that a semiclassical analysis is acceptable for the data sets used in this dissertation.

Also, the scattering parameters p and R have no “physical” correlation (beyond mathematical correlations) for two reasons. First, the theoretical approaches to describe the two scattering processes (surface roughness and grain boundary) are very different, namely via boundary conditions for the non-equilibrium distribution function for surface scattering and via relaxation time calculations for grain boundary scattering. Thus, p cannot be directly related to a scattering cross section whereas R can. Second, the scattering potentials are very different. p describes full reflection from a rough surface with no transmission, whereas R describes partial reflection and transmission from a delta-function-like potential. There is thus no attempt in the literature to describe the two contributions in a common framework. Both p and R are not materials parameters but depend on “extrinsic” properties, such as surface roughness, the cladding material, as well as the grain boundary type.

2.2 Material properties & resistivity scaling

As briefly discussed in the previous chapter, increased resistivity due to enhanced scattering at reduced dimensions has led to issues that are increasingly becoming unsustainable for copper-based interconnects [27], [33], [38]. Going forward, new materials would be required to replace copper to yield a lower line resistance and achieve a better reliability performance. In addition, it would be ideal if the alternative material does not require a diffusion barrier and an adhesion liner, does not poison the surrounding low-κ dielectric, has excellent thermal and chemical stability, is not hazardous to health, is cheap and easily available, and is compatible with the standard silicon manufacturing technology.

It has been argued that metals with a smaller mean free path than copper (thus having a bulk resistivity higher than copper) could, below certain length scales, have a resistivity smaller than copper [11]. A refined approach to the above argument was recently published [51] where, from first-principle calculations, it was inferred that elemental metals with a lower value of the product of the electron mean free path and bulk resistivity ($\lambda_0.\rho_0$) are expected to be less sensitive to the *finite size effects* and thus be more suitable for narrow interconnect lines. This argument directly follows from the semi-classical models of Fuchs-Sondheimer and Mayadas-Shatzkes which approximate the resistivity increase at smaller length scales to be proportional to the product of λ_0 and ρ_0. Using this new figure-of-merit, promising metals for future interconnect applications are the platinum-group metals such as ruthenium, rhodium, iridium, and osmium, along with nickel and cobalt (**Figure 2.5**). Additionally, these metals have a higher melting point than copper which potentially indicates better reliability [50]. Similar conclusions were reached in [50] where a low bulk resistivity combined with a high melting point were suggested as the figures-of-merit (**Figure 1.5**).

Another approach, stemming from the Drude or the free electron model (equation 2.17), proposes the electronic contribution (ne^2/m^*) as a figure-of-merit for selecting alternative metals [48].

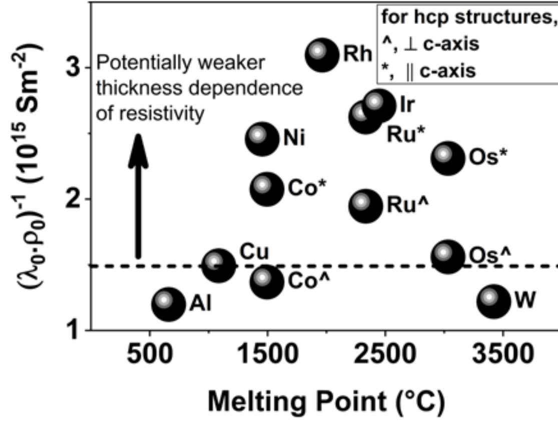

Figure 2.5 Computed inverse product of mean free path [51] and bulk resistivity $(\lambda_0.\rho_0)^{-1}$ for various metals plotted against respective melting points. A higher value of $(\lambda_0.\rho_0)^{-1}$ is desirable for a weaker thickness dependence of resistivity. Platinum-group metals such as Rh, Ir, Ru, Os, along with Ni and Co (∥ c-axis), have a better figure of merit than Cu.

$$\frac{ne^2}{m^*} = \frac{1}{\rho_0 \tau_0} \tag{2.20}$$

where, n: electron density, e: charge on an electron, m*: effective mass, τ_0: scattering time.

As the scattering time can be taken as a qualitative measure of the mean free path (a higher τ_0 would correspond to a higher λ_0), then from equation (2.20), a higher value of ne^2/m^* for a metal can be deemed promising to demonstrate a weaker thickness dependence of resistivity [48]. In addition, the cohesive energy was linked to the melting point and the vacancy-formation energy, and was reasoned to indicate better electromigration, thus reliability performance [48], [49]. A plot of cohesive energy *vs.* electronic contribution is presented in **Figure 2.6**. On both these figures-of-merit, platinum-group metals, such as ruthenium, rhodium, iridium, again score high, along with niobium.

Thus, per various figures-of-merit from the literature, including bulk resistivity, melting point, $\lambda_0.\rho_0$, electronic contribution, and cohesive energy,

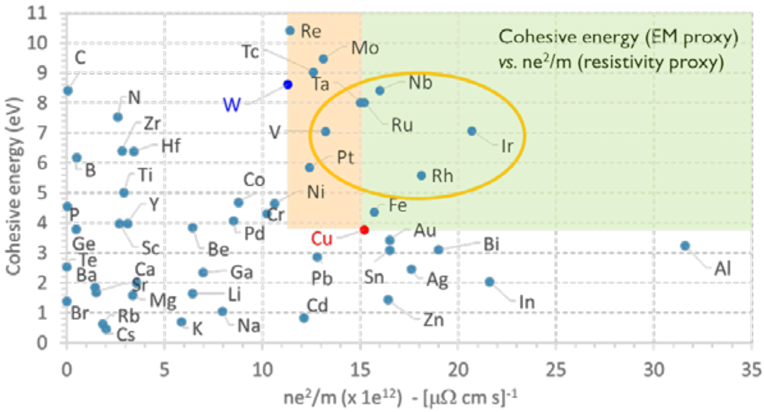

Figure 2.6 Cohesive energy *vs.* electronic contribution (ne^2/m^*) for various metals. Higher cohesive energy (indicative of a higher melting point, thus potentially better electromigration) and a higher ne^2/m^* (indicative of lower resistivity) are desirable. Platinum-group metals such as Ru, Rh, Ir, Pt score higher on both counts (Figure reproduced from [48]).

platinum-group metals, specifically ruthenium, rhodium, and iridium have consistently scored better and have proven themselves to be promising candidates to be explored as alternatives to copper metallization for interconnects in the future technology nodes. Other interesting candidates include nickel, cobalt, and niobium. In fact, cobalt is also being extensively researched for interconnect applications [108]–[112]. The impact of cobalt's ferromagnetism on its possible application as interconnects has not been reported in the literature yet.

Alloys and intermetallic compounds (including silicides, germanides) have also been proposed as worthwhile options to be explored for interconnect applications [113]–[124]. Arguments in support include: several possible alloy combinations, possibility that an ordered (intermetallic) phase results in a low resistivity phase that is lower than either of the constituents, better reliability (due to higher melting point), familiarity with processing and contamination (in case of alloys of aluminum, cobalt, copper), and low cost. However, no compelling experimental evidence exists at this point that demonstrates

markedly better performance over copper-based interconnects. Other drawbacks of the binary compounds include lack of conformal filling capability and the requirement of elevated temperatures for the formation of the intermetallic phase (that is typically not backend CMOS processing compatible). Further, allotropes of carbon - nanotubes [125]–[128] and graphene [127], [129], [130] - along with optical interconnects [131]–[133] are also being explored for possible applications in interconnects. Carbon nanotubes, so far, have yet to demonstrate silicon integrate-able solutions while the research on graphene for interconnects applications and optical interconnects is still in its infancy.

Drawbacks of the platinum-group metals include higher material cost, restricted familiarity with processing, and limited availability of conformal coating processes and related chemistry (including electro(less)plating, ALD precursors), with the notable exception of ruthenium. Concerns of higher cost could be allayed by the combined use of copper and the alternative metal in interconnects where the alternative metal is used only to fabricate the smallest interconnect structures where there is a definite gain over copper while the rest of the (larger, non-critical) interconnect structures are still made of copper. In addition, the cost of ruthenium has reduced by about 50% in the period 2012-2017 [134] owing to its increased use in various applications, especially in the microelectronics industry. Such trend could be expected for other platinum-group metals too as growing interest would drive up the production rates and reduce costs, unless the supplies are fundamentally limited. Familiarity with processing and availability of electro(less)plating and ALD chemistries would also improve once sufficient and compelling experimental evidence in support for interconnect applications comes into light for these metals.

2.3 Chapter summary

Enhanced scattering of charge carriers at the external interfaces and at the grain boundaries are the primary mechanisms through which resistivity increases in reduced dimensions. Over the years, several theories and models were proposed to describe and understand the contribution of these scattering mechanisms to resistivity. Each successive model is an evolution

upon the existing models typically accounting for additional physical parameters or interactions. The Mayadas-Shatzkes model for the case of arbitrary scattering at the interfaces is the most widely used model accounting both for the surface scattering as well as the grain boundary scattering. In spite of its limitations (to account for surface/interface roughness, possible confinement effects), the model does well to quantitatively describe the nature of the scattering mechanisms.

Literature reports significantly varying *p* and *R* values even for the same metal and this can typically arise not only from incorrect or inadequate assumptions (as has been discussed in this chapter), but also from the fact that the *p* and *R* values are not material intrinsic[10]. That said, there is room for systematic and methodical investigation into the surface and grain boundary scattering contributions to resistivity provided the input parameters (such as linear intercept length, bulk resistivity) are accurately determined (through microstructural characterization) together with a careful examination of the applicability of the model and its limitations.

Role of material properties in scattering mechanisms and reliability is also of technological relevance for interconnect applications in microelectronic circuits. Studies have suggested several figures-of-merit to shortlist potential metals for future interconnect applications, and include bulk resistivity, melting point, $\lambda_0.\rho_0$, electronic contribution, and cohesive energy. A lower product of mean free path and bulk resistivity together with a higher electronic contribution suggests a weaker thickness dependence of resistivity while a higher cohesive energy (thus melting point) was argued to be an indicator for potentially better reliability. The platinum-group metals seem promising, with ruthenium, rhodium, and iridium consistently outperforming copper in all aspects.

Other than elemental metals, binary alloys, intermetallic compounds, and quasi-two-dimensional materials (such as graphene, transition metal dichalcogenide materials) are also being investigated by several groups around the world, however are still in infancy.

[10]The *p* and *R* values may vary depending upon several factors, such as *cladding* and thermal treatment. This topic will be explored in detail in Chapter 4.

Chapter 3

Microstructure & Annealing Behavior

Problem Statement

Properties of materials are strongly affected by their microstructure. Thin polycrystalline films have a high degree of defects (including vacancies, dislocations, and grain boundaries) and interfaces, and thus the 'system' is in a state of high free energy. Due to kinetic limitations however, (most of) these defects do not vanish spontaneously and often require an activation energy (that may be higher than the thermal energy). Thermal processing enables the defects to passivate or rearrange themselves into a lower energy configuration. Thus, to be able to *manipulate* the microstructure and engineer the properties of the films, an understanding of the annealing behavior is paramount.

Little exists on the behavior and properties of thin platinum-group metal films as a function of the annealing temperature. Additionally, and as discussed previously, microstructural characterization is a key component in the semi-classical resistivity modeling of thin films[11].

[11]Topic of investigation in the next chapter

Objectives

This chapter aims to explore the microstructure and the annealing behavior of ruthenium films with thicknesses below 30 nm. Such investigations would shed light into the microstructural evolution with thickness and as a function of temperature, and their corresponding effect on the mechanical as well as the electrical properties. From a physical point of view, it would be of interest to explore how the atomistic processes such as vacancy diffusion and vacancy clustering affects the physical properties, and observe implications on the electrical properties.

The scope of microstructural investigation in this work is limited and is only to complement the analyses of the scattering effects discussed later in the dissertation.

Structure

Firstly, it is discussed how the microstructure of thin ruthenium films evolves with the thickness and the corresponding impact on stress. Then, the annealing behavior of thin films is investigated along with its impact on the mechanical and the electrical properties.

3.1 Microstructural transformations

Microstructure plays a crucial role in relation to the mechanical and the electrical properties of materials. Presence of deformations (including defects, dislocations) raises the free energy and the system as such is not thermodynamically stable at equilibrium. The evolution towards a lower energy configuration by reducing the free energy stored in the films is achieved through microstructural transformations that are driven thermodynamically. Such transformations are typically accompanied with changes in one or more (material or electrical) properties. It is to be noted that microstructural transformations may not necessarily be accompanied by phase transformations.

Microstructural transformations can be broadly classified into: recovery, recrystallization, and grain growth. Recovery is a relatively low temperature annealing phenomenon and corresponds to the annihilation or rearrangement of dislocations (line defects) due to atomic diffusion. It is driven by the energy stored in point-defects. The point-defects either cluster or get absorbed at the grain boundaries, dislocations, or at the surface. During recovery, the changes in the microstructure are relatively homogenous and typically have little effect on the boundaries between the deformed grains.

Recrystallization and grain growth have been reported to typically occur at higher temperatures (>0.33-0.50 of the melting point [135]) and have a definite impact on the microstructure. Recrystallization is characterized by the evolution of a new grain structure through the movement of high angle grain boundaries (HAGB) and is driven by the energy stored in the deformed structure. A simple definition of a high-angle grain boundary is when the misorientation angle between two adjacent crystals is greater than 10-15°. A typical high angle grain boundary is relatively disordered, with a high density of empty states [136]. They provide an easy path for mass diffusion in the solid state and are also preferential sites for solutes and impurities to segregate. During recrystallization, the new grains grow by absorbing the existing grains and need not necessarily assume the existing film texture. Several factors affect the process as well as the rate of recrystallization and include [137],

- **Degree of misorientation between grains**: high angle grain boundaries are known to have higher mobility (~100-1000x) than low angle grain boundaries [138].
- **Degree of stress/strain present in the film**: higher stress/strain reduces the recrystallization temperature.
- **Rate of annealing:** as physical mechanisms dictating recrystallization are activated thermally, the recrystallization temperature decreases for increased annealing durations. Additionally, the rate of recrystallization (reaction rate) follows the Arrhenius behavior and is an exponential function of the temperature.
- **Presence of impurities:** solute atoms present in the films tend to aggregate at the grain boundaries and may result in *solute drag*

whereby they retard the motion of the grain boundaries thus hampering the process of recrystallization. Several observations have been reported where minute amount of impurities have significant impact on the recrystallization temperatures [139], [140]. As an example, the recrystallization temperature of copper rose by 240°C with the addition of only 0.01% Tellurium [141].

After recrystallization, the system continues to be in a metastable state and the recrystallized grains may grow further. This grain growth is achieved by the movement of grain boundaries and is driven by the energy stored in the grain boundaries. The grain size has been traditionally used to optimize the mechanical properties such as strength and toughness. It also affects the electrical properties as grain boundaries are an impediment to the flow of charge carriers and a lower density of grain boundaries would result in a drop in the resistance. Factors affecting grain growth include temperature, texture, and impurities. Typically, the various phases of microstructural transformation needn't necessarily occur in a sequence and more than one process may occur simultaneously. In literature, recrystallization and grain growth have been reported to occur in an overlapping manner [142].

3.1.1 Microstructure of thin Ruthenium films

(Thin) film deposition processes are generally non-equilibrium; the as-deposited films are not in the most stable state, and is due to kinetic constraints imposed, thus resulting in non-equilibrium microstructures. The grain structure of such (polycrystalline) films are highly constrained. This affects the mechanical as well as the electrical properties of the films. The films can often be textured, meaning the grains favor a particular crystallographic orientation. The evolution of microstructure in thin films though is highly dependent on the deposition conditions, and several theories and growth models have been proposed to explain the microstructural evolution [143]–[147].

Ruthenium films of various thicknesses were sputter deposited on SiO_2. All films were polycrystalline as-deposited with the presence of the (002) plane ($2\theta \sim 42.15°$) and a feeble (101) component ($2\theta \sim 43.85°$) (**Figure 3.1 (a)**). For

Ru, the (002) texture has the lowest surface energy [148]. The average out-of-plane crystallite size was calculated using the Scherrer equation[12] [149] (**Figure 3.1 (b)**). It can be seen that the films are almost equiaxed; and the in-plane (measured from TEM images, **Figure 3.1 (c)-(e)**) and the out-of-plane grain size are similar. The out-of-plane crystallite size is almost equal to the film thickness for films upto 10-15 nm in thickness and deviates for films >15 nm in thickness. This is likely due to a competing mechanism between the lateral and the vertical growth in the structural evolution which causes the observed deviation.

Arguably, the most simple and still widely used model for sputtered films is the Zone model[13] [143]. The zone model indicates that, in the limit of thick films, textured films with columnar grains are expected. During the initial stages, the deposition of metal thin films will initially proceed by island nucleation, island coalescence, and further growth. If the initial nucleated grains are not textured, there might be a phase where the texture is formed, which is typically ascribed to a faster growth rate of the grains with the right orientation. However, there is no indication that such a phase exists and it will be rather challenging to detect it for polycrystalline films.

Column-like microstructures are rather typical for metal films. A schematic for a film with equiaxed and non-equiaxed columnar grains is shown in **Figure 3.1 (g)**. It can be imagined that in the limit of thin films, even a non-equiaxed grain structure would demonstrate a bamboo-like structure. With

---

[12]Average out-of-plane domain (crystallite) size, $\tau = K_s.\lambda_x/(\beta.\cos\theta)$. K_s is the shape factor (typically between 0.9 and 1), λ_x is the wavelength of the radiation source, β is the FWHM, and θ is the Bragg angle. Due to instrument-related broadening, dislocations, and the uncertainty in the shape factor, the crystallite size determined by the Scherrer equation are typically underestimated. The error margin can vary depending on the instrument setting and the grain shape. It is not possible to separate effects of grain size and microstrains e.g. in a Williamson-Hall approach, since there is only one peak visible in the XRD patterns of the textured films. Also, it is doubtful if a Williamson-Hall analysis would really lead to a more quantitative analysis of the grain size.

[13]It is to be noted that films can grow in several different ways. The zone growth model is a very basic one and certainly does not encompass all possible scenarios, however serves as a good starting point.

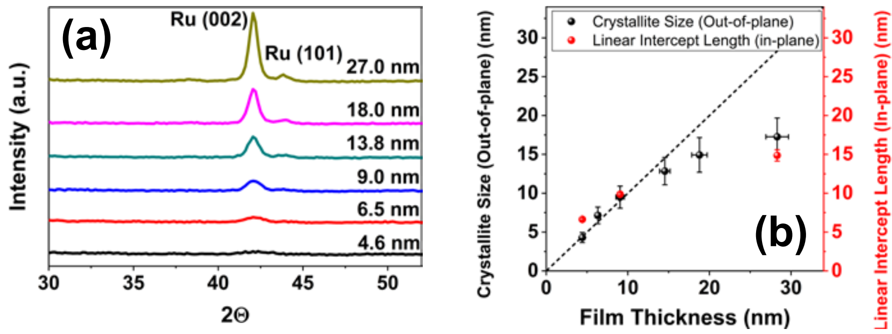

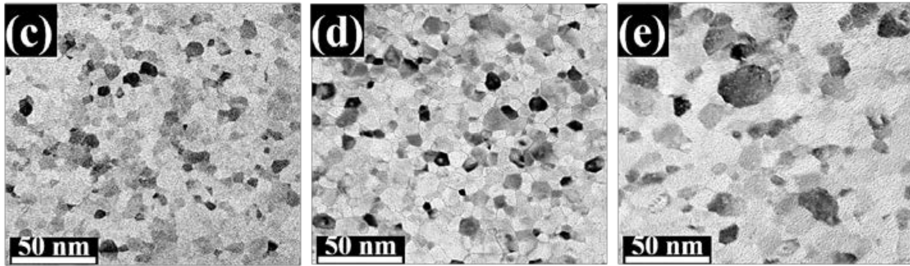

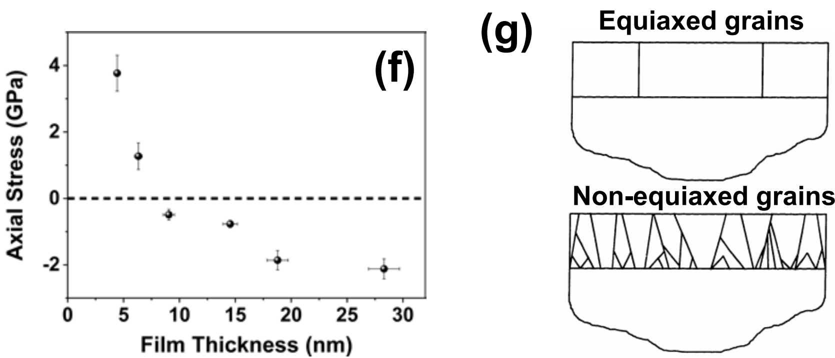

Figure 3.1 (a) X-ray diffraction pattern of various (nominal) thicknesses of sputtered ruthenium films on SiO_2. (b) In-plane and out-of-plane crystallize size. (c) – (e) In-plane TEM images of nominally thick 5, 10, and 30 nm ruthenium films as-deposited (c, d, and e respectively). (f) Axial stress (or the in-plane stress) as a function of thickness. (g) Schematic of a cross-sectional view of equiaxed and non-equiaxed grains (Figure reproduced from [150])

increasing thickness, the overall structure may deviate where the in-plane and out-of-plane grain sizes are still similar but needn't necessarily be equal to the film thickness. The data on ruthenium films presented here are in general consistent with such a growth model. In addition, no significant changes of the lateral correlation length of the surface roughness have been observed for all materials and substrates. TEM measurements of the linear intercept length of as deposited films are only available for Ru on SiO_2 and values for 5, 10, and 30 nm thick films are within experimental errors.

The thinnest as deposited ruthenium film, of ~3 nm, could not be studied in detail by TEM due to resource limitations. However, AFM measurements are not consistent with a corrugation of the order of the film thickness (with RMS roughness of 0.17 nm) and indicate that the film is rather closed. While this does not rule out the presence of individual pinholes, it indicates that the films are certainly well beyond percolation. Models for the sheet resistance of partially non-continuous films exist and show that the effects due to individual pinholes are negligible and strong increase in the sheet resistance is only expected near percolation[14].

The non-equilibrium microstructures can create stress in the films. It has been reported that thin polycrystalline films with small grains (as observed for the ruthenium films here) typically constrain relaxation mechanisms, and thus such films could build very high intrinsic stresses (upto several GPa) [146], [147], [151]. Several stress inducing mechanisms exist [145]–[147], [152]–[154] and play a role. However, there is general acceptance that grain boundary regions are associated with excess free volume and thus thin films with small grains (thus higher cumulative volume of grain boundary region) would result in high tensile strain [147], [152], [154], [155]. This is what is observed for the 5 nm as-deposited ruthenium film with a tensile stress of ~3.7 GPa (**Figure 3.1 (f)**; calculated through the assessment of the Ru (002) peak position)[15]. Increased grain size at higher thicknesses leads to a

---

[14]It shall be later seen in Chapter 4 (Figure 4.4) that the resistivity of the 3 nm film does not increase drastically as one would expect in case pinholes are present.

[15]According to Bragg's law, the interplanar distance, d, is inversely proportional to the scattering angle, θ. So, any deviations from the relaxed peak position suggests that the films are strained. A shift in the peak position towards a higher value than the relaxed position indicates a decrease in interplanar spacing leading to compressive

reduction in the free volume and thus the magnitude of tensile stress reduces. However, for films thicker than 10-15 nm, a stress-reversal is observed where the nature of the stress flips from tensile to compressive in the axial direction. This stress reversal point in thickness is coincidental with the deviation of the out-of-plane crystallite size from the films thickness (out-of-plane crystallite size < films thickness) (**Figure 3.1 (b)**). This can be explained by a combination of increasing grain size (leading to reduced free volume associated with the grain boundaries acting to reduce the tensile stress) and the 'atom insertion model' at the grain boundaries which acts to increase the compressive stress [153]. It has been argued that during the film growth, atoms are inserted in the grain boundary triple junction[16] that result in compressive stress[17] [153]. With increasing thickness, the grain size also increases along with the cumulative amount of the atoms that have been inserted into the grain boundaries. Thus, the magnitude of the compressive stress also increases with the thickness[18]. This sufficiently explains the observations made for the evolution of the stress as a function of thickness in the ruthenium films in this work.

In literature, stress in ruthenium films have been measured whereby its nature and magnitude has been found to strongly depend on the deposition conditions. For sputter deposited ruthenium films of 50 nm thickness, a compressive stress was observed between 2.5 and 4 GPa depending on the

---

strain in the transverse direction. Due to the Poisson effect, this would lead to an axial tensile strain. The magnitude of stress in the films can be calculated as described elsewhere [156].

[16]Triple junction is a junction between the two grain boundaries and the surface.

[17]The compressive stress due to the atom insertion model can be understood as follows: the insertion of atoms at the grain boundaries would result in an increase in the density which is equivalent to the presence of compressive stress.

[18]In addition to the insertion of material at the grain boundaries, another effect called the ion peening [157] could also contribute towards the increased compressive stress as a function of increasing film thickness. This model argues that films deposited by sputtering would be under compressive stress due to the effect of ion bombardment on the grains. However, this does not explain the stress dependence of the grain size and is thus typically discounted. In this work, ion-peening might additionally add compressive stress to the ruthenium films, the magnitude of which might increase as a function of thickness.

deposition parameters [158]. In this work, it is seen that films thicker than 15 nm begin to develop compressive stress and stress in a 30 nm film was observed to be ~2 GPa. In contrast, much thicker films (of the order of μm; exact thickness not known) deposited by MOCVD have a tensile stress of only 70 MPa [159]. The exact reasons are not probed in this study and could include, but not limited to, a vastly different nucleation mechanism, higher growth temperatures, and grain structure (as typically observed in films deposited through a chemical process [160]). Thus, the magnitude of stress in thin films can depend strongly on the deposition process. As a side-note, the presence of tensile stress in films can also lead to stress-induced grain growth with time and can result in the lowering of sheet resistance. Such self-annealing observations have been made for copper films prepared by electrochemical deposition [161].

3.2 Annealing behavior

Microstructural transformations in thin films during annealing can be studied by in-situ measurements.

X-ray diffraction can be an effective technique to monitor microstructural transformations in films under thermal treatment. Here, the sample is heated to a given temperature at a fixed heating rate and a linear detector recurrently captures the diffraction patterns. This way, changes in microstructure as a function of temperature can be monitored continuously.

The in-situ XRD spectra of ruthenium films (sputter deposited on SiO_2) of thicknesses between 5 and 30 nm is shown in **Figure 3.2**. A ramp rate of 1°C/s and a reducing ambient of $He+H_2$ was used. As discussed earlier, the as-deposited ruthenium films were polycrystalline. At temperatures above 400 - 450°C, the films began to recrystallize and strongly texture towards the (002) plane[19] resulting in the observed increase in the peak intensity.

[19]Films upon recrystallization can also assume a different texture than their as-deposited phase. This depends on the interplay between various factors with the goal of maximizing strain-energy release (and assuming the lowest possible energy configuration).

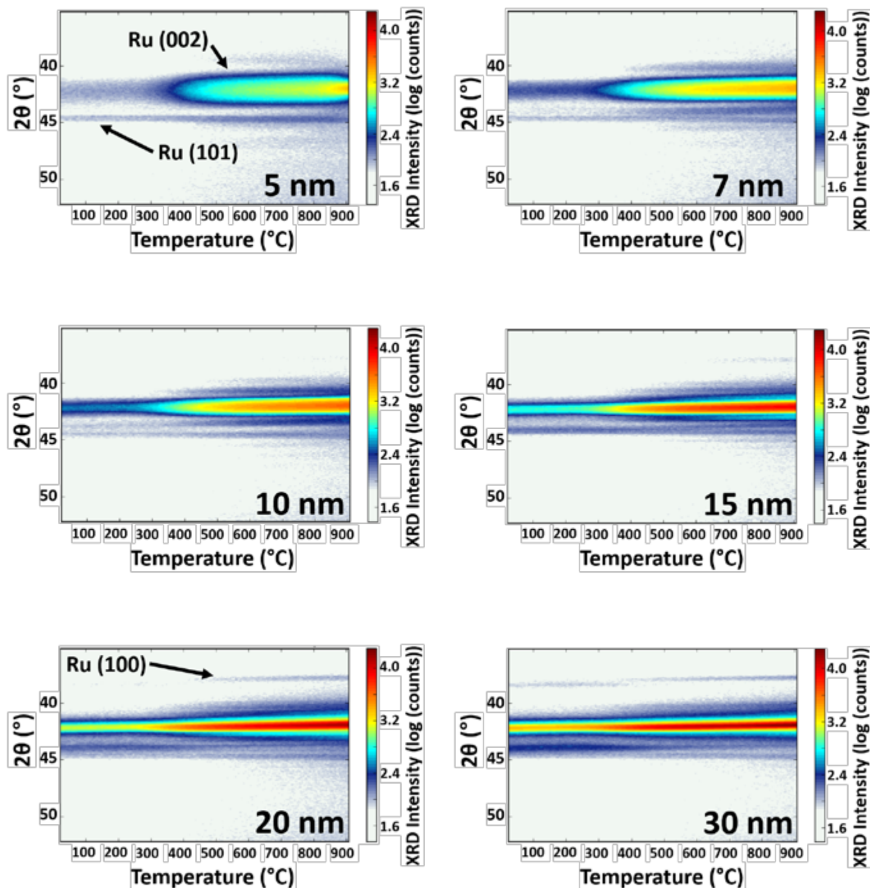

Figure 3.2 X-Ray diffraction spectra as a function of temperature of thin ruthenium films (of nominal thicknesses 5, 7, 10, 15, 20, and 30 nm) deposited on SiO_2. The as-deposited films are polycrystalline with a higher proportion of (002) phase along with a weak presence of (101) phase. Films are observed to recrystallize ~400-450°C. (Ramp rate: 1°C/s; Ambient: He+H_2)[20]. Maximum error in temperature scale is 20°C between 300°C and 600°C.

[20]In-situ x-ray diffraction/sheet resistance measurements carried out at the Department of Solid State Sciences (Conformal Coating of Nanomaterials Research Group), Ghent University, Krijgslaan 281 S1, 9000 Gent, Belgium.

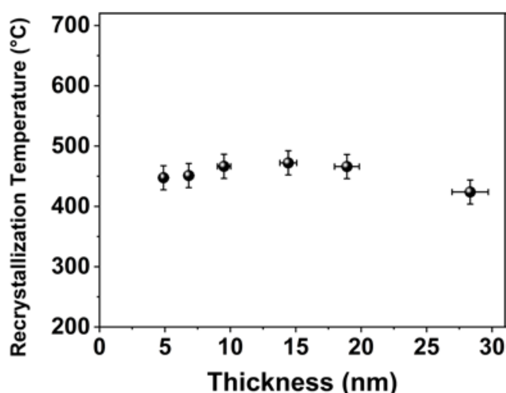

Figure 3.3 Recrystallization temperature of Ru films sputter deposited on SiO_2. Low recrystallization temperature is observed (about a quarter of the absolute melting temperature) with no obvious signs of thickness dependence within the error bars.

Continuous, albeit slow, increase in the peak intensity at higher temperatures indicate that the crystallites do continue to grow, but slowly.

The recrystallization temperature (T_{recrys}) of the ruthenium films was found to vary between 410 and 470°C for films between 5 and 30 nm (**Figure 3.3**) without showing a monotonic increase or decrease. Within the error bars, there was no clear sign of the thickness dependence of the recrystallization temperature. This is in stark contrast to the observations for silicon [162], [163] and metal-oxides [164]–[166] that exhibit a strong, inverse thickness dependence of the crystallization temperature. As the average grain size increased with the thickness of the ruthenium films (**Figure 3.1 (b)**), the grain boundary density reduced accordingly. As the grain boundaries are favored nucleation sites for recrystallization [140], it was expected that the recrystallization temperature would have increased with the film thickness. In addition, stress has also been reported to reduce the recrystallization temperature [140]. Absence of such an observation indicates that the decrease in the average grain boundary density for thicker films and stress (even in the magnitude of GPa) is not sufficiently large to lead to significant changes in the recrystallization temperature. Nevertheless, the low values of recrystallization temperature observed for ruthenium films in this work

(~0.27x of the absolute melting temperature) is somewhat lower than the earlier findings where the recrystallization temperature for bulk metals was reported to be 0.33-0.50 of the absolute melting point [139]. Copper, in comparison, has been reported to recrystallize at 120-370°C depending on the alloying material and the atomic percentage [139], [140].

A few reasons for the lower recrystallization temperature observed here for ruthenium and the commonly reported values (~0.27 *vs.* 0.33-0.50 of the absolute melting point) reported in earlier literature [139] could be impurity content[21] and/or defect concentration[22] [140]. The impact of these factors on the recrystallization temperature of ruthenium films is beyond the scope of this work.

The question of how interfacial defects affect the recrystallization of thin metal films is in principle relevant. It is not straightforward to evaluate the energy of the incoming ruthenium particles after sputtering and whether the sputtering of ruthenium onto itself could generate defects. The ruthenium films were sputtered in a 300 mm Canon Anelva sputter tool. No DC bias was applied during the deposition. There will be some "natural" bias but the quantification is not possible. The use of simplistic models such as that of Sigmund-Thompson [168] energy distribution of sputtered particles can be misleading if caution is not exercised. The model predicts that the sputtered atom energy has a maximum at approximately half of the surface binding energy. The surface binding energy is not trivial to calculate and typically the sublimation energy is used instead. Ruthenium's sublimation energy has been

[21]Higher recrystallization temperatures reported in literature were predominantly for bulk metals of 'commercial purity' (roughly between 95 and 99% purity). The ruthenium films used in our work were sputter deposited from a target of 4N purity (99.99%). It has been observed in the literature that presence of 0.1% impurity can drive up the recrystallization temperature by 100°C [139], [140]. For copper, the recrystallization temperature has been reported to increase by 15°C even for a 0.01% (atomic) alloying with cobalt and up to 240°C with tellurium for the same alloying percentage [167]! As such, *solute drag*, where the impurities segregate at the grain boundaries and retard their motion, could explain the differences in the recrystallization temperature.

reported to be ~ 6.4 eV [169] and, from the Sigmund-Thomson model, this would imply the maximum of the energy distribution to be ~3.2 eV. However, it must be clearly understood that the above simplification fully disregards several factors, including the energy of the bombarding species, and the possible interaction of the sputtered atom with the plasma and with its own species. It is difficult to exactly deduce the energy of the incoming atoms given the complexity of the physical processes involved.[23]

Literature too lacks a descriptive understanding of the topic. As a matter of fact, there is essentially no literature on the recrystallization of thin Pt-group metal films as such. Moreover, the characterization of such interfacial defects is challenging and the effects on recrystallization may be masked by other influences, such as microstructure, initial stress, and/or purity. Therefore, this topic was not elaborated further in the thesis.

3.2.1 Impact on stress evolution

The evolution of stress as a function of the annealing temperature is studied indirectly by continuously monitoring the ruthenium (002) peak position. Such in-situ measurements allow for the dynamic changes in the stress to be captured and can provide valuable insights into the physical mechanisms.

The onset of strain relaxation can be observed ~150-200°C in the 30 nm ruthenium film (**Figure 3.4**), which is much lower than the recrystallization temperature of ~450°C. Hence it is not likely that recrystallization could be the physical mechanism amounting to stress release observed >150-200°C. The relaxation continues further with temperature and begins to saturate ~450°C. This means that recrystallization and further grain growth do not

[23]The tool manufacturer, Canon, claimed that accurate calculations of the above energies were neither available nor possible. The sputter tool is used in this work is capable of producing multilayers consisting of much thinner films down to the monolayer range with excellent interface quality and minimum intermixing. It should also be noted that all XRR data systematically obtained the ruthenium samples are consistent with the physical roughness obtained for the SiO_2 surface before deposition (about 2 to 3 Å RMS). This qualitatively indicates that interfacial intermixing will therefore be rather weak and rather confined to a monolayer at most.

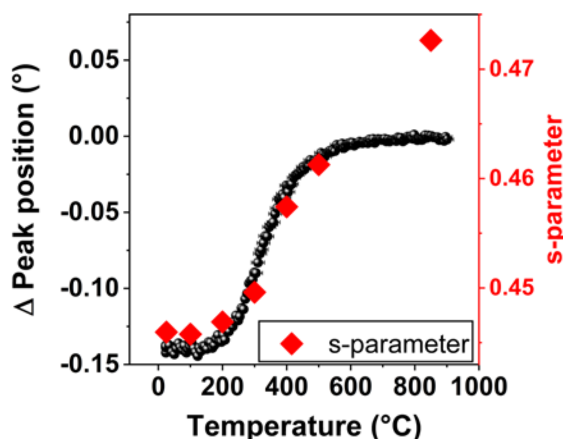

Figure 3.4 Change in lattice parameter (taken as an indication for stress evolution) of the (002) plane as a function of annealing temperature for a 30 nm Ru film (corrected for thermal expansion). A change in lattice parameter can be observed > 150-200°C indicating stress relaxation. The s-parameter, from the positron annihilation spectroscopy[24], for a 30 nm Ru film is also observed to increase >200°C (an indication of vacancy clustering), coincident with the temperature range for stress relaxation. The continuous rise in the s-parameter indicates continued vacancy clustering and high stability of those clusters.

significantly impact the stress state in the film. In literature, relaxation of (compressive) stress in comparatively thicker ruthenium films (200 nm) has been shown to occur at temperatures of 350-550°C [170], in reasonable agreement with our results.

A possible mechanism for stress release observed in ruthenium films here could be vacancy migration and clustering. To test the hypothesis, positron annihilation spectroscopy (PAS) measurements (a sensitive technique to detect open-volume type defects in materials [171]) was carried out on the 30 nm thick ruthenium film. In this technique, positrons are injected in a sample intended to be studied and are expected to be annihilated by the electrons

[24]PAS measurements courtesy Prof. Akira Uedono, Division of Applied Physics, Faculty of Pure and Applied Science, University of Tsukuba, Tsukuba, Ibaraki 305-8573, Japan

releasing energy in the form of photons (gamma rays), energy of which is dictated by the momentum of the annihilating electrons and positrons. Due to the finite momenta of the electron-positron pair, they lose their energy in the form of phonons and thus the energy spectra of the photons assume a Gaussian distribution. When a sample contains vacancies, the positron wavefunction is localized and annihilates at a slower rate as compared to rest of the bulk. This affects the resultant energy spectra (positrons residing in the vacancies would not lose further momentum until annihilation and thus distort the resulting energy spectra). The distortion in the energy spectra is quantified by the s-parameter (or the line shape parameter) which is the ratio of the center portion of the Gaussian distribution to the entire distribution. The s-parameter in itself is not of much significance but what is more important is the change in its magnitude. The presence (and clustering) of vacancy-type defects in a sample narrows the distribution, thus causing an increase in the s-parameter. It is of note that, during agglomeration, the net vacancy concentration would decrease. Because of the high positron sensitivity for vacancies, however, almost all positrons are trapped by defects. Thus, no information could be deduced on the defect concentration.

The variations in s-parameter, which is a qualitative measure of the defect size, is observed to increase at >200°C for the 30 nm ruthenium film (**Figure 3.4**). The increase in the s-value can be attributed to the clustering of vacancy-type defects in the metal film, which unambiguously indicates vacancy migration. The vacancies are most likely to cluster at the grain boundaries as they act as trap sites [172], [173]. For copper, vacancy-type defect mobility has been found to be sensitive to the structure of the grain boundaries [174]–[176]. Also, simulations have shown that defect content can also affect the grain boundary structure [177].

Furthermore, the s-parameter continues to increase even after recrystallization till the highest measured temperature of 850°C, indicating continuous net vacancy clustering. This is in contrast with reports on (electroplated) copper where increase in the s-parameter is observed for annealing below 200°C, and a decrease in the s-parameter is observed for annealing above 300°C signifying dissociation of vacancy clusters and saturates at the annealing temperature range of 600-700°C [178]. The lower threshold for vacancy diffusion for copper when compared to ruthenium

could be linked to their respective vacancy diffusion activation energies (E_{vm-Cu}: 0.72 eV, E_{vm-Ru}: 2.18 eV [31]). The fact that the s-parameter does not decrease till 850°C indicate high stability of the vacancy clusters in ruthenium. Thus, it is learnt that stress relaxation in thin ruthenium films is strongly coincident with vacancy clustering and is predominantly a low temperature process. Relatively high temperature phenomena like recrystallization and subsequent grain growth does not have significant implications on the stress relaxation behavior.

3.2.2 Impact on electrical resistance

As has been discussed in the previous sections, annealing has a significant impact on microstructure, texture, and stress in thin films, all of which can have an influence on the electrical resistance. The movement and clustering of point defects release stress and reduce the total volume associated with point defects[25] and could thus reduce the potency of such scattering centers for charge carriers [179]. Additionally, the increase in grain size upon annealing amounts to a decrease in the density of grain boundaries per unit length that acts to reduce the resistance to the flow of charge carriers. Also, as ruthenium packs as a hcp crystal lattice and has a non-spherical fermi surface, the conduction of charge carriers is anisotropic. Recrystallization upon annealing might affect the film texture, thus resistivity, in the direction of the flow of current (the final resistivity after recrystallization however will also depend on the grain size distribution). Thus, it is indeed intriguing to explore the impact of the above process(es) on the electrical properties of the thin ruthenium films.

The sheet resistance (measured through the four-point technique) as a function of temperature of a 30 nm ruthenium film is shown in **Figure 3.5**. As evident, the onset of vacancy clustering and stress relaxation ~200°C is coincident with the instance when the resistance starts to decrease, though the impact is rather small (< 5%). In fact, up until 300°C, the decrease in resistance is only ~10%. Though the reduction is not significant, this

[25]A vacancy can be visualized as a sphere. So, clustering of vacancies (analogous to Oswald ripening) would result in a surface area that is smaller than the combined surface areas of all individual vacancies.

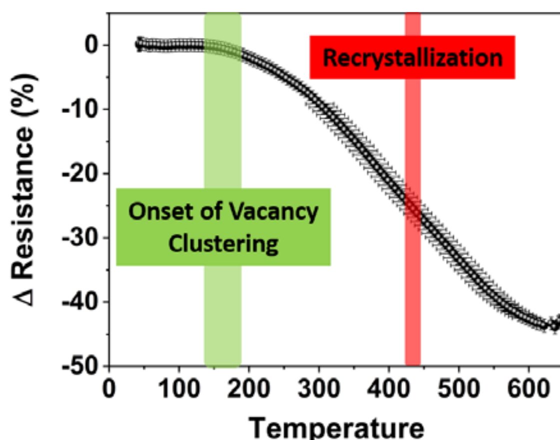

Figure 3.5 Change in sheet resistance of a 30 nm ruthenium film as a function of annealing temperature. Resistance values are corrected for temperature coefficient of resistance. (Error bars on the temperature only available between 300°C and 600°C; resistance measured using four-point probe with high accuracy). Annealing was carried out in a reducing ambient of He+H_2 with a ramp rate of 1°C/s.

however indicates that the low temperature phenomenon of recovery and vacancy clustering indeed measurably affects the electrical behavior of thin ruthenium films.

Beyond 300°C, the rate of decrease in resistance becomes more pronounced and a reduction of ~30% from the room temperature value is observed till the recrystallization temperature. This can primarily be attributed to recrystallization occurring in an overlapping manner with recovery[26]. Though the texture upon recrystallization does not deviate from the as-deposited texture (**Figure 3.2**), the grains grow by virtue of the movement of (predominantly) high angle grain boundaries, which are known to have a greater energy as well as mobility than low angle grain boundaries[27]. This

[26]Recovery and recrystallization have been reported to occur in an overlapping manner [135].

[27]Significant differences in mobility, upto 100-1000 times, between high angle (>15°) and low angle (2-5°) grain boundaries in copper have been reported [140].

increased grain size translates into a longer mean linear intercept length and would drive the resistivity lower. Additionally, HAGBs are known to have a higher density of defects at the interfaces [180], (a significant fraction of) which upon annealing metamorphize into LAGB. Thus, both, the reduction in grain boundaries per unit length as well as reduction in the density of HAGBs, act to reduce the overall sheet resistance upon recrystallization.

Further reduction in resistance beyond 450°C can be attributed to subsequent grain growth post recrystallization. The reduction is significant and is ~45% when compared to the resistance at room temperature, which begins to saturate ~600°C. The film is not crystalline yet and could, in theory, has a room for the grains to grow further. The saturation suggests that the activation energy is much higher for the remaining grains to grow.

Thus, the gains of annealing in lowering the sheet resistance are limited to ~600°C and further annealing does not seem to have beneficial effects on resistance.

3.3 Chapter summary

The focus of this chapter has been to investigate the microstructure of thin ruthenium films and study the impact of annealing on the mechanical and the electrical properties.

The microstructure evolution of sputter deposited ruthenium films was studied. Films initially grow in an equiaxial manner and begin to deviate afterwards due to competing growth between the lateral and vertical grains. Such a deviation was found ~15 nm for the ruthenium films studied in this work. The microstructure evolution with thickness was also linked to the stress in the films. The stress was found to be highly tensile in the thinnest film of 5 nm and was attributed to the high density of grain boundaries (due to smaller grains) that are typically associated with tensile stress. As the grains grow, the grain boundary density reduces and the tensile stress reduces sharply, as seen for the 7 and the 10 nm films. Thereafter, as the microstructure evolves further, the stress in the films switch from tensile to compressive and can be explained through the 'atom insertion' and cumulative 'ion peening'.

Annealing behavior of the ruthenium films was studied and it was found that films recrystallize at much lower temperatures in relation to their melting point (~0.27x) and show almost no thickness dependence. This is in contrast with what is known for oxides and even for other bulk metals. Thus, metals in smaller dimensions show properties that deviate from their bulk behavior.

Further investigation reveals that stress release in ruthenium films can already be achieved at low temperatures, and relatively high temperature effects like recrystallization and grain growth had little impact. In contrast, low temperature treatment had little influence on the electrical properties of the films whereas recrystallization and subsequent grain growth led to significant reduction in the resistance.

Chapter 4

Scattering Mechanisms in Thin Films

Problem Statement

Resistivity scaling in metallic thin films have been extensively researched due to immense scientific and technological interest. The transport properties vary significantly in reduced dimensions than bulk due to the additional scattering mechanisms that come in play. Though this behavior is observed in all metals, there is no consensus on the relative contribution of the scattering mechanisms in scaled structures for copper as well as for the platinum-group metals. Additionally, as has been discussed in chapter 2, platinum-group metals like ruthenium, rhodium, and iridium are expected to be less sensitive to size effects than copper due to a lower product of the mean free path and the bulk resistivity. However, such a crossover in resistivity with copper is yet to be experimentally demonstrated.

Results from this chapter have been published in:

S. Dutta, K. Sankaran, K. Moors, G. Pourtois, S. Van Elshocht, J. Boemmels, W. Vandervorst, Z. Tokei, C. Adelmann, "Thickness dependence of the resistivity of platinum-group metal thin films," *Journal of Applied Physics*, vol. 122, no. 2, p. 025107, Jul. 2017, doi: 10.1063/1.4992089.

Objectives

The primary goal of this chapter is to understand the scattering mechanisms in thin films (<30 nm) of platinum-group metals.

Structure

The material characteristics (texture, grain size, RMS roughness) of the thin platinum-group metal (ruthenium, rhodium, palladium, iridium, platinum) films are quickly visited. Then, the thickness dependence of the resistivity is discussed. This is followed by a detailed examination of the contribution of the surface and the grain boundary scattering mechanisms to resistivity. Finally, the effect of the mean free path on the thickness dependence of resistivity is explored.

4.1 Material characterization

Films of thicknesses below 30 nm of various platinum-group metals (except Osmium) were sputter deposited[29]. All films were polycrystalline in their as deposited state. From the x-ray diffraction measurements, the Θ-2Θ patterns were found to be consistent with the expected crystal structures of the stable phases (hcp for ruthenium, fcc for all other metals) with (partial) texture [(002) for ruthenium, (111) for other metals]. Post deposition annealing at 420°C in forming gas for 20 minutes improved both the crystallinity and led to strong texturing (**Figure 4.1**).

The purpose of annealing (of the different ruthenium film series) was to generate samples with different microstructure (grain size) and to check for the robustness of the modeling results. The general idea was to vary processing methods such as deposition, substrates, and recrystallization to generate different series of ruthenium layers with different thickness

[29]Deposition methods and measurement techniques have been described in Appendix A

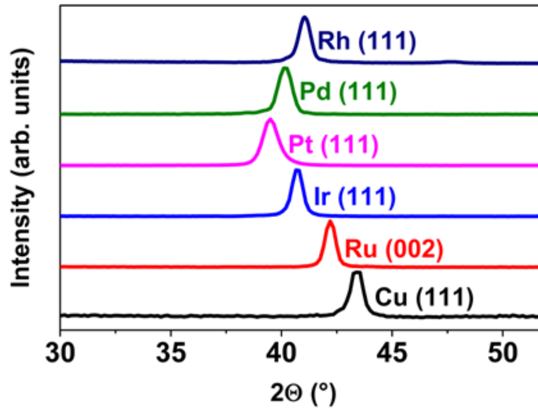

Figure 4.1 Θ-2Θ XRD pattern of 20 nm thick films of platinum-group metals and Cu, as indicated (Ru was deposited on SiO_2). All layers have been annealed at 420 °C for 20 min. The patterns indicate strong (111) texture for fcc materials (Rh, Pd, Pt, Ir, Cu) and (002) texture for hcp Ru.

dependences of the microstructure. All these methods are, in principle, equivalent. Ideally, there is no expected explicit effect of annealing on resistivity beyond microstructure (and potentially interface and surface roughness).

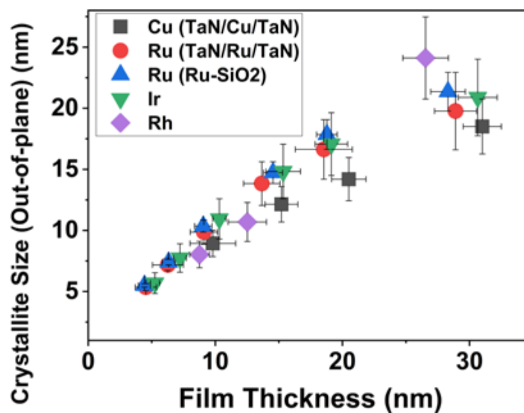

Figure 4.2 Out-of-plane Scherrer grain (crystallite) size determined from the XRD pattern.

The choice of annealing conditions (none or 420°C/20 min) was determined by several factors. The number of annealing conditions was limited by the available TEM resources. Annealing at too high temperatures (>650°C) led to decohesion of the metal films on SiO_2 and was thus not suitable. Annealing at lower temperatures (below 300°C) would not be very useful either as the in-situ sheet resistance measurements on PVD ruthenium films showed very little changes in resistance below 300°C (**Figure 3.5**). Thus, a single annealing temperature was chosen. Additionally, for ruthenium, different substrates (which also affects the grain size) were used to vary the microstructure. The annealing at a single temperature (compared to annealing e.g. at always the recrystallization temperature) led to a better comparability of the resistivity values for a given thermal budget and to more technologically relevant data. For this reason, the annealing temperature was kept the same for all materials and samples. Concerning the annealing time of 20 minutes, the impact of temperature on the film crystallinity essentially saturated around 20 minutes. This led to good process control while minimizing process times.

The out-of-plane Scherrer crystallite size of annealed films (**Figure 4.2**) was typically of the order of the film thickness for films up to about 15 nm and deviated slightly towards smaller values for thicker films. This indicates that the out-of-plane crystallite (domain) size was of the order of the films thickness.

Figure 4.3 shows the root-mean-square (RMS) roughness obtained from AFM measurements of copper (TaN/Cu/TaN), ruthenium (both Ru/SiO_2 and TaN/Ru/TaN), iridium, palladium, rhodium and platinum films as a function of the film thickness after post deposition annealing at 420 °C. The roughness of the annealed films increased with increasing film thickness but remained below 0.4 nm even for 30 nm thick platinum-group metal films. Copper films were slightly rougher with RMS values of 0.5 to 0.6 nm for the thickest films. XRR measurements (not shown) indicated that the roughness of the top surface was very similar to that of buried interfaces (typically also 0.3 to 0.5 nm). The lateral correlation length ξ of the surface roughness was between 10 and 15 nm for all films with insignificant differences between materials/stacks and only little coarsening in the studied thickness range up to 30 nm.

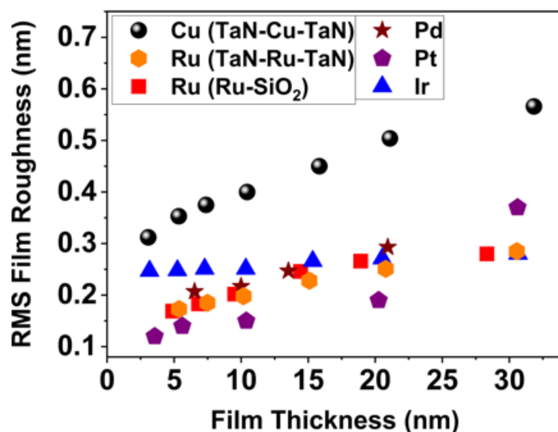

Figure 4.3 RMS surface roughness obtained from AFM measurements of thin platinum-group metals and Cu films as a function of their thickness. Error on the measurements are <0.04 nm. All films annealed at 420°C for 20 min

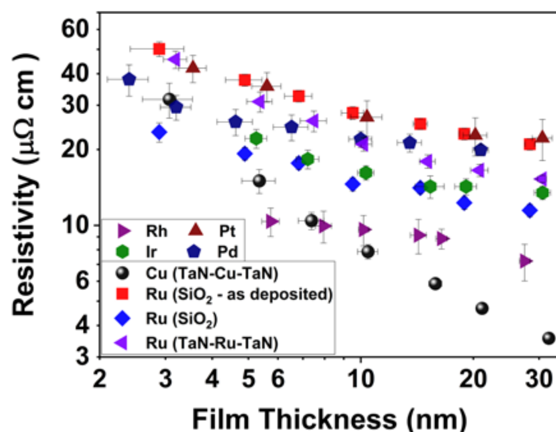

Figure 4.4 Thickness dependence of the thin film resistivity of platinum-group metals and copper, as indicated. All platinum-group metals thin films showed a much weaker thickness dependence of the resistivity than copper. For film thicknesses 8 to 5 nm and below, the resistivities of Rh, Ru, and Ir are comparable and even lower than the resistivity of copper. All films have been annealed at 420 °C for 20 min, except Ru (SiO_2 – as deposited).

Figure 4.4 shows the resistivity of copper (TaN/Cu/TaN), ruthenium (Ru/SiO_2 and TaN/Ru/TaN), rhodium, palladium, iridium, and platinum as a function of the film thickness. All films were annealed at 420 °C for 20 min in forming gas (except Ru on SiO_2, as deposited). Copper showed a strong increase with decreasing film thickness, as observed previously and ascribed to the combination of surface and grain boundary scattering. Note that the copper resistivity values were close to the ones reported in the literature for scaled copper interconnect lines of the same critical dimension [181].

By contrast, thin films of all platinum-group metals showed a much weaker thickness dependence of the resistivity than copper. For films with thicknesses of 10 nm and above, the resistivities were much higher than for copper owing to the higher bulk resistivities of the platinum-group metals. However, for film thicknesses of about 8 nm and below, the resistivities of rhodium, ruthenium, and iridium became comparable and even lower than the resistivity of copper. This observation could be linked to the predicted weaker thickness dependence of resistivity of the platinum-group metals due to a lower product of ρ_0 and λ_0 discussed in the earlier chapters. More will be investigated by semi-classical modeling of thin films in the next sections.

From a more fundamental point of view, these data raise the question of the material dependence of the thin film scattering contributions, such as surface and grain boundary scattering. It has been asserted that a shorter electron mean free path leads to a weaker thickness dependence of both surface and grain boundary scattering [45], [46], [182]. However, to confirm this argument, effects of potentially different microstructures (e.g., the thickness dependence of the mean linear distance between grain boundaries) have been examined in this chapter.

4.2 Semi-classical resistivity modeling

To gain further insight into the contributions of surface and grain boundary scattering, the thickness dependence of resistivity of ruthenium, iridium, rhodium, and copper was modeled using the semi-classical model developed

by Mayadas and Shatzkes [5]. Despite recent advances in ab initio modeling [6], [98], [107], [183], [184], the approach by Mayadas and Shatzkes remains the only tractable quantitative model for thin film resistivities in the studied thickness range up to 30 nm that contains both surface and grain boundary scattering. This is because the inputs required for the model are easily available in the literature (such as mean free path, bulk resistivity) or can be determined experimentally with high accuracy (mean linear intercept length). The Mayadas-Shatzkes model has already been discussed in detail in Chapter 2. The common quantum models [103], [185], [186] require a number of input parameters that are not always feasible to be determined experimentally (and include micro-scale roughness (that is of the order of the electron wavelength), relaxation times, correlation lengths, precise geometry of the wires etc.)

The model also neglects confinement effects that can be expected to further increase the resistivity for very thin films. For nanowires, ab initio calculations have shown an orientation dependent increase of the resistivity although the magnitude of the increase varied between studies [6], [98], [107], [183], [184]. As a consequence, the thickness dependence of confinement effects in nanowires (and the transition to bulk-like behavior) cannot be considered as fully understood for (copper) nanowires and even less so for (copper or platinum-group metals) thin films, where confinement effects can be expected to be weaker than for nanowires. **However, as discussed and shown in Chapter 2, confinement effects are expected to be negligible for the films studied in this work.** Also note that no different trends were observed for the thinnest films of 5 nm thickness and below, in the sense that fitting data subsets including thicker films only did not lead to significantly different fitting parameters. This is further proof that confinement effects, if present in the films used in this dissertation, are very weak and can be safely neglected. However, future work will be required to unambiguously identify the effect of the band structure and confinement on the thin film resistivity, especially for film thicknesses far below 5 nm.

The Mayadas-Shatzkes model for the resistivity of a thin film, along with its fitting parameters, has been discussed in Chapter 2. The full analytical model as shown in equation (2.13) will be used to model the thickness dependence of resistivity in this work. To reiterate, the model has two fitting parameters,

p and R, that describe the surface and the grain boundary scattering processes, respectively. The phenomenological surface specularity parameter p varies between 0 for diffuse and 1 for specular scattering of charge carriers at the surface or interface; R is the reflection coefficient ($0 < R < 1$) of a charge carrier at a grain boundary. In general, p can take different values at the top and bottom interface, e.g. when the surface and interface roughnesses are strongly different, as described by the model of Soffer [67]. However, given the observation that surface and buried interface roughnesses in the stacks considered here are low and very similar, we will assume that a single parameter p can describe both interfaces of the metal films.

4.2.1 Thickness dependence of the linear grain boundary distance

While surface scattering depends directly on the film thickness, grain boundary scattering depends on the average linear distance between grain boundaries, g, along the transport direction. Therefore, a quantitative model of the thin film resistivity as a function of film thickness requires the knowledge of the thickness dependence of g in polycrystalline films. Historically, it has often been assumed that g is identical or proportional to the film thickness and this assumption has often been used to model the thickness dependence of the resistivity. However, it has been pointed out that such simple relations are generally not valid [187].

In this work therefore, experimentally determined the average linear grain boundary distance using the intercept method [77] from plan-view transmission electron micrographs for nominally 5, 10, and 30 nm thick Ru/SiO_2 (as deposited and after annealing at 420 °C), TaN/Ru/TaN (annealed), Rh/SiO_2 (annealed), Ir/SiO_2 (annealed), and TaN/Cu/TaN (annealed) thin films.

Figure 4.5 shows both, sample TEM images as well as the deduced film thickness dependence of the mean linear grain boundary intercept length. While for TaN/Cu/TaN and annealed Ru/SiO_2 the mean linear intercept length was close to the film thickness, other stacks clearly showed a saturating

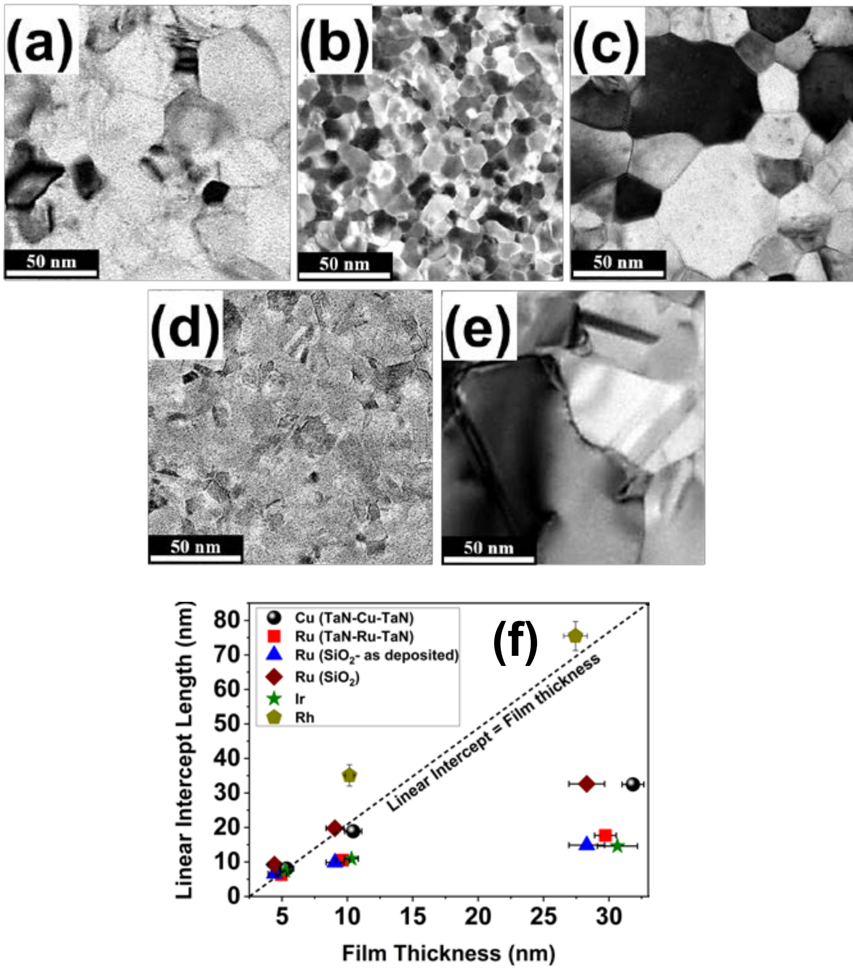

Figure 4.5 Plan-view TEM images of nominally 30 nm thick films of (a) TaN/Cu/TaN, (b) TaN/Ru/TaN, (c) Ru/SiO_2, (d) Ir/SiO_2, and (e) Rh/SiO_2. All films have been annealed at 420 °C for 20 min, except Ru (SiO_2 - as deposited). (f) Mean linear intercept length between grain boundaries deduced from the TEM images *vs.* film thickness. Due to a large number of measurements, the standard deviation in the linear intercept length is <1.5 nm in all cases (except for Rh where the standard deviation is 3.2 and 4.1 nm for 10 and 27 nm thickness respectively).

effect for ~30 nm thick films. Linear intercept lengths for in-between thicknesses were obtained by interpolation. Other more nonlinear interpolation schemes did not have any significant effects on the modeling results discussed later.

The linear grain boundary intercept length for Ru-SiO_2 increases upon annealing, which is to be expected as grain boundaries migrate to reduce the total energy of the system. The increase is more pronounced at higher film thicknesses and could be due to the deviation from equiaxial growth (discussed in Chapter 3) easing the grain boundary motion (as in case of out-of-plane grains spanning the film thickness, surface grooves form at the grain boundary-surface intersections due to the equilibration of the surface and boundary tensions and have been reported to 'pin' the migration of the grain boundaries [188]).

Comparison of the linear intercept length between metals is not advisable as it is not a material intrinsic property and depends on several factors including deposition conditions, thermal treatment, and stress [189].

4.2.2 Results and discussion

Figure 4.6 shows the experimental thickness dependence of the resistivity of various metals, together with the best fits using the Mayadas–Shatzkes model in equation (2.13). All films were annealed at 420 °C for 20 min except for an additional data set of as deposited Ru/SiO_2. To obtain the best fits, the experimentally determined thickness dependences of the linear distance between grain boundaries for the varied materials and stacks, as discussed in the previous subsection, were used. In addition, bulk electron mean free paths obtained by ab initio calculations in [73], were employed in combination with experimental bulk resistivities. As discussed earlier, quantum confinement effects are expected to be negligible for the thickness range studied in this dissertation.

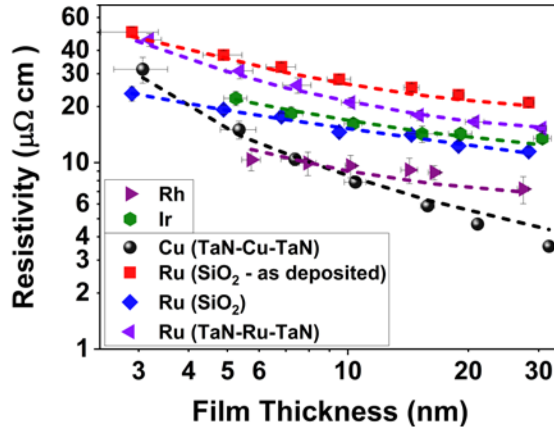

Figure 4.6 Best fits (dashed lines) using the Mayadas–Shatzkes model [5] to the experimental thickness dependence (symbols) of the resistivity of platinum-group metal and Cu films, as indicated. The resulting fit parameters are listed in **Table 4.1**. All stacks have been annealed at 420 °C except as deposited Ru/SiO_2.

Table 4.1. Modeling sputter deposited films: best fitting parameters, p (surface specularity parameter) and R (grain boundary reflection coefficient), along with λ (mean free path) and ρ (resistivity) used as input parameters in the Mayadas–Shatzkes model. The error in p and R values reflect the experimental in the determination of thickness, resistivity, and mean linear intercept length. The mean sum of squared errors, MSE, corresponding to the best fit is also given for each data set.

Material Stacks	p	R	λ (nm)	ρ (μΩcm)	MSE (μΩ^{2}cm^2)
Ru/SiO_2 (as deposited)	0.99 (+0.00/-0.19)	0.58 (+0.02/-0.02)	6.6	7.6	3.9
Ru/SiO_2 (annealed)	0.98 (+0.01/-0.25)	0.46 (+0.04/-0.05)	6.6	7.6	1.4
TaN/Ru/TaN (annealed)	0.01 (+0.08/-0.00)	0.47 (+0.04/-0.05)	6.6	7.6	1.8
Ir/SiO_2 (annealed)	0.99 (+0.00/-0.26)	0.47 (+0.02/-0.02)	8.1	5.2	0.6
Rh/SiO_2 (annealed)	0.99 (+0.00/-0.38)	0.62 (+0.06/-0.08)	7.5	4.8	0.9
TaN/Cu/TaN (annealed)	0.01 (+0.11/-0.00)	0.29 (+0.02/-0.02)	40.6	1.71	1.8

The p and R parameters were obtained with a direct search method. The resistivity was calculated using the Mayadas-Shatzkes model for all values of p and R, each between 0.01 and 0.99 in steps of 0.01 (thus, a total of 99*99=9801 iterations). Then, the mean sum of squared errors (MSE) was calculated with respect to the experimental values, and the data set with the lowest MSE was considered the best fit. Though this procedure was computationally demanding, it had the advantage to ensure that the global minimum of the error was found. Further, it also allowed to address correctly the mathematical correlations between p and R.

Due to the finite breadths of the minima, the confidence intervals for p and R need to be deduced from the MSE function. As opposed to linear regressions, there is no unanimous way to determine confidence intervals for nonlinear regressions. In this dissertation, it was decided to specify errors as the variation in p or R that corresponds to an increase of two times the MSE at the minimum.

Additional errors in p and R can stem from the propagation of errors in the original data – the sheet resistance, thickness, and the mean linear intercept length:

- The error in the linear intercept length is statistical as errors in the TEM length calibration is negligible. It was determined by analyzing several (>4-5) TEM images for a given layer as the standard error of the mean (each image, in turn, was analyzed along 8-10 different lines). The standard deviations were typically less than 1.5 nm due to large number of data points analyzed.

- The error in the sheet resistance is very small. Statistical errors (repeatability) of measurements are much smaller than 1% and the setup is well calibrated.

- The thickness was determined by both RBS as well as XRR. In both cases, the statistical error was negligibly small (<1%). However, there were considerable systematic errors on the determination of thickness, which was the most important source of error. It is to be noted that the errors in the thickness also affects the calculations of the resistivity from sheet resistance measurements. RBS measures

atomic density, which requires the assumption of a density to calculate a thickness. Bulk densities were assumed and were consistent with XRR measurements but the error on XRR densities can be estimated to be typically 5% due to correlations with other stack parameters. Moreover, the accurate modeling of XRR measurements often requires the inclusion of "surface contamination layer" and/or surface oxide layers. For noble metals, such as Ru or Ir (or in the presence of O-barrier capping layers such as TaN on Cu), the surface oxidation is small but in the case of thin films not completely negligible. Thus, systematic errors appear in XRR due to open questions whether such surface layers should be included in the total Ru thickness or not. Typically, XRR thicknesses were higher than RBS. To take this effect into account, the RBS was taken as the lower limit of the film thickness and XRR, including the thin surface contamination layers (typically ~1 nm or less), on Ru and Ir as the upper limit. The parameters p and R were fitted for both sets of data and the mean and the standard error are now reported for p and R in addition to the fitting error discussed above.

For ruthenium, the bulk resistivity has been reported to be anisotropic [101], [102]. Since all films studied here showed strong (002) texture, the bulk in-plane resistivity (perpendicular to the hexagonal axis) has been used. Only p and R were used as adjustable parameters. In general, the model described well the thickness dependence of the thin film resistivity for all materials and stacks over the entire thickness range. The resulting parameters are listed in Table 4.1.

Using the Mayadas–Shatzkes model, the best fit to the data for copper films (within a TaN/Cu/TaN stack) indicated that both surface ($p = 0.01$) and grain boundary scattering ($R = 0.29$) contribute to the thin film resistivity. The values of p and R fall well within the range of published values [13]–[15], [36], [42]–[44], [53], [55]. Moreover, they are in good agreement with a recent review [53] that concluded that the scattering at TaN/Cu interfaces is highly diffuse, in agreement with our results.

By contrast, the fitted grain boundary reflection coefficients for ruthenium, iridium, and rhodium were larger than for copper with $R = 0.46$ to 0.58 for

the different ruthenium stacks, $R = 0.47$ for Ir/SiO_2, and $R = 0.62$ for Rh/SiO_2. Grain boundary configurations, in particular, the average misorientation angle of contiguous grains, can have an influence on the grain boundary resistance. In literature, a simple model relating the R to the surface energy (and to the melting point) of polycrystalline films has been proposed[30] [78] where R is proportional to the melting point of the material. This is fully consistent with the observations that R was larger for the more refractory rhodium, ruthenium, and iridium than for copper. Moreover, the fitted values of $R \sim 0.5$ for ruthenium, $R = 0.47$ for iridium, and $R = 0.62$ for rhodium are in reasonable quantitative agreement with the predictions of this model of $R = 0.55$ for ruthenium, $R = 0.57$ for iridium, and $R = 0.50$ for rhodium [78]. The predicted value for copper is $R = 0.35$, and is also in reasonable agreement with the aforementioned model. It is to be noted that R deviates slightly from the experimental results and is possible because the determination of R can be influenced by several factors including, the nature of grain boundaries [98] and density of defects in the films. Also, the R for copper extracted by Mayadas-Shatzkes in their first demonstration of their formulation [5] was 0.24, in good agreement with the experimental results here.

Recently, R for twin boundaries in platinum-group metals (platinum, rhodium, iridium, and palladium) was calculated by *ab initio* methods [98] and found them to be higher than for copper, in qualitative agreement with the results here. It should however be noted that all such fitted R values describe "effective" grain boundary reflection coefficients since the grain structures of the films certainly contain many different grain boundary structures. For this reason, the quantitative understanding of grain boundary reflection coefficients both in copper and platinum-group metals will still require further work in the future[31].

---

[30]Discussed previously in section 2.1.2 (equation 2.17).

[31]Such undertaking would require extensive ab initio simulations that are beyond the scope of this dissertation. From a practical point of view, it would also require the characterization of all the individual grain boundaries present in films, which is not straightforward.

The fitted grain boundary coefficients of Ru/SiO_2 showed a significant reduction upon annealing ($R = 0.46$ *vs.* $R = 0.58$) beyond the uncertainty margins. This may be attributed to a reduction of the average misorientation of adjacent grains, as typically observed during recrystallization processes due to the preferred movement of high-angle grain boundaries [138], [140]. It has been calculated [190] and experimentally observed [60], [191], [192] for copper that the resistance of boundaries between randomly oriented grains is much larger than that of coherent or coincidence grain boundaries due to a high degree of disorder at the grain boundaries between randomly oriented grains. It is speculated that a similar behavior also applies to ruthenium grain boundaries, leading to a reduction of R upon annealing as observed in the experiments here. Similar arguments were made in [193] where a lower defect density at the grain boundaries was linked to a lower R.

Interestingly, both ruthenium and iridium on SiO_2 showed strong specular nature of the surface scattering. Hence, in those films, despite their small thicknesses, surface scattering did not appear to contribute strongly to the resistivity. It has been calculated that the surface scattering coefficient for a given interface should be a strong function of both the magnitude (RMS) as well as its lateral correlation length of the surface roughness [60], [69], [186], [191]. Although the Ru/SiO_2 and Ir/SiO_2 films were somewhat smoother than the TaN/Cu/TaN films (**Figure 4.3**), the difference is small, and the lateral correlations lengths are similar. Therefore, it appears unlikely that the difference between Ru/SiO_2 as well as Ir/SiO_2 and TaN/Cu/TaN was only due to differences in the physical surface properties. Thus, the electronic structure and the scattering potentials at the interface may contribute significantly [70].

Moreover, strongly diffuse scattering was observed at Ru/TaN interfaces (as in TaN/Ru/TaN stacks) with $p \sim 0$. This indicates that surface scattering depends less on the conducting metal (ruthenium *vs.* copper) than on the interface/*cladding* material of the thin film (SiO_2/air *vs.* TaN) (further discussion will follow). Note that surface roughnesses for TaN/Ru/TaN and Ru/SiO_2 were almost identical. Similar observations have been made for copper [70], [98], [194]. In particular, it has been observed that the surface scattering contribution to the thin film resistivity was lower in contact with oxides (SiO_2, Ta_2O_5) than with TaN [13], very similar to our observations.

The uncertainty in the determination of p is, in general, observed to be higher when compared to R. This is because the contribution of surface scattering to the film resistivity is very small and thus multiple p values can fit the thickness dependence of resistivity of various metals. This shall be elaborated in the next section.

Several models for the surface specularity parameter p have been reported in the literature [13], [60], [69], [70], [191], [195] that quantitatively link p to the surface roughness and the intrinsic properties of the Fermi surface of the conducting material. However, only very few studies have considered the effect of the *cladding* material [70], [195], which appears essential in view of the experimental results. Zahid et al. [70] have studied the resistivity of copper films surrounded by different metals using ab initio calculations and found that metals can both lower as well as increase p with respect to a free copper surface, depending on the difference of the density of states at the Fermi level of conducting metal (copper) and the *cladding* material at the interface. Although the density of states at the Ru/TaN interface has not yet been calculated, the bulk densities of states of ruthenium and TaN at the respective Fermi levels are rather similar [70]. Thus, additional work is needed in the future to clarify the contributions of the properties of the conductor and the *cladding* material and its interface on the surface scattering.

One of the biggest challenges in understanding the impact of the *cladding* layer on surface scattering is the lack of a general predictive theory that correlates the material properties of the interface/*cladding* to the boundary conditions of the center conductor. The general consensus, derived from ab initio transport and relaxation time calculations is that the origin of surface scattering is the geometrical roughness and an atomically smooth surface will always demonstrate $p = 1$ irrespective of the nature of the interface. Zahid et al. [70] argued, for copper, that the use of *cladding* metals which have the same density of states at the Fermi level as that of copper will electronically 'smoothen' the geometrical roughness. They showed, by ab initio methods, that the use of aluminum or palladium as capping/*cladding* on copper, whose density of states at the Fermi level matches that of copper, will result in specular scattering while the use of tantalum or ruthenium will result in diffused scattering due to the mismatch of the density of states at the fermi level. Experimentally, it was shown by Rossnagel et al. [13] that a thin

tantalum layer on copper led to fully diffused surface scattering. However, when the tantalum layer was allowed to oxidize in air, the surface scattering turned specular. It shows the extremely sensitive nature of surface scattering. Chawla et al. [71] demonstrated similar results for copper with a thin tantalum layer on top. They claim that the atomically smooth interface results in a flat periodic potential that causes the conduction electrons to specularly scatter at the interface. However, the addition of a tantalum layer on copper causes a perturbation to the smooth interface potential and results in displaced scattering centers from the original interface and cause completely diffuse surface scattering. It is difficult to determine the scattering potentials of such realistic surfaces and such questions cannot be conclusively answered. Still, qualitative comparison between our results and the literature can be done and there are many similarities between our results on copper, iridium, ruthenium, and rhodium and previously published work essentially exclusively on copper.

The loss of momentum of diffusively scattered electrons from the interface is also not due to spin disorientation. Not only there is no clear published evidence for that, but additionally, spin disorientation is proportional to the fourth power of the atomic number, meaning, if spin disorientation and momentum loss were related, then a cladding with a higher mass number should also lead to larger surface scattering. This is in direct contrast with Zahid et al. [70] where they report specular scattering for copper with palladium capping (Z=46) but diffused scattering with ruthenium capping (Z=44).

It must be noted that all the above studies are highly case-specific and thus it is difficult to draw a generic conclusion that is applicable for an arbitrary interface. Additionally, the results obtained in this work that specular scattering for the case of Ru/SiO_2, Ir/SiO_2, and Rh-SiO_2 even though they interface is not atomically flat disputes the theory that only geometrical roughness is the origin of surface scattering. This is further corroborated by the work of Chawla et al. [71] and Rossnagel et al. [13] as discussed earlier.

Further evidence that surface scattering is negligible for Ru-SiO_2 stack can be found in temperature-dependent resistivity measurements. It has been shown that if surface scattering was dominant and to have a significant contribution

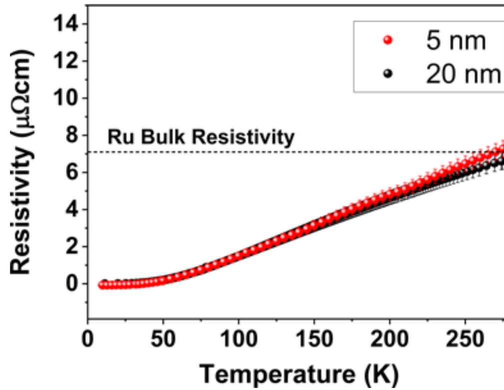

Figure 4.7 Temperature-dependent contribution to resistivity vs temperature for 5 and 20 nm of as-deposited Ru films on SiO_2. The temperature-dependent part of resistivity is almost independent of the films thickness, indicates grain boundary scattering is the dominant scattering mechanism contributing to resistivity. Additionally, the temperature-dependent contribution to resistivity being equal to the bulk resistivity indicates grain boundary scattering is independent of phonon scattering (The uncertainty in temperature scale is less 0.5 K).

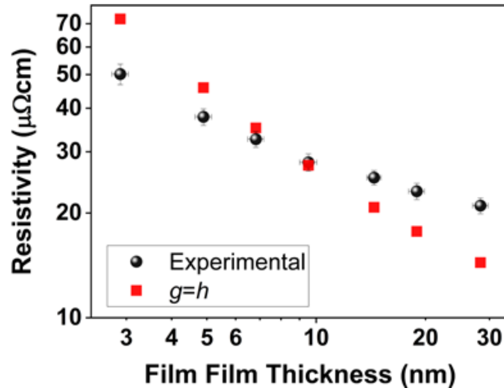

Figure 4.8 Simulated thickness dependence of resistivity of PVD Ru on SiO_2 under the assumption that the linear grain boundary intercept length is equal to the film thickness ($g = h$), compared with the experimental values

to resistivity, the slope of the temperature-dependent part of the resistivity (i.e. residual resistivity at 4.2 K subtracted from the total resistivity) as a function of temperature would vastly differ for different film thicknesses [83], [196]. But in case of the dominance of grain boundary scattering, the slope would not vary with the film thickness, which is what is found in this work for the as-deposited ruthenium films of 5 and 20 nm of thickness on SiO_2, within errors (**Figure 4.7**). This experiment proves decisively that grain boundary scattering is indeed the dominant scattering mechanism in these thin films. The temperature-dependent part of the resistivity is almost equal to the bulk resistivity of ruthenium and indicates that grain boundary scattering is independent of phonon scattering[32].

Finally, a hypothetical case is simulated for the thickness dependence of resistivity of PVD ruthenium on SiO_2 (as deposited) with the most common assumptions made in the literature i.e., grain size being equal to the film thickness, $g = h$ (**Figure 4.8**). A much stronger dependence of resistivity on thickness is observed resulting in a significant deviation of the simulated values from the experimental curve. The mean sum of squared errors (MSE) quantifying the observed deviation is 94 $\mu\Omega^2cm^2$, about 24x higher when compared to the case when linear grain boundary intercept lengths are measured experimentally. This underlines the importance of the microstructural characterization in this work.

4.2.3 Comparison: ALD vs PVD Ru films

Sputter deposited films typically have the advantage of being high in purity, comparatively easier to deposit, and reach film closure at a smaller thickness when compared to chemical-based processes. However, ALD processing in modern semiconductor manufacturing is virtually indispensable. Aggressive miniaturization of the devices has resulted in high aspect ratio structures in variety of steps that need conformal film coatings that not only are electrically

[32]Total film resistivity (ρ_{tf}) can be expressed as a sum of temperature-dependent (ρ_t) and temperature-independent components (ρ_i). However, from Figure 4.7, $\rho_t \approx \rho_0$, thus $\rho_i \approx \rho_{GB}$, which implies that the grain boundary scattering is independent of phonon scattering.

continuous but morphologically consistent with low surface roughness, including gate dielectric, diffusion barriers, adhesion liners, and interconnects. There are several advantages to ALD which include, a higher degree of control over thickness, and self-saturating behavior that leads to excellent step coverage and conformal deposition, even at the nanometer scale [197].

Several ruthenium ALD processes have been reported in the past [197]–[202]. Though these processes have shown excellent step coverage, there has always been issues with delays in nucleation and growth inhibitions especially on oxide substrates, and that has resulted in undesirable island-like growth characteristics. New precursor designs have enabled shorter nucleation periods thus promoting two-dimensional growth [203]–[205], among which the EBECH ruthenium precursor has been reported to yield thin films with low resistivity values even on vastly different starting surfaces such as SiO_2 and TiN [205]. The goal of this section is to evaluate the scattering mechanisms in ALD ruthenium films and compare to the observations made for the ruthenium films deposited by PVD.

Ruthenium films were deposited by the EBECH Ru/O_2 ALD process at 325°C [205] on thick (~90 nm) SiO_2 and on varying thickness of TiN (0.3 nm, 1 nm, and 5 nm). Ruthenium films on SiO_2 demonstrated strong preferential growth towards the (002) texture (similar to sputter deposited ruthenium on SiO_2) with a very weak (101) component, while diffraction patterns on TiN were consistent with a random polycrystal (**Figure 4.9 (g)**). The detailed explanation for the observed differences in texture on SiO_2 and on TiN can be found elsewhere [205] where it has been reported that the ruthenium growth process on TiN using the EBECH Ru precursor is mediated by the $Ti(O,N)_x$ segregation which lowers the surface energy and suppresses the commonly observed (002) texture in ruthenium films.

The linear intercept lengths of the ALD ruthenium films on SiO_2 and on 0.3 nm TiN (as deduced from the TEM images from **Figure 4.9 (a)-(c)** and **(d)-(f)**, respectively) is shown and compared with PVD ruthenium films in **Figure 4.9 (h)**. The linear intercepts of ALD films on SiO_2 are much larger than PVD films on SiO_2, possibly due to the fact that ALD films used in this

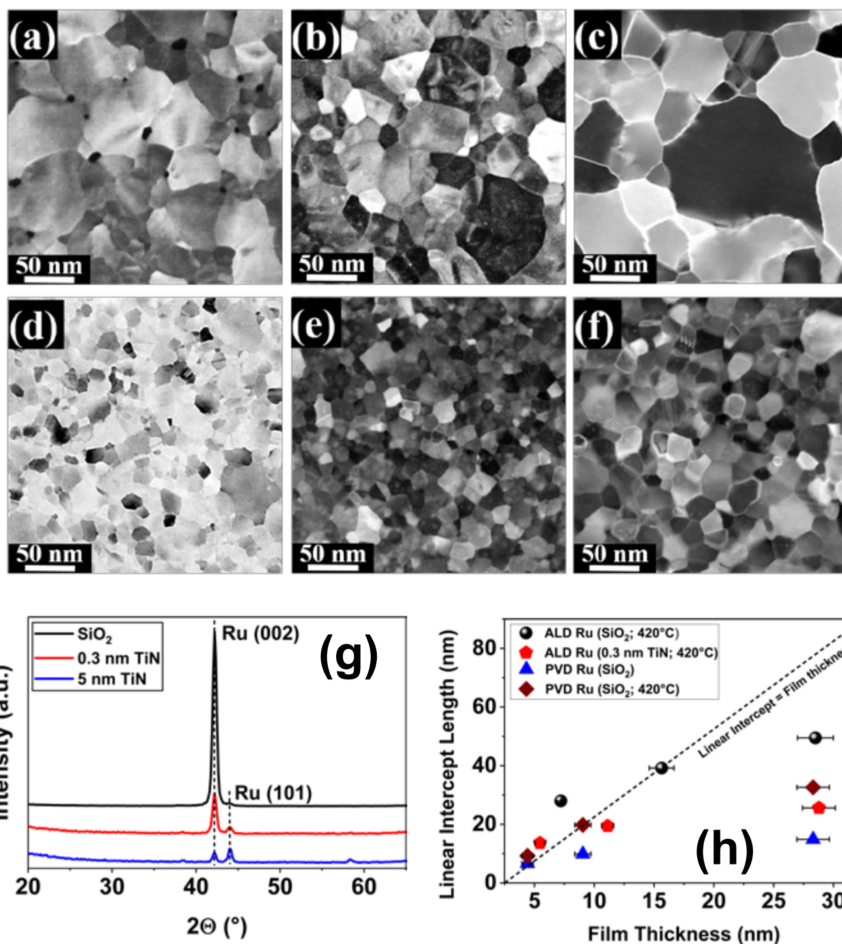

Figure 4.9 In-plane TEM images of nominally 7, 13, and 30 nm ALD Ru films on SiO_2 (a,b, and c respectively) and on 0.3 nm TiN (d, e, f respectively) after an ex-situ anneal at 420°C for 20 minutes in a reducing ambient (He+H_2). (g) Comparison of the x-ray diffraction spectra of ALD ruthenium films on various substrates (SiO_2, 0.3 nm TiN, and 5 nm TiN). On SiO_2, ruthenium films texture towards the (002) plane, similar to PVD ruthenium films on SiO_2. However, on TiN, ruthenium films are randomly polycrystalline irrespective of the TiN layer thickness. (h) Mean linear intercept length between grain boundaries deduced from the TEM images as a function of film thickness for ALD Ru films. Comparison with PVD Ru films shown. The dashed line represents the case where the linear intercept length is equal to the film thickness (Due to a large number of measurements, the maximum standard deviation in the linear intercept length is less than 1.9 nm in all cases).

work were grown at 325°C which allowed for larger grains to be obtained as compared to PVD films that were deposited at room temperature.

The linear intercepts of ALD ruthenium films on SiO_2 are much larger (by about 1.5 - 2x) than on 0.3 nm TiN, possibly due to the *solute drag* effect and the strong differences observed in the grain size from the TEM images (**Figure 4.9 (a)-(c)** *vs.* **(d)-(f)**). In literature, impurities are known to increase the recrystallization temperatures (a case for copper has already been discussed in Chapter 3). It has been shown that the impurities often segregate at the grain boundaries [206]–[208] thus retarding their motion and limiting their growth. The phenomenon is known as *solute drag*.

When using the EBECH precursor to deposit Ru on TiN by ALD, it has been reported in literature [205] that Ti segregates and incorporates at low levels during deposition. In that study, medium-energy ion scattering (MEIS) measurements were used to evidence the surface Ti layer. In the thesis, it was observed that the recrystallization temperature of EBECH Ru films deposited on TiN were much higher than on SiO_2 (Appendix B). Secondary ion mass spectroscopy (SIMS) measurements show the presence of Ti inside the Ru film and also at the Ru/air interface (**Figure 4.10**). The concentration of titanium inside the films increased with the thickness of the TiN layer, increasing from $<10^{17}$ atoms/cm^3 for a 0.3 nm TiN substrate to $\sim 5 \times 10^{18}$ atoms/cm^3 for 5 nm TiN. The mechanism for Ti incorporation has been discussed elsewhere [205]. The surface Ti is qualitatively consistent with the MEIS measurements in [205]. However, a quantitative comparison between SIMS and MEIS is difficult due to the SIMS transient effects and the impact of surface oxidation on Ti ionization yield. The same effect also makes the interpretation of the signal at the Ru/SiO_2 interface very difficult. The anomalous signal is most likely due to mass interference from the Si-SiO_2 interface. One possibility includes $SiOH_4$ ($\equiv {}^{48}Ti$). Oxides are common interferences since oxygen-metal/semiconductor bonds are particularly stable. Moreover, the presence of O near the interface will strongly increase the Ti ionization yield and the signal will represent the O concentration as much as the Ti concentration. Therefore, the perceived accumulation near the interface may at least be partially an artifact. However, SIMS clearly indicates the presence of Ti inside the Ru film. The error in depth scale is a

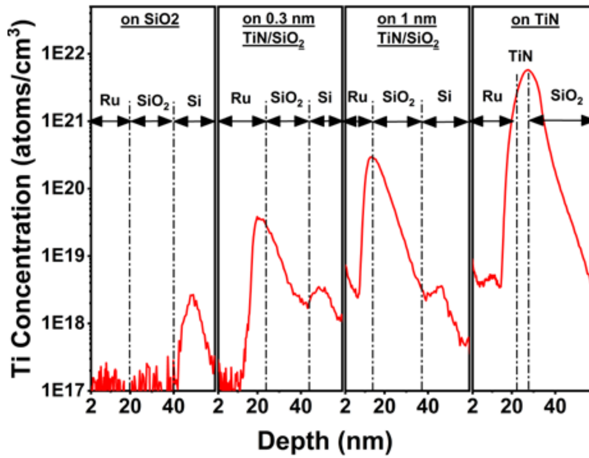

Figure 4.10 Ti SIMS depth profile[33] of ALD Ru on SiO_2 (control sample), 0.3 nm TiN, 1 nm TiN, and 5 nm TiN. Ti incorporation in Ru films increases with thicker TiN underlayer, from $<10^{17}$ to 5×10^{18} atoms/cm^3. The higher amount of Ti in Ru films for thicker TiN underlayer is correlated to higher recrystallization temperature observed for Ru films on TiN (Appendix B). The error in depth scale of Ti concentration is a maximum of ±4 nm due to the assumption that the average sputter rate during the SIMS measurements is constant.

maximum of ±4 nm due to the assumption that the average sputter rate is constant. Even with the error bars, the qualitative conclusion is not affected.

The data indicate that there exists a correlation between the amount of Ti inside the Ru films and the recrystallization temperature. Higher Ti concentrations led to higher recrystallization temperatures. The hypothesis is the solute drag effect, in which the solute/impurity atoms segregate at the grain boundaries and increasing the activation energy for grain boundary migration, causing a "pinning" effect. This effect is well established in the

[33]Transient effects during SIMS depth profiling have been reported to affect the estimation of the concentration of the species under study, but is typically limited to the surface only [209]. Thus, the Ti concentration data at the top 2 nm of the stack has been discarded. This is not expected to significantly affect the conclusion as we are more interested in quantifying the Ti concentration *within* the film.

literature [207], [208], [210]. To test for this hypothesis, Atom Probe Tomography (APT) measurements were attempted but have so far failed because of the several complexities involved in the sample preparation including Ru films. APT could have provided an insight into the spatial distribution of Ti inside the Ru film. Thus, the current data can only prove a correlation between the Ti concentration and the recrystallization temperature of Ru.

Thus, it is likely that solute drag causes the ALD ruthenium films grown on TiN to have a smaller mean linear intercept length than on SiO_2. (**Figure 4.9 (h)**). Normally, it would be expected that a difference of such magnitude in the mean liner intercept lengths would result in significant differences in resistivity, but surprisingly it was observed that resistivity of ruthenium films on SiO_2 were only marginally lower than on 0.3 nm TiN (**Figure 4.11**). This could be ascribed to the following reasons: firstly, the resistivity in the ruthenium hcp crystal lattice is anisotropic where the resistivity in the direction parallel to the c-axis has ~27% lower resistivity than perpendicular to it [101], [102]. In case of ALD ruthenium grown on SiO_2, the out-of-plane texture is (002) and thus the charge carriers are flowing in the directions perpendicular to c-axis thus through the higher resistivity path.

Secondly, it has also been reported (for copper nanowires) that the presence of impurities at the grain boundaries reduces resistivity by lowering the number of empty states around the Fermi energy in the boundary plane region of the grain boundary [211]. The same effect could contribute to lower the resistivity of ruthenium thin films grown on TiN with Ti segregation at the grain boundaries. More work is needed in the future to ascertain this point for the specific case discussed here.

The recrystallization temperature of the ALD ruthenium films on SiO_2 was found to be around 450°C, similar to PVD ruthenium films on SiO_2. As the grain size for the above two cases are vastly different (**Figure 4.9 (h)**), the changes in the density of the grain boundaries observed here are not sufficient to effect a change in the recrystallization temperature. Thus, the increase in the recrystallization temperature for ALD ruthenium films on TiN when compared to SiO_2 is not likely to be due to different density of grain boundaries.

The best fits of the experimental thickness dependence of the resistivity of ALD ruthenium films on SiO_2 and on 0.3 nm TiN using the Mayadas–Shatzkes model in equation (2.13) is shown in **Figure 4.11**. As ALD ruthenium films on TiN were observed to be random polycrystal (see **Figure 4.9 (g)**), bulk resistivity was taken as 7.1 μΩcm [101], [102] as opposed to 7.6 μΩcm for (001) textured films. Again, only p and R were used as adjustable parameters. The resulting parameters are listed in Table 4.2.

For ALD ruthenium films on SiO_2, the best fit to the data indicated the surface scattering to be strongly specular, consistent with what has been observed for PVD ruthenium films on SiO_2. On 0.3 nm TiN however, the surface scattering assumed a diffusive character. It is to be mentioned here that when growing ALD Ru on 0.3 nm TiN-SiO_2, it was reported that not only Ti diffuses inside the ruthenium films but also goes to the top surface of ruthenium [205]. Thus, the stack effectively takes the form Ti/ALD Ru/TiN. This is analogous to TaN/PVD Ru/TaN discussed in the previous section and the observation of the diffusive surface scattering is consistent. Thus, a very thin *cladding* is sufficient to fully transform the surface scattering behavior, which strongly suggests that the surface scattering behavior is very sensitive to the interface characteristics. These observations are further evidence that the surface scattering behavior is not material intrinsic and strongly depends upon the nature of the interface.

The grain boundary reflection coefficient for ALD ruthenium films on SiO_2 were similar to PVD ruthenium films on SiO_2 after annealing within the error bars. This points that the deposition process did not significantly affect the grain boundary scattering behavior, within the uncertainty margins. The small decrease could be possibly due to the higher processing temperature (325°C) during ALD growth allowing for the passivation of more defects at the grain boundaries. On 0.3 nm TiN, R was again similar to that of ALD ruthenium on SiO_2 and PVD Ru on SiO_2 within the error margins.

Overall, the scattering behavior of the ALD ruthenium films, both surface and the grain boundary, did not significantly deviate from the films deposited by PVD and remained qualitatively similar. **The results here demonstrate the repeatability of the *p* and the *R* values on several different stacks accounting for a large spread in the linear grain boundary intercept length and resistivity values.**

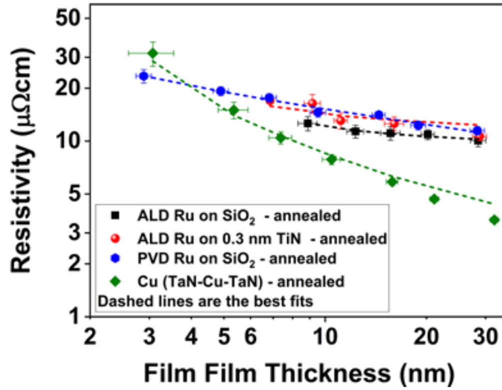

Figure 4.11 Thickness dependence of resistivity of ALD Ru films on SiO_2 and on 0.3 nm TiN (solid symbols). Best fits (dashed lines) using the Mayadas–Shatzkes model [5]. The resulting fit parameters are listed in Table 4.2. (A comparison with PVD Ru films on SiO_2 and Cu is also shown). All films annealed at 420°C.

Table 4.2. Modeling ALD Ru films: best fitting parameters, *p* and *R*, along with mean free path λ and resistivity ρ used as input parameters in the Mayadas–Shatzkes model [5].

Material Stacks	p	R	λ (nm)	ρ (μΩcm)	MSE ($\mu\Omega^2cm^2$)
ALD Ru/SiO_2 (annealed)	0.98 (+0.01/-0.31)	0.44 (+0.07/-0.06)	6.6	7.6	0.1
PVD Ru/SiO_2 (annealed)	0.98 (+0.01/-0.25)	0.46 (+0.04/-0.05)	6.6	7.6	1.4
ALD Ru/0.3 nm TiN (annealed)	0.01 (+0.16/-0.00)	0.42 (+0.05/-0.03)	7.06	7.1	1.7
TaN/PVD Cu/TaN (annealed)	0.01 (+0.11/-0.00)	0.29 (+0.02/-0.02)	40.6	1.71	1.8

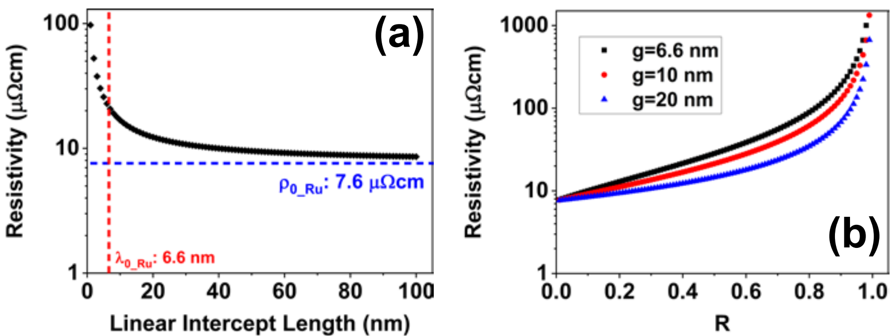

Figure 4.12 (a) Linear grain boundary intercept length, *g*, *vs.* Resistivity. The impact is pronounced with $g \sim \lambda_0$. Once g >4-5x λ_0, gains in resistivity are limited. (b) *R* vs. Resistivity, for various intercept lengths. Impact of *R* would be stronger for films that have smaller grains

An intriguing observation is the fact that even though the linear grain boundary intercept length for ALD ruthenium on SiO_2 reduced by ~1.6x (38%) between the thickest (28 nm) and the thinnest (8 nm) measured film, the increase in the corresponding thin film resistivity was only ~20%, increasing from 10 μΩcm for 28 nm to 12 μΩcm for 8 nm). This can be understood by studying the direct relation between thin film resistivity (equation (2.13)) and the linear grain boundary intercept length.

Since specular scattering is observed for ALD Ru films on SiO_2, the resistivity of thin films is only a function of α' (equation (2.11)), within the Mayadas-Shatzkes theory. α' in turn depends upon the linear intercept length and *R*. So, for a given film (and thus fixed *R*), α' depends solely on the linear intercept length. In **Figure 4.12 (a)**, simulations within the Mayadas-Shatzkes model show that the increase in resistivity starts to be drastic when the linear intercept lengths are reduced to the order of the mean free path. This means that there are limited gains in resistivity by increasing the grain size (and thus linear intercept length) beyond a certain point (>4-5 times of the mean free path). This explains why the increase in resistivity was rather limited going from a 28 nm ALD Ru film to an 8 nm film on SiO_2. **This is further proof that the contribution of surface scattering to resistivity is negligible**. Additionally, a weaker thickness dependence of resistivity for a metal film can be achieved by increasing the grain size sufficiently beyond the mean free path.

Similarly, the impact of *R* on resistivity was simulated and it was found that the impact would be stronger for films that have smaller grains (**Figure 4.12 (b)**). The increase is more pronounced at higher values of *R*. Since *R* has been argued to have a dependence on the melting point of a metal, grain boundary scattering would be more detrimental to the resistivity of metals with high melting point.

The simulations further explain that the reduction in resistivity for PVD ruthenium films on SiO_2 upon annealing (**Figure 4.6**) is significant (>50%) because not only the *R* reduced from 0.58 to 0.46, but also the fact that the linear intercept length is of the order of the mean free path and an increase after annealing translated into substantial improvement in resistivity.

Physically, the above simulations indicate that even though grain boundaries act as scattering planes for the charge carriers, grains that are sufficiently large (by a factor of 4-5 of the mean free path) would not significantly impact the relaxation times between the scattering events.

4.2.4 Relative contribution of scattering mechanisms

The derivation of the Mayadas-Shatzkes model [5] does not require that surface scattering and grain boundary scattering are independent of each other. Thus, the thin film resistivity cannot generally be written as the sum of the bulk resistivity, surface scattering contribution, and a grain boundary scattering contribution, as discussed earlier. This issue has also been discussed in detail in the original publication by Mayadas and Shatzkes [5] and rather convincing physical reasons (the "renormalization" of the mean free path by grain boundary scattering) have been mentioned why such a separation/independence should not be expected. As a consequence, this limits the possibilities to fully quantify the relative contributions of surface and grain boundary scattering to trivial cases where either the surface or the grain boundary scattering is zero.

In the literature, approximations of the Mayadas-Shatzkes equation under the assumption that grain boundary and surface scattering are separable have been derived and these approximations have been used often in the literature to fit the experimental data and derive a quantitative figure for the contributions from surface and grain boundary scattering to resistivity [37], [212]. However, as discussed by Mayadas and Shatzkes in [5], such approximations are not expected to be necessarily valid. For example, [44] have used both the full Mayadas-Shatzkes model as well as an approximation assuming the validity of Matthiessen's rule to fit the same data for copper thin films. Although the quality (in terms of reduced coefficient of determination) of the fits was comparable, they found rather different p and R values for the two models. Thus, the approximation assuming the validity of Matthiessen's rule cannot be considered as good.

In the Mayadas-Shatzkes formulation in equation (2.13), while the first term in equation (2.13), $1/\rho_{GB} \equiv \sigma_{GB}$, describes grain boundary scattering independent of surface scattering, the second term $1/\rho_{SS,GB} \equiv \sigma_{SS,GB}$ describes combined effects of surface and grain boundary scattering[34]. Nonetheless, the ratio of the two terms can be evaluated and used to shed some light on the relative importance of grain boundary and surface scattering within the Mayadas–Shatzkes model. **Figure 4.13** shows the ratio of $\sigma_{SS,GB}$ and σ_{GB} as a function of the surface scattering parameter *p* for TaN/Cu/TaN, Ru/SiO_2, and TaN/Ru/TaN, as well as Ir/SiO_2 and film thicknesses of 5 nm (**Figure 4.13 (a)**) and 20 nm (**Figure 4.13 (b)**). Experimental mean linear intercept lengths and *R* corresponding to best fits were used (Note that the uncertainty margins of *R* did not significantly impact the results). It should also be noted that in equation (2.13), a ratio of $\sigma_{SS,GB}/\sigma_{GB} = 0.5$ corresponds to equal contributions of the two terms. If $\sigma_{GB} \gg \sigma_{SS,GB}$ for all values of *p*, the second term can be neglected and the thin film resistivity in the Mayadas–Shatzkes model is dominated by grain boundary scattering. However, due to the violation of Matthiessen's rule, the opposite conclusion, namely the dominance of surface scattering for $\sigma_{GB} \approx \sigma_{SS,GB}$, is not necessarily valid.

The data indicate a general prevalence of the grain boundary scattering over surface scattering within the Mayadas–Shatzkes model for all stacks even for the most diffusive case of $p = 0$ since generally $\sigma_{SS,GB}/\sigma_{GB} \ll 0.5$. Only for TaN/Cu/TaN (in particular, for 5 nm film thickness), $\sigma_{SS,GB}$ contributed strongly to the overall conductivity. By contrast, the contributions were weak for the platinum-group metal containing stacks—even for fully diffusive surface scattering, as observed for TaN/Ru/TaN.

The different magnitudes of $1/\rho_{GB} \equiv \sigma_{GB}$ and $1/\rho_{SS,GB} \equiv \sigma_{ss,GB}$ have strong repercussions on the accuracy of the extracted *p* and *R* values. In general, due to the small contribution of $\sigma_{ss,GB}$, the uncertainty in *p* was larger than *R* (**Table 4.1**). This shows that the surface specularity parameter of the platinum-group metals can therefore only approximately be determined by modeling of the thickness dependence of the resistivity within the Mayadas–Shatzkes model, at least for the film thicknesses and grain sizes considered

[34]The second term on the RHS of equation (2.13) contains both *p* and *R*.

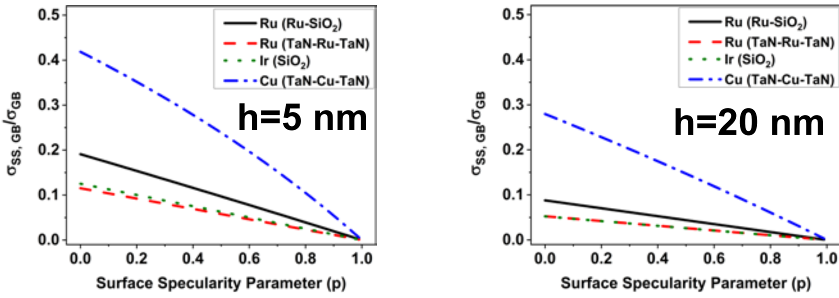

Figure 4.13 $\sigma_{SS,GB}/\sigma_{GB}$ as a function of the surface scattering parameter p for (annealed) stacks as indicated for film thicknesses of (a) 5 nm, and (b) 20 nm respectively. Experimental mean linear intercept lengths and R corresponding to the best fits were used.

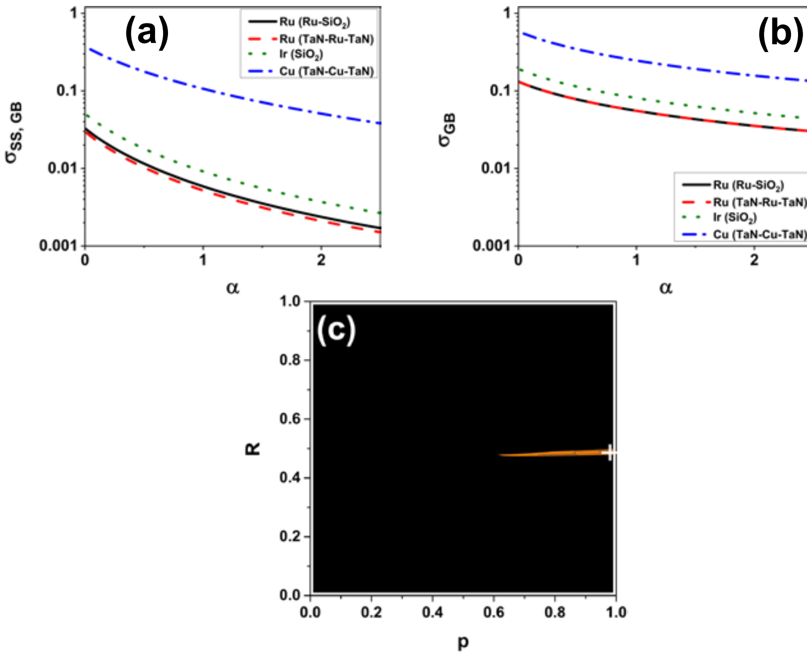

Figure 4.14 Deviations from Matthiessen's rule: (a) $\sigma_{SS,GB}$ and (b) σ_{GB} as a function of the dimensionless grain boundary scattering parameter $\alpha' = (\lambda_0/l) \times 2R(1-R)^{-1}$. Here, the thickness was set to 10 nm and fully diffuse surface scattering with $p = 0$ was assumed to make the curves more comparable. (c) Mean sum of squared errors (MSE) of fits to the experimental data (Figure 4.6) vs. p and R fitting parameters for Ir/SiO_2 after post-deposition annealing at 420 °C. The full color scales correspond to the range between 1× and 2× the minimum MSE. The white cross represents the minimum MSE.

here. However, the discussion above suggests that the grain boundary scattering dominates the ruthenium and iridium thin film resistivities, even more so than for copper, due to the much smaller mean free path and that this holds independent of the exact value of p. This also indicates that the absolute value of p should not necessarily be taken as a measure whether surface scattering contributes significantly or not. To reiterate, p describes only the *nature* of the surface scattering. It does not indicate the relative contribution of surface scattering.

By contrast, the contribution of $\sigma_{SS,GB}$ was much larger for TaN/Cu/TaN (**Figures 4.13 (a)** and **(b)**). This can be linked to the long mean free path of 40.6 nm and indicates that surface scattering cannot be simply neglected for thin copper films. Although both σ_{GB} and $\sigma_{SS,GB}$ are reduced with increasing mean free path (via the dimensionless parameters α' and k in equation (2.13)), $\sigma_{SS,GB}$ appears more sensitive than σ_{GB}, leading to an increasing prevalence of σ_{GB} for large α'. In addition, the grain boundary reflection coefficient of copper, $R = 0.29$ was found to be much smaller than for platinum-group metals ($R \sim 0.5$), which also leads to a weaker relative contribution of σ_{GB} for copper with respect to the platinum-group metals

Among the platinum-group metals, $\sigma_{SS,GB}/\sigma_{GB}$ of Ru/SiO_2 showed a much stronger dependence on p (**Figures 4.13 (a)** and **(b)**) than TaN/Ru/TaN or Ir/SiO_2. This can be linked to deviations from Matthiessen's rule, as shown in **Figure 4.14**. As pointed out by Mayadas and Shatzkes [5], the (effective) mean free path that determines surface scattering in a polycrystal (i.e., in the presence of grain boundary scattering) is reduced over the bulk value (renormalization) by $\lambda_{GB}=(\rho_0/\rho_{GB}).\lambda_0$. This leads to a dependence of surface scattering on α'. The effect is illustrated in **Figure 4.14 (a)** for $h = 10$ nm, which shows $\sigma_{SS,GB}$ as a function of α. To make the curves more comparable, $p = 0$ was assumed in all cases. For comparison, the dependence of σ_{GB} on α is also shown in **Figure 4.14 (b)**. The data show that an increase of α' (i.e., stronger grain boundary scattering) leads to a decrease in $\sigma_{SS,GB}$ that is generally faster than for σ_{GB}. At $h = 10$ nm, due to the combination of large grains and short mean free path, α' = 0.5 for Ru/SiO_2, much smaller than for TaN/Ru/TaN (α' = 1.4 ± 0.1), and Ir/SiO_2 (α' = 1.6 ± 0.1), which leads to a relatively larger $\sigma_{SS,GB}$ of Ru/SiO_2 for a given value of p. In practice

however, the scattering at Ru/SiO_2 and Ru/air interfaces was found to be nearly specular and the contribution of $\sigma_{SS,GB}$ to the thin film resistivity was also negligible for Ru/SiO_2.

The above reasoning indicates that, for smaller grains, not only the grain boundary scattering contribution to resistivity (ρ_{GB}) would increase (smaller grains lead to larger α') but also the surface scattering in the presence of grain boundary scattering ($\rho_{SS,GB}$) would grow (smaller grains would lead to renormalization of the mean free path which, in turn, would increase $\rho_{SS,GB}$). Thus, all things being equal, smaller grains would lead to a comparatively stronger correlation between the grain boundary scattering and the surface scattering.

It should be noted that the renormalization of surface scattering by grain boundary scattering leads always to weaker surface scattering when grain boundary scattering is increased. This needs to be considered in the conclusions. For example, surface scattering contributions of copper are typically stronger than for ruthenium because of the longer mean free path but also because of the lower *R*. Also, since the uncertainty in *R* is small in all cases, the quantitative impact on the above calculations are negligible and does not affect the overall conclusions

4.2.5 Influence of the mean free path

Finally, within the Mayadas-Shatzkes model, the relative impact of the different material parameters (λ_0, p, R, l) on the slope of the thickness dependence of the thin film resistivity is evaluated. It has been previously proposed that metals with a shorter mean free path may show a much weaker thickness dependence of their thin film resistivity [45], [46], [182]. However, this effect may potentially be complemented or dominated by other factors such as the material (stack) dependence of surface and grain boundary scattering coefficients as well as the thickness dependence of the mean linear grain boundary intercept length, which will in generally depend both on the material and the applied thermal budget.

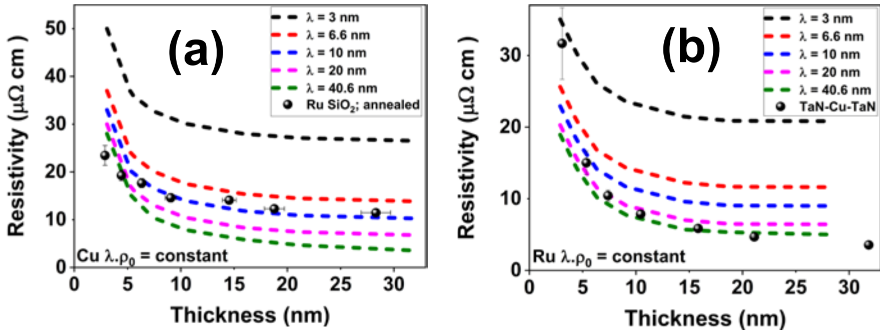

Figure 4.15 Calculated thickness dependence of the resistivity as a function of the mean free path λ_0 with $\lambda_0 \times \rho_0$ constant using (a) Cu parameters (i.e., $\lambda_0 \times \rho_0$, p, and R) and linear distances between grain boundaries as well as (b) Ru parameters and linear distances between grain boundaries. For λ_0 equal to the value for Ru (6.6 nm), the simulated curve using Cu parameters in (a) is close to the Ru/SiO_2 experimental resistivities; analogously, the λ_0 of Cu (40.6 nm) in combination with Ru parameters in (b) leads to a thickness dependence of the resistivity close to that of Cu. This indicates that the weaker film thickness dependence of the resistivity of platinum-group metals as compared to Cu can be attributed mainly to their shorter mean free paths.

To gain further insight into the importance of the electron mean free path, we have calculated the expected thickness dependence of the resistivity of copper or ruthenium as a function of the mean free path, keeping λ_0 x ρ_0 constant as it is only a function of the Fermi surface morphology. The result, using the experimentally deduced parameters (p, R, and mean linear grain boundary intercept length) for copper, is shown in **Figure 4.15 (a)**. The data indicate that the overall slope of the resistivity *vs.* thickness curves shows a strong dependence on the mean free path. Reducing the mean free path to that of ruthenium (6.6 nm, [73]) while keeping λ_0 x ρ_0 constant (6.9 x 10^{-16} m^2) leads to both a slope and absolute resistivities that are close to what was experimentally observed for annealed Ru/SiO_2 (**Figure 4.15 (a)**).

Conversely, as shown in **Figure 4.15 (b)**, using the parameters obtained for annealed Ru/SiO_2 (p, R, and average linear intercept between grain boundaries) and increasing the mean free path to that of copper (40.6 nm, see Table 4.1) while again keeping λ_0 x ρ_0 constant (5.0 x 10^{-16} m^2) leads to a slope almost identical to that experimentally observed for TaN/Cu/TaN.

The residual differences stem from the material dependence of λ_0 x ρ_0, *R*, and *p* (see reference [73]), as well as from the different thickness dependence of the mean linear grain boundary intercept length, and are rather small. The larger deviations for the 3 nm thick films in both graphs can be ascribed to the much stronger contribution of surface scattering to the copper resistivity, which becomes significant only for such small thicknesses. As a whole, however, this confirms that the shorter mean free path is the root cause for the different thickness dependence of the resistivity of copper and the platinum-group metals.

4.3 Chapter summary

In this chapter, the thickness dependence of the resistivity of thin platinum-group metal films in the range between 3 and 30 nm was examined. All studied platinum-group metals (ruthenium, rhodium, palladium, iridium, platinum) showed a much weaker thickness dependence than copper, the reference material. As a consequence, platinum-group metal thin films show comparable or even lower resistivities than copper for film thicknesses of about 7 nm and below.

The thickness dependence of the resistivity of TaN/Cu/TaN, Ru/SiO_2, TaN/Ru/TaN, Ir/SiO_2, and Rh/SiO_2 was modeled using the Mayadas–Shatzkes model and experimentally determined mean linear grain boundary intercept lengths. Fitted grain boundary scattering coefficients for ruthenium, rhodium, and iridium ($R \sim 0.4$ to 0.6) were significantly higher than for copper ($R = 0.29$), in good qualitative agreement with recent calculations [78], [98]. The model also found nearly specular interface scattering ($p > 0.9$) for ruthenium, rhodium, and iridium on SiO_2 but the interface scattering was much more diffuse ($p \approx 0$) for TaN/Ru/TaN and Ru/TiN indicating that specular interface scattering is not an intrinsic material property of ruthenium and surface scattering is very sensitive to the electronic structure at the interface (as shown by the fully diffused surface scattering in the case of ruthenium with a 0.3 nm TiN underlayer). This behavior is currently not yet well understood owing to the lack of a general predictive theory for the material dependence of interface scattering. The best available explanation comes from Zahid et al. [70] that correlates interfaces between material with

very dissimilar density of states to diffusive specular scattering. Other theories have been discussed as well. However, it should be noted that in all cases—irrespective of *p*—interface scattering contributed only weakly to the overall resistivity, which was dominated by grain boundary scattering, except for the thinnest TaN/Cu/TaN films. This was further corroborated by the temperature-dependent measurements where the temperature-dependent contribution to resistivity remained thickness independent. Furthermore, while using the Mayadas-Shatzkes model to understand the thickness dependence of resistivity, it is of critical importance to determine parameters such as the linear grain boundary intercept length experimentally that incorrect assumptions may lead to significant deviations.

Simulations within the Mayadas-Shatzkes model showed that the gains in resistivity upon annealing depend on the starting grain size. If the grain size initially is order of the mean free path, then annealing reduces the overall resistivity not only by increasing the grain size (hence the linear grain boundary intercept length) but also by reducing the *R*. However, if the initial grain size is greater than a factor of 4-5 of the mean free path, then the impact of annealing (i.e. further increase in the grain size, reduction in *R*) on resistivity is rather limited. This can again be attributed intrinsically to the mean free path. As the grains become much larger than the mean free path, the scattering at the grain boundaries have much smaller impact on the overall relaxation times. This was not easily observed for copper because of its much higher mean free path (~6x) when compared to ruthenium, which meant that the starting grains have to be much larger for copper for annealing to not show significant gains. Further simulations showed that the shorter mean free paths of the platinum-group metals were indeed responsible for the weaker thickness dependence of the thin film resistivity. This confirms earlier predictions [45], [46], [182] and justifies the usage of $\rho_0.\lambda_0$ as a figure-of-merit of alternative metals for beyond-copper interconnects in particular with respect to the expected scaling behavior [49], [100].

Chapter 5

Highly Scaled Ruthenium Nanowires

Problem Statement

In the previous chapter, it was experimentally observed that the transport properties in thin platinum-group metal films deviated significantly from the bulk, largely due to the contributions from grain boundary scattering, with surface scattering being significant only in certain cases. Though the scattering mechanisms responsible for the increase in resistivity in metallic nanowires (quasi-one-dimensional structures) are the same as in thin

---

Results from this chapter have been published in:

- S. Dutta, S. Kundu, A. Gupta, G. Jamieson, J. F. G. Granados, J. Bömmels, C. J. Wilson, Z. Tőkei, C. Adelmann, "Highly Scaled Ruthenium Interconnects," in *IEEE Electron Device Letters*, vol. 38, no. 7, pp. 949-951, July 2017. doi: 10.1109/LED.2017.2709248.

- S. Dutta, K. Moors, M. Vandemaele, C. Adelmann, "Finite Size Effects in Highly Scaled Ruthenium Interconnects," in *IEEE Electron Device Letters*, vol. 39, no. 2, pp. 268-271, Jan 2018. doi: 10.1109/LED.2017.2788889.

- S. Dutta, S. Kundu, L. Wen, G. Jamieson, K. Croes, A. Gupta, J. Bömmels, C. J. Wilson, C. Adelmann, and Z. Tokei, "Ruthenium interconnects with 58 nm^2 cross-section area using a metal-spacer process," in *Proceedings of IEEE International Interconnect Technology Conference (IITC)*, May 2017, pp. 1–3, doi: 10.1109/IITC-AMC.2017.7968937.

metallic films (quasi-two-dimensional structures), the case for nanowires is different and rather complex due to several differing factors, including four external surfaces (instead of two as in the case of thin films), two independent dimensions i.e., height and the width, and anisotropic grain sizes in the two directions perpendicular to the flow of current. In addition, resistivity models for nanowires are less developed when compared to thin films.

Platinum-group metals have shown promise to outperform copper (in terms of resistivity as well as reliability) at smaller linewidths but have so far lacked published experimental evidence especially at small dimensions (< 100 nm^2 cross-section area). In addition, the impact of scattering mechanisms at such scaled linewidths has not been investigated either. These can partly be attributed to the fact that fabricating such scaled structures is technologically complex using the conventional methods used in silicon technology.

Objectives

This chapter aims to investigate the scattering mechanisms in highly scaled (cross-section area < 200 nm^2) quasi-one-dimensional metallic structures.

Structure

The chapter presents a novel scheme to fabricate highly scaled (metallic) nanowires. Ruthenium nanowires are realized using the proposed scheme and the physical and electrical characteristics are discussed. This is followed by the resistivity modeling of nanowires, and a discussion on the scattering mechanisms along with the effect of dimensional parameters on the resistivity of nanowires.

5.1 Fabrication scheme

As discussed previously, the properties of platinum-group metals are quite attractive to be explored in smaller dimensions. In the previous chapters, the thin film properties were investigated; in this chapter, we shall discuss the physical and electrical properties of the nanowires.

Several methods, both top-down and bottom-up, exist to fabricate highly scaled structures. Nanowires have been fabricated using a number of techniques, and include (dual-) damascene [213], [214], [20], [215], multiple patterning [216], [217], electron beam lithography [218], [219], step-edge lithography [220], [221], direct-write ALD [222], vapor-liquid-solid (VLS) growth [223], [224], solid-liquid-solid (SLS) growth [225], area selective deposition [226], and bottom-up fill using nano-templating [227]. (Dual-) damascene and multiple patterning are getting increasingly (and will, in future, become prohibitively) complex and expensive with smaller technology nodes. With electron beam lithography, it's difficult to achieve structures below 10 nm [218] and also suffer from low throughput. Other techniques mentioned above are material-specific and sometimes require specific chemical reactions and often suffer from low yield.

Ruthenium nanowires, as small as 200 nm^2, have been demonstrated in the literature using a single damascene approach [20], [228]. However, scaling such approaches to smaller areas becomes increasingly complex in terms of both patterning as well as metallization. In this work, a novel albeit simple scheme to process off-pitch structures has been developed to fabricate metal nanowires with sub-100 nm^2 cross–section area. Such structures are sufficient to probe the electrical properties of the nanowires. Key advantages of the proposed scheme include no requirement for multiple pattering or chemical-mechanical polishing/planarization (CMP). Moreover, the scheme is sufficiently generic to be used to fabricate nanowires of a wide range of metals.

Ruthenium nanowires were processed using the above method on 300 mm wafers. A schematic of the nanowire processing flow is presented in **Figure 5.1**. SiO_2 cores of height 25 nm and width 300 nm were patterned on 300

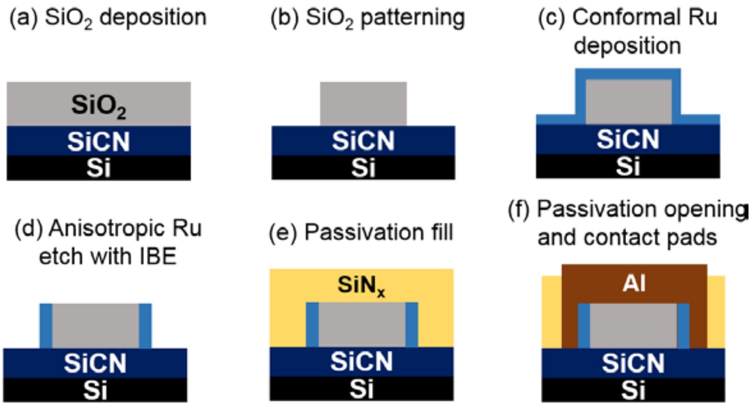

Figure 5.1 Schematic representation of the nanowire fabrication process. Nominally, two nanowires are produced in parallel; optionally, single nanowires can be obtained by lithographically masking one of the two parallel wires and removing the other by a "cut etch" (after the anisotropic etch). The dimensions of the nanowires can be controlled by tuning the film thickness, etch time, and height of the SiO_2 core

mm Si (100) wafers. Conformal ruthenium layer of 10 nm thickness is subsequently deposited on the cores using atomic layer deposition (ALD) from (ethylbenzyl) (1-ethyl-1,4-cyclohexadienyl) $Ru^{(0)}$ (EBECHRu $C_{16}H_{22}Ru$) and O_2. Details of process chemistry and growth mechanism is published elsewhere [205]. To improve adhesion between ruthenium and the SiO_2 cores, a 0.3 nm thick TiN layer was deposited by thermal ALD prior to Ru deposition [20]. The ruthenium deposition was then followed by an anisotropic etch resulting in ruthenium wires on the sidewalls of SiO_2 cores. Optionally, to obtain single wires, one of the two parallel wires can be lithographically masked and the other can be removed by a "cut etch" (no cut etch was used in this work; thus nominally, always two nanowires were measured in parallel). A $SiN_x/SiO_2/SiN_x$ passivation layer was then deposited and Al contacts were formed after passivation opening at the ends of the wires. Finally, all samples were annealed at 420°C for 20 mins in forming gas.

The dimensions of the ruthenium nanowires can be controlled through several parameters: varying the thickness of the metal layer, controlling the height of the SiO_2 core, and by adjusting the etch duration.

5.2 Nanowire fabrication with reactive ion etching

In the first approach to fabricate nanowires, a 10 nm ALD ruthenium film was deposited on the SiO_2 cores.

Reactive ion etching was used at the anisotropic etch step (**Figure 5.1 (d)**). Cross-section TEM images of the ruthenium nanowires after the etch is shown in **Figure 5.2**. As no cut etch was used in the fabrication process, nanowires can be observed on either side of the SiO_2 core. The nanowire profile is tapered (the *ellipsoidal* shape arises out of the imperfect etch of the SiO_2 core and of the nanowires) with typical cross-sections between 65 and 80 nm^2, as measured on several images. The sidewall (height) profile is rough (**Figure 5.2 (c)**). This arises due to the fact that ALD ruthenium grown with EBECH precursor on SiO_2 with a 0.3 nm TiN adhesion layer has a fiber texture in-plane [205] and the RIE etch rate is dependent on the grain

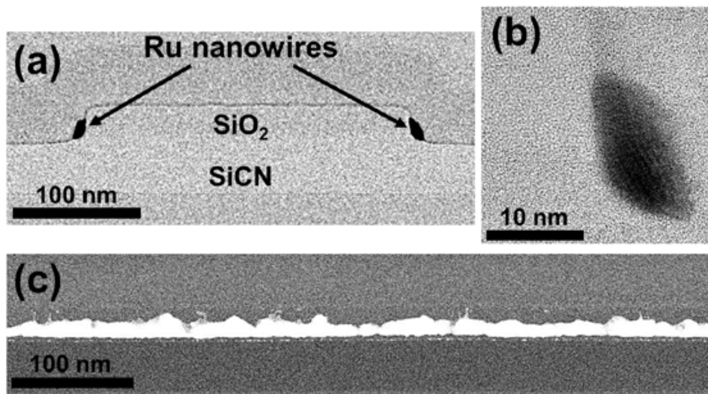

Figure 5.2 (a), (b) Cross-section TEM images across the nanowires. Physical area is ~65-80 nm^2. Nanowires can be observed on either side of the SiO_2 sidewall as no cut-etch was used. Nanowire profile ellipsoidal due to tapering at the top and bottom edges (c) TEM image along the nanowire. High roughness (variation in the height profile) observed due to differential etch rates of Ru planes during the RIE process. However, 7 μm lines were electrically conductive.

orientation (due to conformal film deposition at the sidewalls, the etch is in-plane).

5.2.1 Electrical characterization

The resulting nanowires were electrically measured for line resistance on 7, 47, and 97 μm long lines. Only 7 μm lines were found to be electrically active owing to the high roughness in the height profile observed that caused the longer lines to be discontinuous. The distribution of the resistance per unit length is shown in **Figure 5.3**. A bimodal distribution was observed with tight distribution within the two modes. The two modes can be attributed to the resistance of a single as well as double parallel nanowires. Out of the 200 nanowires measured (100 structures each with two nanowires in parallel), 53 structures had only one electrically active nanowire out of the nominal two (thus the yield of single nanowires, Y_{SN}, is 0.53), while 7 structures had both the nanowires in a conducting state (the yield of a double nanowire, Y_{DN}, is 0.07). So, the probability that a random nanowire is active is 0.335. Thus, the probability that both the nanowires in a measured structure are active is 0.11, which is similar to the yield obtained for double nanowires (Y_{DN}). Also, $Y_{DN} \sim \sqrt{Y_{SN}}$ indicates that the failure of the nanowires is random.

The resistivity and the electrical cross-section area were deduced from temperature-dependent electrical measurements. The technique is based on the fact that the total resistivity of a material (ρ) is the sum of resistivity contribution from lattice vibrations (ρ_T), which is temperature-dependent, and lattice imperfections (ρ_i) (including defects, impurities, and finite size effects) which are typically found to be independent of temperature. These contributions, to a first approximation, can be assumed to be independent of each other for pure metals. With the above assumptions, the temperature-dependent resistance measurements can be used to determine the electrical cross-section area (A_{el}) and resistivity (ρ) using [229]:

$$A_{el} = (d\rho/dT)*L*(dR/dT + R*CTE)^{-1} \quad (5.1)$$

$$\rho = (d\rho/dT)*R*(dR/dT + R*CTE)^{-1} \quad (5.2)$$

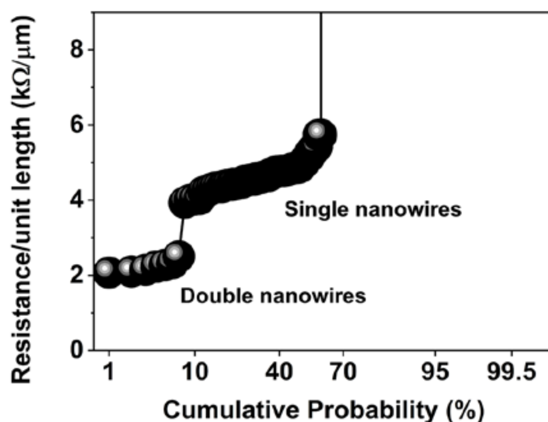

Figure 5.3 Cumulative probability distribution of the room temperature electrical resistance of the nanowires. A bimodal distribution is observed signifying single nanowires were obtained (and measured) in some cases and double in others. A combined yield (of single as well as double nanowires) of 60% was achieved. This translates into a 33.5% probability that a line is electrically active. (It is noted that all electrical measurements presented in Chapter 5 have < 1% error).

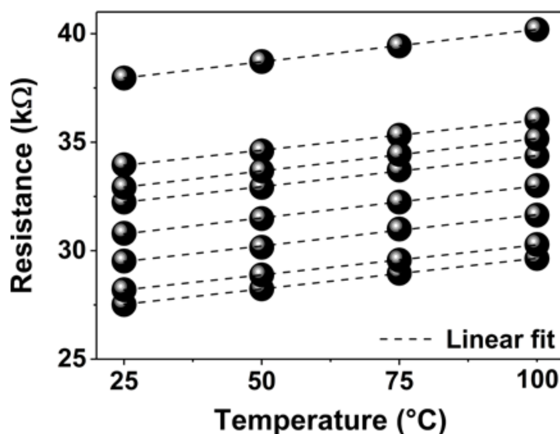

Figure 5.4 Temperature dependence of the electrical resistance of various ruthenium nanowires. Linear behavior is observed in all cases; a necessary condition to calculate the cross-section area from the temperature-dependent resistance measurements.

Here, L is the length of the wire, dR/dT is the experimentally determined linear temperature coefficient of the resistance, CTE is the coefficient of thermal expansion for Ru, and $d\rho/dT = 2.65\times10^{-8}\ \Omega\cdot\text{cm}\cdot\text{K}^{-1}$ [20], the linear temperature coefficient of the bulk ruthenium resistivity. If the wire can be assumed to be divided into smaller resistive elements, the total electrical area deduced from the temperature-dependent resistance measurements is the harmonic average of the smaller elements (see Appendix C). In the limiting case when the metal wires are open, then the area of one or more of the resistive elements is zero. Thus, the harmonic average of the all the areas becomes zero and so does the total electrical area.

Further, the term R*CTE denotes the effect of thermal expansion on the determination of the electrical area and the resistivity, and was found to be < 0.6%. The ruthenium nanowire resistance measured as a function of temperature was found to be linear up to the highest measured temperature of 100°C[35] (**Figure 5.4**).

The resistivity as a function of cross-section area of the nanowires is shown in **Figure 5.5**, and is compared with single damascene (SD) Ru lines from [20], [228]. The electrical cross-sectional area was between 58 and 69 nm^2, similar to cross-sectional area determined from the TEM images (65 to 80 nm^2). Since harmonic average is smaller than the arithmetic and geometric average, the electrical cross-section area calculated from the temperature-dependent resistance measurements apparently underestimate the physical area of rough limes measured from the TEM images. The higher resistivity of the Ru wires observed at smaller cross-sectional area is due to the increased scattering of charge carriers. This follows from the fact that as the

---

[35]Resistance measurements at higher temperatures might be affected by the changes in the microstructure and lead to much worse accuracy of the TCR measurements. For example, Cu is known to recrystallize >100°C [140]. Also, for ruthenium, in-situ sheet resistance measurements (Figure 3.5) show a decrease in resistance at temperatures >150°C. Resistances could be measured at lower temperatures to extend the temperature interval. Low temperature measurements were not feasible on the samples in this work due to the limitations of the measurement apparatus available. Additionally, from discussions with Dr. Takeshi Nogami from IBM about his work on Ru, Co, Cu, it is learnt that the linearity in resistance continues even at temperatures below 25°C unless the temperature is too low to see impurity and surface scattering residual resistivity components [230].

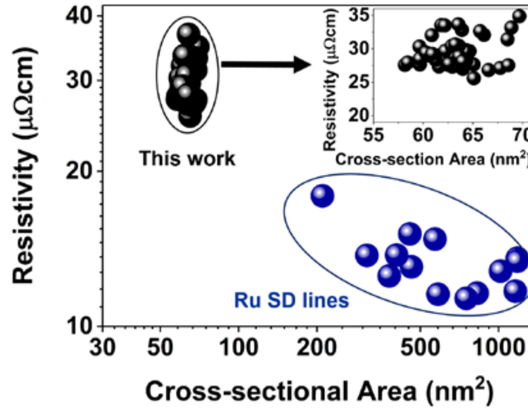

Figure 5.5 Resistivity of ruthenium nanowires as a function of cross-section area. Ruthenium single damascene data appended from [20], [228]. (The uncertainty in resistivity and cross-section area is <3% due to the variation in the reported values of dρ/dT for Ruthenium)

interconnect dimensions are reduced, the surface-to-volume ratio increases, thus more electrons are scattered at the surface.

5.2.2 Wafer-level reliability

Reliability is a critically important consideration for interconnects. Any serious candidate to substitute copper must demonstrate a robust reliability performance. In prior literature, arguments as well as ab-initio simulations have been made to correlate the interconnect reliability performance to the cohesive energy of the metal and, by extension, to the melting point [48], [231]. This is based on the argument that a higher cohesive energy of a material is indicative of a stronger binding between its atoms and would typically be able to withstand harsher thermoelectric stress. For instance, copper ($E_{cohesive}$: 4eV/atom) and tungsten ($E_{cohesive}$: 8.5eV/atom) interconnect structures have shown to have a better reliability performance than aluminum ($E_{cohesive}$: 3.4eV/atom [27], [48], [232], [233]. As such, platinum-group metals, with their cohesive energies >6 eV/atom [48] can be expected to show robust reliability. There have been limited reports of ruthenium reliability in literature demonstrating promising results [20], [108],

[215]. However, no data exists on ruthenium nanowires of sub-100nm^2 cross sectional area. In this section, an attempt has been made to probe the reliability of ruthenium nanowires of ~58-68 nm^2 cross-sectional area.

Wafer-level reliability tests were conducted on single ruthenium nanowires fabricated in this work to obtain a qualitative as well as a quantitative measure of their reliability. A quick and simple test could be to measure the fusing current density, J_{fuse}, that is the current density at which the wire breaks down (melts due to Joule heating) when a rapid current-sweep is applied. This can provide a good indication of the maximum current capability. Ruthenium nanowires were measured at room temperature and were found to fuse between the current densities of 530 and 720 MA/cm^2 with a median value of 650 MA/cm^2 (**Figure 5.6**). In comparison, copper has been reported with a J_{fuse} of ~100-160 MA/cm^2 whereas aluminum is reported to have a significantly smaller fusing current density of ~20 MA/cm^2 [234]. The superior current carrying capability of Ru nanowires can be attributed to its high cohesive energy of 6.74 eV/atom [48], and thus to its high melting point (2334°C) when compared to that of copper and aluminum. It is important that J_{fuse} should not be confused with the maximum current density, J_{max}, obtained from electromigration (EM) tests. (J_{max} is typically obtained by observing failures at high applied thermoelectric stress and extrapolating to expected operational conditions) but should only be used as a qualitative measure of the reliability performance.

To get an estimate of the lifetime, electromigration tests are conducted, which have now become a standard in the semiconductor industry [27], [234]. The basic theory is as follows: under a sufficient higher current density, electrons would collide with the metal atoms in the interconnect and cause them to migrate towards the anode. This atomic diffusion, in due time, could lead to void formation in the interconnect lines and result in an increase of the total resistance of the wire and impact the overall performance significantly. Thus, a higher current density exacerbates the electromigration phenomena. Furthermore, if the voids in the interconnect grow sufficiently large, it could result in an open. As device dimensions shrink and the requirement for the drive current increases, the current density through the interconnects increase rapidly. The electromigration lifetime, however, would decrease for a smaller interconnect structure as now the critical void size is smaller (critical

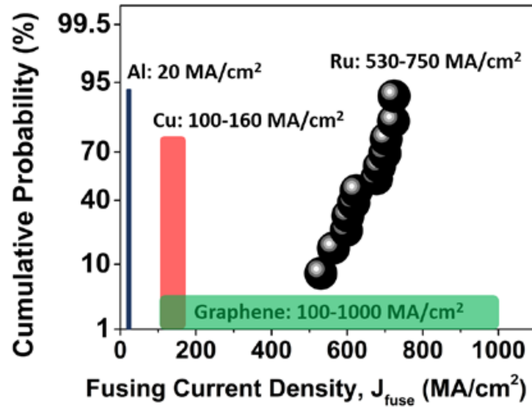

Figure 5.6 Fusing current density (J_{fuse}) of ruthenium nanowires, compared with J_{fuse} of copper, aluminum, and graphene. Median J_{fuse} obtained was 650 MA/cm^2. It is to be noted that fusing current density is not the same as the maximum current carrying capability (J_{max}) derived from electromigration measurements typically reported in the literature. (Due to the uncertainty in cross-section area being $<3\%$, the errors in the fusing current density for ruthenium are also $<3\%$)

void size scales proportionally with the interconnect dimension; electromigration failures result from a series of voids that eventually strings across a line, and should take longer for wider structures) and thus the reliability performance gets poorer at smaller dimensions [235], [236].

In electromigration tests, the interconnect structures are systematically failed by subjecting them to accelerated testing by the application of a very high thermoelectric stress. The failure times observed are then extrapolated to obtain the failure time under anticipated operating conditions. Under normal operating conditions ($T<100°C$, $J<1MA/cm^2$), interconnects may take long (from several months to years) before showing any signs of failure. Hence, it is not feasible to provide feedback to the manufacturing unit on process changes or evaluate interconnect performance rapidly. Thus, wafer-level electromigration tests can be carried out without the need for packaging. High temperatures and current densities (typically, $T>200$-$300°C$ and $J>2$-5 MA/cm^2) are employed to achieve short test durations, and in these methods, joule heating creates the stress temperature [237], [238]. However, such stress

conditions can also add a number of unintended effects to the measurements and are often used only as a qualitative indicator of reliability and electromigration.

No electromigration failure was observed when ruthenium nanowires were stressed at 200°C with 20 MA/cm^2 or 50 MA/cm^2 for one hour. Even at 100 MA/cm^2, no failure was observed upto four hours (**Figure 5.7**). The resistance of nanowires changed only marginally, by less than 2%, over the course of the measurement. In literature, there have been limited electromigration reports of ruthenium interconnects, however for much larger dimensions (>200 nm^2 cross-section area) and a smaller degree of thermoelectric stress [20], [108]. Copper or aluminum interconnects have not been reported to survive such high thermoelectric stress. Under the perspective that smaller structures will have shorter electromigration lifetimes [235], [236], the performance of ruthenium nanowires under the applied thermoelectric stress in this work demonstrate the potential for robust reliability performance for future ruthenium-based interconnect structures. Additional electromigration measurements on packaged structures will shed further light on the reliability of ruthenium nanowires at such small cross-sections.

The reason for ruthenium's ability to withstand such high thermoelectric stress could stem from the fact that the energy required for vacancy formation (E_{vf}) and vacancy migration (E_{vm}) in ruthenium is 2.68 and 2.17 eV, much higher when compared to that of copper (E_{vf}: 1.07 eV; E_{vm}: 0.72 eV) and aluminum (E_{vf}: 0.61 eV; E_{vm}: 0.58 eV) [31]. By extension, iridium (E_{vf}: 1.55 eV; E_{vm}: 2.54 eV) and rhodium (E_{vf}: 1.53 eV; E_{vm}: 1.25-1.47 eV) [31] nanowires too can be expected to demonstrate better electromigration performance. Similar arguments have been made elsewhere [48], [49].

In addition, the PAS measurements on ruthenium thin films indicated that the vacancy clusters do not dissociate till the highest measured temperature of 850°C (refer Chapter 3). Copper films, on the other hand, have been known to show vacancy cluster dissociation above 300°C [178]. As electromigration failure typically requires movement and agglomeration of voids downstream to form a critical void size, it is possible that the high stability of such vacancy clusters in ruthenium delays the formation of such

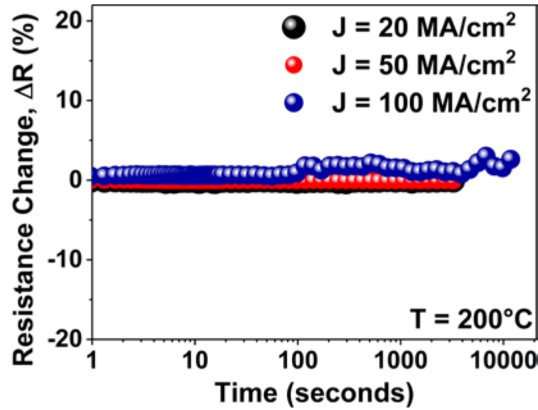

Figure 5.7 Time-dependent behavior of ruthenium nanowires under thermoelectric stress (wafer-level tests). Nanowires do not fail upto ~4 hours under the highest applied thermoelectric stress of J=100 MA/cm^2 and T=200°C, indicating potential of ruthenium nanowires to demonstrate robust reliability.

a critical void, thus allowing for a robust electromigration performance observed. Finally, it is also speculated that vacancy cluster dissociation scales with the cohesive energy of metals and might be observed for ruthenium at higher temperatures (850-2300°C).

5.3 Nanowire fabrication with ion beam etching

As observed in the previous approach to nanowire fabrication with reactive ion etching, the height profile of the nanowires (along the line) was rough owing to the differential etch rate of (002) and (101) ruthenium planes (**Figure 5.2 (c)**). To mitigate this issue, ion-beam etch was used in the next iteration, as a physical etch process should, in principle, be transparent to etching different crystal orientations than RIE. Also, to obtain a wide spread in the cross-section area of the nanowires, a design-of-experiment (DOE) was created with varying film thickness (8, 10, 12 nm), etch duration (0.8, 1.0, 1.2 x 'best known method' (BKM)), and etch bias (400V, 200V) (**Figure 5.8**).

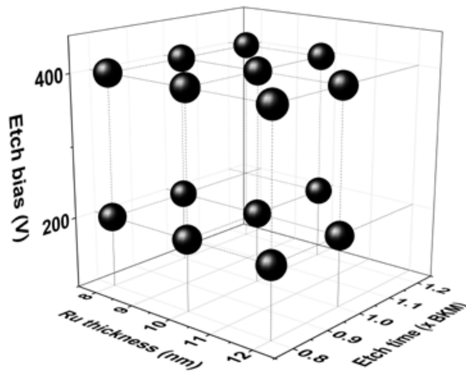

Figure 5.8 Design of Experiment used to create nanowires of varying cross-sectional areas. The DOE splits on film thickness (8, 10, 12 nm), etch duration (0.8, 1.0, 1.2 x BKM), and etch bias (400V, 200V).

Cross-sectional transmission electron microscopy (TEM) images of the wires, across and along the wires, together with elemental mapping are shown in **Figure 5.9**. TEM images taken across the wires correspond to the structure shown in **Figure 5.1 (e)**. The nanowire profile is tapered with an ellipsoidal shape, similar to what was obtained by RIE (**Figure 5.2 (b)**). Thus, the change in the etch process did not have any improvement on the nanowire cross-sectional profile. The typical cross-sections of the ruthenium nanowires were between:

- 40-59 nm^2 (**Figure 5.9 (b)**) for wires fabricated with ruthenium film thickness of 8 nm, etch time of 58 seconds, and an etch bias of 400 V
- 80-113 nm^2 (**Figure 5.9 (c)**), for a ruthenium film thickness of 8 nm, etch time of 48 seconds, and an etch bias of 400 V, and
- 95-120 nm^2 (**Figure 5.9 (d)**) for a ruthenium film thickness of 10 nm, an etch time of 114 seconds, and an etch bias of 200V

The height of the nanowires was between 14.5 nm and 17 nm with a smooth profile (**Figure 5.9 (e)**). As expected, the ion-beam milling, being a physical process, maintained a similar etch rate between different ruthenium planes

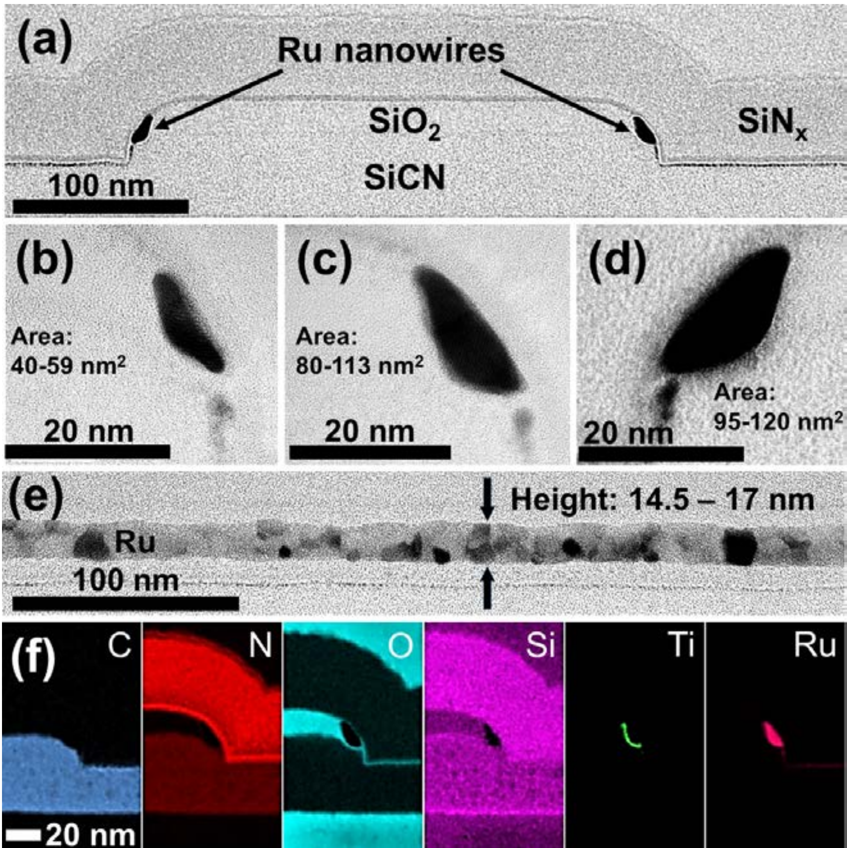

Figure 5.9 Cross-section TEM images **(a)-(d)** across the wire structures with their corresponding cross-sectional areas. Electrical cross-sectional area deduced for images in (c) and (d) is ~ 90 nm^2, consistent with the TEM area **(e)** TEM images along the nanowire. Sidewall roughness profile varies between 14.5 and 17 nm **(f)** Elemental mapping (EELS) of C, N, O, Si, Ti, Ru across the wires. Presence of Ru and O can be observed on regions on SiCN field not covered by SiO_2 cores. This can be attributed to redeposition during the ruthenium etch process and subsequent oxidation during air exposure. However, electrical measurements on fork structures confirmed that these RuO_x layers were electrically discontinuous (Map contrasts are optimized to show element distributions)

thus yielding comparatively low roughness to the previously used RIE etch process. Elemental mapping using electron energy loss spectroscopy (EELS) confirm the homogeneous distribution of ruthenium in wires, without any voids (**Figure 5.9 (f)-Ru**). Thus, the conformal deposition of ruthenium was excellent and the film was closed. EELS mapping also show the presence of Ti in the adhesion layer (**Figure 5.9 (f)-Ti**). Additionally, the presence of ruthenium and oxygen (RuO_x) could be noticed on regions on SiCN field not covered with SiO_2 cores (**Figure 5.9 (f)-Ru/O**). This can be attributed to redeposition during the ruthenium etch process and subsequent oxidation during air exposure. This could have posed a problem of short between the structures as ruthenium oxide is known to be conductive [239], however electrical measurements on fork structures confirmed that these RuO_x layers were electrically discontinuous (data not shown), and thus there is no need to have an additional etch (cleaning) step to remove the RuO_x layer.

5.3.1 Electrical characterization

Resistances were measured on the nanowires with lengths of 7, 47, 97, 485, and 1455 μm (each structure has two nanowires in parallel, and resistance for a single nanowire is obtained by nominally multiplying the measured resistance by two. It is thus assumed that both nanowires are similar). The distribution of resistance per unit length is shown in **Figure 5.10**. Excellent yields, in excess of 80%, were obtained even on the longest measured lines of 1455 μm, owing to the fact that the height profile of the nanowires obtained by IBE had limited variation that enabled nanowires to be electrically active over longer lengths. In addition, resistances measured on varying length of wires generally scaled well per unit length, demonstrating the fidelity of the fabrication process. The smallest electrical cross-section area of the wires was calculated (from equations 5.1, 5.2) to be 33 nm^2, in reasonable agreement with the corresponding physical area determined from TEM images (**Figure 5.9 (b)**) of 40-59 nm^2. The observed difference could arise from high roughness and/or etch damage resulting in the increased line resistance which, from equation (5.1), would result in a lower electrical cross section area. Nevertheless, the results are in reasonable quantitative agreement.

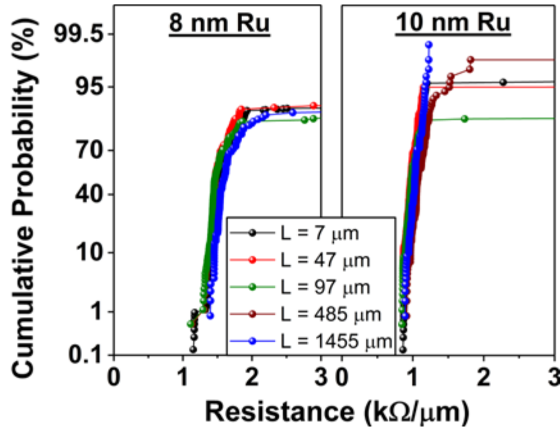

Figure 5.10 Room temperature electrical resistance per unit length of ruthenium nanowires fabricated with different ALD Ru film thicknesses (**Figure 5.1 (c)**) and same etch conditions. Yields in excess of 80% is observed (only selected experimental points from the DOE described in **Figure 5.8** is shown)

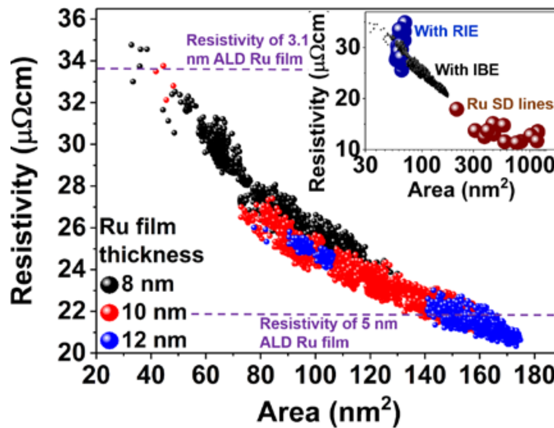

Figure 5.11 Resistivity of nanowires as a function of cross-section area fabricated from different ALD ruthenium film thicknesses (8, 10, 12 nm) in **Figure 5.1 (c)**. Additionally, shown are the resistivity of 3.1 and 5 nm ALD Ru films. (Inset: comparison with Ru single damascene lines [20], [228]). The uncertainty in resistivity and cross-section area is <3% due to the variation in the reported values of dρ/dT for ruthenium.

At the time of writing, these are the smallest reported dimensions of ruthenium nanowires. For nanowires shown in TEM images of **Figure 5.9 (c)** and **5.9 (d)**, the deduced electrical cross-section area was ~90 nm^2, for estimated physical areas of 80-113 nm^2 and 95-120 nm^2, underlining the good estimation capability of the temperature-dependent resistance measurement method in determining the cross-section area of the wires.

The cross-section area dependence of resistivity of the ruthenium wires is plotted in **Figure 5.11**. For comparison, the resistivity of ruthenium interconnects from previously published work is also shown [20], [228]. The nanowires show an increase in resistivity with decreasing cross-section area that can be ascribed to the increasing impact of surface and grain boundary scattering at smaller dimensions (the phenomenon has been discussed in detail in earlier chapters). Furthermore, nanowires with similar electrical cross-section area (between 80 and 120 nm^2) but fabricated with different ruthenium film thickness (8, 10 nm) vary slightly in resistivity, with nanowires with 8 nm starting film thickness being higher in resistivity. This could be qualitatively attributed to the smaller grain size expected for a thinner film as compared to a thicker film. Such dependence of grain size on film thickness has been discussed in Chapter 4.

5.3.2 Resistivity modeling of ruthenium nanowires

In this section, an attempt is made to compute the area dependence of resistivity of ruthenium nanowires without the use of any free parameters.

Similar to the thin films, the increase in resistivity of nanowires at smaller cross-sectional area (**Figure 5.11**) may be ascribed to the contributions from surface and grain boundary scattering. However, the models for nanowires are less developed when compared to thin films and their relative contributions are limitedly understood. Modeling a nanowire is different on various accounts than for thin films; the surface-to-volume ratio is higher (for a rectangular nanowire, there are four surfaces/interfaces instead of the two for films), and two independent dimensional parameters (height and

width) instead of one. Moreover, as discussed earlier, the existing models require a number of parameters that are often not feasible to determine experimentally (and include micro-scale surface roughness, correlation length, coherence length, relaxation times to name a few). As such, these parameters are also used as fitting parameters in the model which then artificially improves the fitting.

The semi-classical model of Mayadas-Shatzkes was specifically developed for thin films, but can however be modified for (rectangular) nanowires by imposing another boundary condition to its dimensions i.e., a nanowire can be thought of a thin film with a finite thickness/height as well as a finite width *w*. The idea has been demonstrated schematically in **Figure 5.12**.

The Mayadas-Shatzkes formulation for thin film resistivity in equation (2.13) can be represented equivalently as follows:

$$\rho_{tf} = \left[\frac{1}{\rho_{GB}} - \frac{1}{\rho_{GB,SS}}\right]^{-1} \tag{5.3}$$

The addition of another boundary condition (due to finite width) can be affected as follows:

$$\rho_{nw} = \left[\frac{1}{\rho_{GB}} - \left(\frac{1}{\rho_{GB,SS-h}} + \frac{1}{\rho_{GB,SS-w}}\right)\right]^{-1} \tag{5.4}$$

Thus, the full numerical expression of the above equation takes the form:

Figure 5.12 Schematic representation of a (rectangular) nanowire as though to be a thin film with an additional boundary condition (due to finite width)

$$\rho_{nw} = \left\{\frac{1}{\rho_{GB}} - \left[\frac{6(1-p)\lambda}{\pi\rho_0}\left(\left(\frac{1}{h}\int_0^{\pi/2} d\varphi \int_1^{\infty} dt \frac{\cos^2\varphi}{H^2}\left(\frac{1}{t^3}-\frac{1}{t^5}\right)\frac{1-e^{-k_1 tH}}{1-pe^{-k_1 tH}}\right) + \left(\frac{1}{w}\int_0^{\pi/2} d\varphi \int_1^{\infty} dt \frac{\cos^2\varphi}{H^2}\left(\frac{1}{t^3}-\frac{1}{t^5}\right)\frac{1-e^{-k_2 tH}}{1-pe^{-k_2 tH}}\right)\right)\right]\right\}^{-1} \quad (5.5)$$

where $k_1 = \lambda_0/h$ and $k_2 = \lambda_0/w$. 'ρ_{GB}' and 'H' are the same from equations (2.9) and (2.14) respectively. The linear intercept length *g*, measured from **Figure 5.9 (e)**, is 9.3 nm. As different cross-section areas of the nanowires, for a given film thickness, were obtained by varying the etch parameters, the linear intercept length is not affected.

The height and the width of the wires are determined from TEM images (**Figure 5.9**) for the smallest and largest cross-section areas and interpolated for areas in between. The *p* (=0.01) and *R* (=0.42) values, along with the uncertainty, are taken from Table 4.2 for ALD Ru films on 0.3 nm TiN-SiO_2 as the same ALD process has been used to fabricate the nanowires that were used to deposit and model ALD ruthenium films. The assumption here that the *nature* of the surface and the grain boundary scattering remains the same between the films and the nanowires is reasonable due to the use of the same stack – ALD Ru on 0.3 nm TiN- and the same ALD Ru deposition conditions. Moreover, *p* is ~0 and cannot reduce further. *R* is the effective reflection coefficient of electrons from the grain boundaries. Given that the grains inside the nanowires do not favor any particular arrangement (**Figure 5.9 (e)**), it is a valid assumption to use the same *R* as that for the ALD Ru films on 0.3 nm TiN.

It needn't be necessary that the film deposited by ALD on the sidewalls of the core has the same microstructure than obtained from blanket experiments. However, this was not really assumed in the analysis of the resistivity. The linear intercept length of the wires in the transport direction was measured experimentally for the wires and was found to be 9.3 nm with an uncertainty of 1.3 nm. Possible differences could still include texture but ALD Ru grown on 0.3 nm TiN are rather randomly oriented and there is no real reason to assume that this changes on sidewalls. The TiN was deposited by ALD, which is highly conformal. As discussed above in detail, deviations from bamboo-like structures might lead to changes in the effective *R* value

but not to completely different thickness dependences. The results in the manuscript indicate that the *R* values obtained for thin films are also relevant for nanowires, which in turn indicates that there is no evidence suggesting that the microstructure is clearly different on the sidewalls of the core than on thin films.

The computed resistivities using equation (5.5) were slightly lower than the experimental values (**Figure 5.13**). The uncertainty in resistivity and cross-section area is <3% due to the variation in the reported values of $d\rho/dT$ for ruthenium. This may be because the ruthenium interconnects were only annealed after full dielectric passivation of the films. This typically leads to reduced recrystallization and smaller grains than annealing of structures with free surfaces. As already discussed in Chapter 4 for ruthenium films on SiO_2 (Table 4.1), annealing reduces *R* in parallel to the recrystallization. Thus, the observed deviation may be attributed to a slight underestimation of the *R* value obtained from the annealed ALD ruthenium films (with a free surface). Additionally, deviations at smaller cross-section areas (<70 nm^2) are likely due to effects than are not captured by the semi-classical Mayadas-Shatzkes model. In the simple Mayadas-Shatzkes model, the maximum contribution of surface scattering is obtained for $p = 0$, *i.e.* for fully diffuse scattering at a completely flat boundary surface. In very narrow wires, such boundary roughness effects are expected to become more pronounced due to a non-negligible probability of having sequential scattering events (*i.e.* the surface acting like a trap) or an effective reduction of the cross-sectional area. This may lead to a resistivity contribution of surface scattering even higher than for $p = 0$, which may in turn explain the systematic underestimation of the resistivity at small areas.

Despite this, reasonable agreement between experimental and modeled resistivity was obtained using parameters obtained from thin film experiments. Note that no fitting was performed to adjust the computed resistivity to the experimental data. This indicates that the parameters obtained by ruthenium thin film resistivity modeling also apply (in good approximation) to ruthenium wires and that much simpler thin film experiments may be used to predict the resistivity of scaled interconnects with reasonable accuracy.

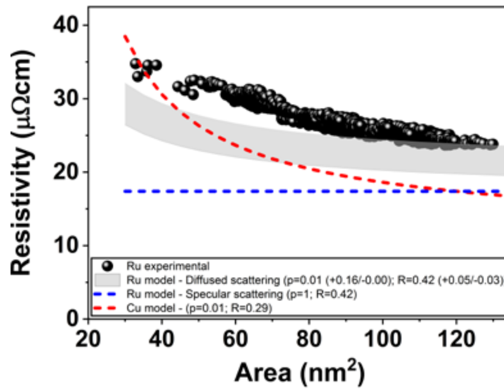

Figure 5.13 Computing the area dependence of resistivity of ruthenium nanowires using the p (=0.01; diffusive scattering) and R (=0.42) obtained from thin film resistivity modeling of ALD Ru on 0.3 nm TiN. In addition, a hypothetical case is simulated for Ru nanowires with fully specular (p=1) scattering. Thus, surface scattering causes the slope of the area dependence of resistivity while grain boundary scattering is the dominant scattering mechanism except for the smallest areas. For comparison, resistivity of Cu nanowires as a function of area is generated with p=0.01 and R=0.29. Stronger area dependence of resistivity for Cu was observed compared to Ru (from thin film modeling, weaker thickness dependence of resistivity for Pt-group metals was attributed to their smaller mean free path when compared to Cu). Furthermore, simulations suggest the crossover between the resistivity of Ru and Cu nanowires to be at ~40 nm² (for the parameters used here).

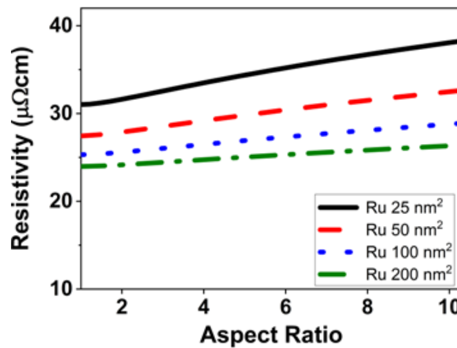

Figure 5.14 Simulated resistivity of Ru nanowires as a function of aspect ratio for various cross-sectional areas. A higher aspect ratio has a comparatively stronger impact on resistivity at smaller cross-sectional areas. Even then, the impact is marginal for realistic aspect ratios (for e.g., between 3 and 1). Thus, the cross-section area principally determines the resistivity of the nanowires and the effect of the aspect ratio is marginal.

A calculation under the assumption of fully specular scattering at the interfaces (p = 1, all other input parameters remain identical) is also shows as a dashed line in **Figure 5.13**. The difference between the experimental data and the dashed line can be roughly considered as the contribution of surface scattering to the resistivity. Thus, grain boundary scattering is the dominant contribution to the resistivity, except for the smallest areas where surface scattering contribution rises.

For comparison, the resistivity of copper wires was computed as a function of the cross-sectional area using p (= 0.01) and R (= 0.29) as obtained from resistivity modeling of thin copper films (Table 4.1). Dimensional parameters and the linear intercept length was kept the same as that of ruthenium wires. The area-dependence of resistivity of copper wires was found to be stronger than that of ruthenium due to its much larger mean free path (same was

observed in the case for thin films). Additionally, simulations predict the cross-over between the resistivity of copper and ruthenium wires to be ~40 nm^2 (for the parameters used here) below which ruthenium wires would have lower resistivity.

Using the semiclassical model, the effect of the aspect ratio (AR) on the resistivity of ruthenium nanowires can be examined. The resistivity of nanowires at a fixed cross-sectional area (**Figure 5.14**) shows a rather weak dependence on the aspect ratio of the structures. Simulations predict for the smallest simulated cross-sectional area of 25 nm^2, the decrease in resistivity from an AR of 4 to 1 is only ~8%, and <2% when reducing the AR from 2 (a more realistic value for interconnect structures) to an AR of 1. For the largest simulated cross-sectional area of 200 nm^2, the change in resistivity is even smaller; ~3% from an AR of 4 to 1, and <1% when reducing the AR from 2 to 1. This indicates that the resistivity is predominantly determined by the cross-sectional area of the wires and depends only weakly on the aspect ratios. This is likely due to the fact that both the height as well as the width of the wires is of the order of or below the mean free path, and while the contribution of grain boundary scattering to resistivity remains constant (linear intercept length is constant), the contribution of surface scattering to resistivity does not change drastically within the aspect ratios examined here. These results further suggest that the gains of aspect ratio engineering would

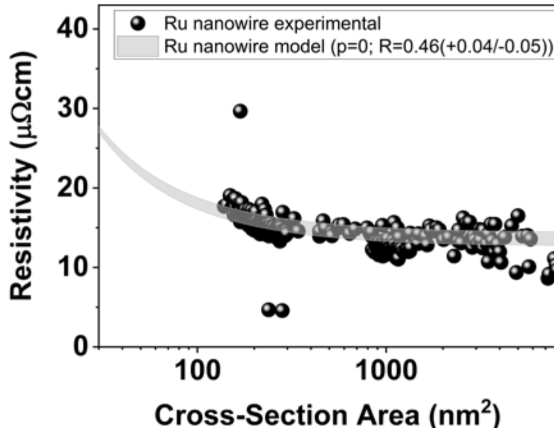

Figure 5.15 Computed area dependence of resistivity of DME Ru nanowires using $p = 0$ (diffused surface scattering) and $R = 0.46$ (+0.04/-0.05) (for PVD ruthenium; **Table 4.1**). A good match between the calculated and the experimental values shows that the nanowire model can be successfully adapted to different fabrication techniques. The uncertainty in resistivity and cross-section area is <3% due to the variation in the reported values of $d\rho/dT$ for Ruthenium.

be limited even at smaller cross-sectional areas. Furthermore, this suggests that the shape of the wire for a given cross-sectional area might not significantly affect the resistivity and thus a simplistic rectangular profile for the wires assumed here remains valid.

Additionally, to examine the flexibility of the semi-classical model for the nanowires proposed in this work, the area dependence of resistivity was calculated for ruthenium nanowires fabricated using a different (direct metal etch - DME) approach[36] than used in this work [240]. In this case, the ruthenium film was deposited using PVD. The height of the nanowires was kept constant at 24 nm and the width was varied to obtain a spread in the cross-section areas. The linear intercept length was 28 nm. To compute the

[36]The experimental data of DME Ru nanowires is courtesy Danny Wan (imec). The fabrication and characterization of these nanowires are not a part of this dissertation. The data is used only to demonstrate the versatility of the nanowire resistivity model proposed in this work.

resistivity, an *R* of 0.46 was used as obtained by modeling the thickness dependence of PVD ruthenium films (**Table 4.1**). Also, the ruthenium films were deposited on a 0.3 nm TiN layer and thus a *p* of 0 is used. The computed resistivity of DME ruthenium nanowires along with the experimental values is presented in **Figure 5.15**, and a very good agreement is observed between them.

The DME ruthenium nanowires differ in several aspects than the nanowires fabricated in this work (viz, film deposition technique, fabrication method, nanowire dimensions and the range of cross-section areas). The excellent agreement between the computed and the experimental values demonstrates the versatility of the nanowire model developed and used in this work.

5.4 Chapter summary

This chapter contributes towards expanding the current understanding of the resistivity scaling in quasi-one-dimensional metallic structures.

A major limitation towards achieving that goal in the past has been the lack of simple test vehicles that allow fabrication of such structures with high fidelity. This work tackles the issue by proposing a generic, CMOS-compatible scheme to fabricate highly scaled nanowires. This has allowed to fabricate ruthenium nanowires, down to 33 nm^2 in cross-sectional area, and probe the scattering mechanisms.

Grain boundary scattering was found to be the dominant mechanism contributing towards increased resistivity in scaled nanowires, except for very small cross-sectional areas where the contributions from surface scattering became significant. The probing into the scattering mechanisms was enabled by a proposition made in this work to adapt the Mayadas-Shatzkes model of thin films for nanowires with a rectangular cross-section. This further allows for the computation of resistivity of nanowires without the use of any free parameters. The significance of this can be gauged by the fact that the existing models to calculate the resistivity of nanowires require a number of parameters that are often difficult to be determined by theoretical or experimental methods [53], [185], [185], [186], [241]. Moreover, the versatility of the proposed model was demonstrated by excellent agreement of the

calculated resistivity values as a function of cross-section areas for two different ruthenium datasets. Additional simulations within the model strongly suggest that the resistivity (of ruthenium nanowires) is primarily determined by the cross-section area and engineering the aspect ratio has minor impact. This is argued to be due to the shorter mean free path of ruthenium as opposed to that of copper. Historically for copper, the interconnect structures were designed to be as close as possible to the 1:1 aspect ratio. However, for ruthenium (and, by extension, for other platinum-group metals) such considerations will have very limited gains on resistivity.

Through wafer-level tests, ruthenium nanowires demonstrated the potential for robust reliability. This can be attributed to the high energies for vacancy formation and vacancy migration in ruthenium. Additionally, the stability of vacancy clusters in ruthenium even at elevated temperatures (refer section 3.2.1) possibly delays the formation of a critical void size needed for EM failure thus allowing high resistance to failure.

Chapter 6

Conclusion

This dissertation was primarily aimed at expanding the current understanding of the scattering behavior of metallic nanostructures at reduced dimensions. The focus has been on the platinum-group metals which have shown immense potential for future interconnect applications.

The resistivity of nanostructures is higher than in the bulk and is due to the additional contributions from scattering at the interfaces and at the grain boundaries. These have been explained by the (semi-) classical models of Fuchs-Sondheimer and Mayadas-Shatzkes. Though the models are several decades old and have their limitations, it has been shown that, if accounted appropriately for the microstructure, these models are still applicable and can provide valuable insights into the scattering mechanisms. Thus, strong emphasis was laid on the microstructural characterization in this work which strongly complemented the resistivity modeling. Several datasets of ruthenium thin films were modeled and consistent results were obtained indicating the robustness of the approach.

The literature on copper has been divided on the dominance of surface and grain boundary scattering contribution to resistivity. We have shown that this could, in part, be due to incorrect assumptions of the linear grain boundary intercept length (~film thickness, for example). That said, for all thin films (of the platinum-group metals as well as copper) studied in this work, grain boundary scattering was the dominant mechanism for increase in resistivity at reduced dimensions, except for the thinnest films of copper.

Furthermore, the thickness dependence of resistivity was generally weaker for all the platinum-group metals when compared to that of copper. It was shown that this is intrinsically due to the shorter mean free path of the platinum-group metals. This allowed for a crossover in resistivity with copper at smaller dimensions. From a technological point of view, this resistivity crossover renders platinum-group metals, in particular rhodium, ruthenium, and iridium, highly interesting for scaled interconnects with critical dimensions of 10 nm and below, where the current combination of copper, diffusion barriers, and adhesion liner layers may be outperformed by barrierless rhodium, ruthenium, or iridium metallization. Indeed, scaled ruthenium filled interconnect structures have already shown first promising results [20] demonstrating the prospects of these materials for future interconnect technology nodes.

The study of annealing behavior of thin ruthenium films revealed profound insights into the behavior of the material. First, stress relaxation was already seen to begin ~200°C. The evidence of vacancy clustering in thin ruthenium films is particularly interesting for its possible application in interconnects. The movement of vacancies in interconnects plays a vital role in stress redistribution along the length of an interconnect structure. Presence of a vacancy allows for the surrounding lattice to relax increasing the tensile stress or reducing the compressive stress. In contrast, increased atomic flux elsewhere would have the opposite effect. As such, the onset of vacancy migration in thin ruthenium films already at 200°C could have an impact on the electromigration lifetimes of ruthenium interconnects (though it must also be mentioned that passivated interconnect structures could have additional stresses resulting from a mismatch between the passivation layer and the interconnect during deposition and subsequent processing, and also from a high applied current density). It has been reported that the presence of stress in copper interconnects has a significant impact on the reliability; passivated copper interconnects with compressive stress at the interfaces arrests material diffusion [242], thus positively influencing electromigration lifetimes, whereas tensile interfacial stress is detrimental to reliability and increases the chances of failure [38].

Second, the electrical properties were deeply impacted by recrystallization and grain growth as opposed to the mechanical properties (stress).

Ruthenium films recrystallized at ~450°C and is lower than the typical recrystallization temperatures of metals reported in literature in relation to their melting point (T_{recrys} ~0.33-0.50 of the melting point [139]). This resulted in a significant decrease in resistance by upto ~27% for the film studied in this work. Such gains in resistance at backend compatible thermal budgets would lead to substantially better performance.

It was further seen that the surface scattering behavior was sensitive to the *cladding* material and that even a 0.3 nm thick TiN changed the nature of surface scattering from fully specular to diffusive. This behavior is not well understood owing to the lack of a general predictive theory of the material dependence of p in the literature. It has been argued that surface scattering depends solely on the roughness [67] while counter-arguments have attributed it to the *cladding* material [70]. It has been shown through ab-initio simulations that microscopic surface roughness[37] (that is typically of the order of the electron wavelength, ~0.5 nm) can indeed change the contribution of surface scattering [13] but, in reality, it is not feasible to experimentally measure roughness at such length scales with the methods available today. There was also an excellent experiment conducted by Rossnagel et al. [13] where the resistivity of copper films with tantalum *cladding* showed an increase in resistivity (as opposed to no *cladding*), however, the increase relaxed when the *cladding* was allowed to oxidize in air. This indeed is a compelling argument on the dependence of surface scattering on the *cladding* material. However, it can be questioned that the microscopic surface roughness could have changed at the surface due to the oxidation of the *cladding* material. More (ab-initio) work is needed in this regard to fundamentally understand surface scattering. Technologically however, the detrimental effect of *cladding* on surface scattering can have implications on the resistivity of interconnects when using very thin adhesion liners.

For the case of ruthenium nanowires, grain boundary scattering was again the dominant mechanism contributing to resistivity, except at very small cross-section areas. The adapted Mayadas-Shatzkes model for (rectangular) nanowires explained remarkably well the area dependence of resistivity and

[37]Microscopic surface roughness is different than the mesoscopic surface roughness. Roughnesses measured through AFM provides mesoscopic roughness.

was found to be quite versatile as well. This further underlines the relevance of thin film resistivity modeling and the applicability of its learnings to nanowires. Further simulations within the model strongly suggest that the resistivity (of ruthenium nanowires) is primarily determined by the cross-section area and engineering the aspect ratio will have minor impact. Aspect ratio engineering has been one of the ways for the designers to reduce the interconnect resistivity. Thus, the use of metals with low mean free path will restrict that option. Nonetheless, in the area range up to 350 nm^2 and higher, it has been shown that copper resistivity is lower than that of ruthenium due to its lower bulk resistivity [20], however copper resistivity is expected to rise sharply below 200 nm^2 [214]. The area dependence of the copper resistivity has been shown to be stronger than that of ruthenium thin films [243], thus making ruthenium an attractive interconnect candidate for small line widths, in particular as it has been shown that ruthenium does not require barrier layers to prevent from diffusion into surrounding dielectrics [20]. The promise of ruthenium for interconnect applications was further corroborated by the robust wafer-level reliability observed for ruthenium nanowires. This was not only due to the high cohesive energy of ruthenium but can also be attributed to the high stability of vacancy clusters in ruthenium as learnt for the PAS measurements.

Cobalt is indeed another potential candidate being considered to replace copper in the interconnects due to its reduced sensitivity to scattering at smaller dimensions, low bulk resistivity, and higher cohesive energy [49], [100]. In addition, practical advantages such as, lower material cost (when compared to the Pt-group metals) and familiarity with ULSI processing (cobalt is used as liners for copper interconnects for better adhesion and improved reliability) make it attractive for interconnect applications. Intel is expected to use cobalt in their 10-nm technology [244]. However, it has not been introduced in any available chips yet. GlobalFoundries will continue to use copper for their 7-nm node [245]. Other players in the industry haven't yet announced a move away from copper. Thus, copper being replaced by cobalt in interconnects is not yet a general industrial practice.

Comparing cobalt and ruthenium, ruthenium is expected to be less sensitive to size effects due to a lower product of the bulk resistivity and the mean free path [100] assuming all extrinsic parameters remain same (interface, grain

size, material homogeneity in interconnect structure). A higher cohesive energy of ruthenium [48], [49] would not only enable better electromigration [112] but also possibly eliminating the need for a diffusion barrier [20], [228]. Unit material cost for ruthenium is higher than that of cobalt. However, and as has been discussed earlier, since the gains in resistivity, and thus resistance, of using alternative metals in place of copper is only at very small length scales, use of alternative metals for only the most critical interconnect structures while still using copper for the relaxed dimensions is recommended.

From the experiments and simulations on thin films and nanowires, platinum-group metals (especially ruthenium, rhodium, and iridium) have indeed shown potential to replace copper in future interconnect structures with scaled widths of 10 nm and below.

6.1 Outlook

This section outlines recommendations to expand the scope of this work.

- It has been sufficiently established that the surface scattering is not an intrinsic property of a material and that *cladding* around the film significantly affects the nature and thus contribution of surface scattering to resistivity. Though this effect has been explored in this work but is not well-understood as the literature lacks a model that accounts for the material dependence of scattering from the interfaces. Such a model will account for the film material and further relate the scattering behavior to a physical property of the *cladding*.

- The Mayadas-Shatzkes model describing the thickness dependence of resistivity has several assumptions, including planar interfaces and isotropic fermi surfaces. An improved model that accounts for anisotropic fermi surfaces and surface roughness would further the applicability of the Mayadas-Shatzkes model.

- It was also reported that ALD ruthenium grown on TiN using the EBECH precursor causes segregation of Ti inside the ruthenium film which apparently affects its annealing behavior (texture, recrystallization temperature). It was speculated that the segregated Ti preferentially occupies grain boundaries and increases the activation energy for grain boundary movement. Atom probe tomography could help map the distribution of Ti inside the ruthenium films and strengthen the argument.

- It has been reported (for copper nanowires) that the presence of impurities at the grain boundaries reduces resistivity by lowering the number of empty states around the Fermi energy in the boundary plane region of the grain boundary [211]. The same effect could be exploited to lower the resistivity of ruthenium interconnects grown on TiN with Ti segregation at the grain boundaries. Furthermore, in the case of copper interconnects, it has been shown that impurities segregating at the grain boundaries have a positive impact on reliability and improves electromigration lifetimes [38], [206], [246], [247]. Such effects would be interesting to be explored in future for ruthenium interconnects.

- Through various figures-of-merit (discussed in Chapter 2), ruthenium, rhodium, and iridium were shortlisted as the most promising candidates for interconnect applications. Other candidates were cobalt and niobium which are also expected to demonstrate weaker thickness dependence of resistivity. An investigation into their thin film properties could shed light into the scattering mechanisms.

- A novel vehicle to fabricate highly scaled (pseudo-)-one-dimensional (metallic) structures was proposed in this work. The transport properties of ruthenium nanowires were examined, and the contribution of grain boundary scattering was found to dominate the overall resistivity. Such insights for other metals/materials could also be useful.

- In case of a via, the nanowire model proposed in this dissertation can be easily adapted by: (a) measuring the intercept length in the direction of the flow of the current, and (b) if the bulk resistivity is anisotropic, appropriate values must be used depending on the texture. For e.g., in case of ruthenium which is a hcp structure, the resistivity in the direction parallel to the hexagonal axis is 5.6 μΩcm [12], and 7.6 μΩcm perpendicular to the hexagonal axis. For random texture, 7.1 μΩcm should be used. Exact geometrical models of current density distributions in interconnects are clearly beyond the scope of the thesis and are very dependent on the design, the process technology, the overlay accuracy, and the line and via shape. However, these models will benefit clearly from the calibrated resistivity vs. area measurements obtained within the thesis.

Appendix A

Deposition and characterization techniques

All films studied in Chapter 4 were deposited by physical vapor deposition (PVD) at room temperature on Si (100). Prior to metal deposition, a 90 nm thick thermal oxide was grown on the silicon wafers to ensure electrical isolation. Copper, ruthenium, and iridium films were deposited on 300 mm wafers in a Canon Anelva EC7800 system. In addition to films directly deposited on SiO_2, copper and ruthenium films were also grown in situ on 1.5 nm thick PVD TaN and capped by 1.5 nm thick PVD TaN. This was done to prevent the oxidation of the copper surface, to avoid copper diffusion into the underlying SiO_2 during annealing, and to study the effect of the "*cladding*" material on the ruthenium thin film resistivity. Rhodium and platinum films were sputter deposited on small samples in a home build system. A thin (~1 nm) titanium layer was used to promote adhesion for platinum. Rhodium films were deposited on SiO_2. Palladium films were obtained by e-beam evaporation using a Pfeiffer PLS 580 system on a thin TiN adhesion layer.

The thin film resistivity was calculated from sheet resistance measurements using KLA Tencor RS100 and Jandel 4-point probe systems as well as the film thickness measured by X-Ray Reflectivity (XRR). XRR was performed using Cu Kα radiation in a Bede MetrixL diffractometer from Jordan Valley or a Panalytical X'Pert diffractometer. Film thicknesses by XRR were cross-calibrated by Rutherford backscattering spectrometry (RBS) measurements using a 1.52 MeV He^+ ion beam in a rotating random mode at a backscatter angle of 170°. The lower limit on the thickness was obtained from the atomic

density measured from the RBS (bulk metal density was assumed). The maximum uncertainty on the RBS measurements were <2%[38]. The upper limit on the thickness was taken from the XRR measurements (The maximum uncertain in XRR measurements was <0.5nm). The tools used to measure sheet resistance in this work are highly calibrated and statistical errors in the measurements can be neglected.

In all cases, the contribution of the adhesion layers to the sheet resistance was obtained by independent measurements and taken into account in the determination of the metal thin film resistivity. The diffractometers mentioned above were also used to assess the film crystallinity using x-ray diffraction (XRD).

The microstructure of the films was determined by plan-view transmission electron microscopy (TEM) images using Tecnai F30 and Titan3 G2 microscopes. Based on these images, the mean linear grain boundary intercept distance (the average linear distance between grain boundaries) was determined [77]. Surface roughnesses were measured by atomic force microscopy (AFM) using a Bruker IconPT microscope. Scan sizes were 5x5 μm. Lateral correlation lengths of the surface roughness were obtained from the autocorrelation function.

The RMS roughness (R_q) is defined as the standard deviation of the elevation, z values, within the given area, is calculated from the following equation where $z_{average}$ is the average of the z values within the given area, z_i is the z value for a given point, and N is the number of points within the given area.

[38]RBS measurements were performed at the MCA lab of imec. An uncertainty margin is provided that includes the statistical uncertainty and the intrinsic methodological uncertainties separately. The statistical uncertainty is a basic counting uncertainty. For 'n' counts, the uncertainty is square root of n. The methodological uncertainty attempts to include various sources of uncertainty, and includes - uncertainty in the high voltage, uncertainty in the scattering angle (detector location), uncertainty in the stopping power of He in Si, uncertainty in the fitting and related to this uncertainty in the energy calibration of the spectrometer. Their estimate of the error in the measurement, including the electronic stopping power, is <2% [248].

$$R_q = \sqrt{\sum_{i=1}^{N} \frac{\left(z_i - z_{average}\right)^2}{N}}$$

In an AFM topography image on a surface plane x-y for a given area, A, defined by a window scan size L, the height values can be associated with their respective surface coordinates and the image can be described by a matrix with N rows and M columns corresponding to the surface (x, y) points which contains the height as matrix elements. The autocorrelation function is then given by [249], [250]:

$$G(m,n) = \frac{1}{(N-n)(M-m)} \sum_{l=1}^{N-n} \sum_{k=1}^{M-m} z_{k+m,l+n}\, z_{k,l}$$

where, $\tau_x = x_1\text{-}x_2$, $\tau_y = y_1\text{-}y_2$, Δ is the sampling interval, $m = \tau_x/\Delta x$, $n = \tau_y/\Delta y$.

The one-dimensional autocorrelation function is then given by:

$$G_x(m) = \frac{1}{(N)(M-m)} \sum_{l=1}^{N} \sum_{k=1}^{M-m} z_{k+m,l}\, z_{k,l}$$

The correlation length, T, can be extracted by the following one-dimensional autocorrelation function.

$$G_x(\tau_x) = R_q^2 \exp(-\tau_x^2/T^2)$$

Appendix B

Recrystallization temperature of ALD Ru

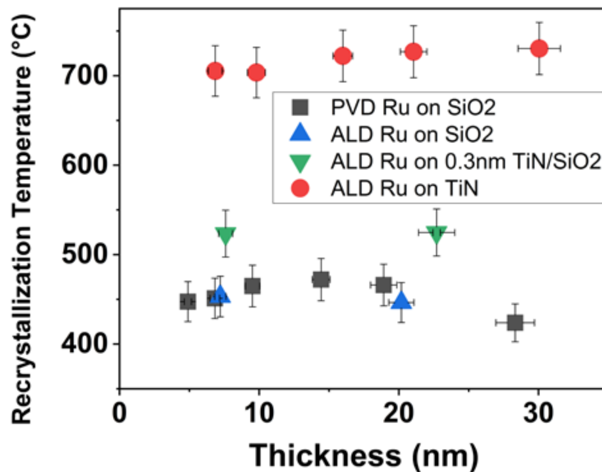

Figure B.1 The recrystallization temperature of ALD Ru films grown using the EBECH precursor on various substrates. From Figure 4.10 (that shows the Ti concentration inside Ru films on various substrates), a strong correlation between the Ti concentration and the recrystallization temperature can be observed. A comparison with PVD Ru is also shown.

Appendix C

Electrical cross-section area of nanowires

$$\mathbf{R = \rho.L/A}$$

$$\mathbf{dR/dT = (L/A).d\rho/dT}$$

(Here, we ignore the resistivity contributions due to the thermal expansion of the wires. Such contributions were found to be typically small, <0.6% for the Ru wires fabricated in this work). Dividing the wire into small resistive elements, the series resistance is given by:

$$R = \int_0^L \frac{\rho(l)}{A(l)} dl$$

$$\frac{dR}{dT} = \int_0^L \frac{d\rho(l)}{dT} \frac{1}{A(l)} dl$$

$$\frac{dR}{dT} = \frac{d\rho}{dT} \int_0^L \frac{1}{A(l)} dl$$

$$\frac{dR}{dT} = \frac{d\rho}{dT} \frac{L}{A_H}$$

where A_H is the harmonic mean. The harmonic mean is smaller than the arithmetic and geometric mean[39] and thus the electrical cross-section area calculated from the temperature-dependent resistance measurements apparently underestimate the physical area of very rough lines measured from the TEM images.

In the limiting case when the metal wire is open, then the area of one of the resistive elements becomes zero. Thus, the harmonic average becomes zero and so does the electrical area.

[39]For positive real numbers, arithmetic mean > geometric mean > harmonic mean.

Appendix D

Resistivity comparison of sub-100nm^2 nanowires

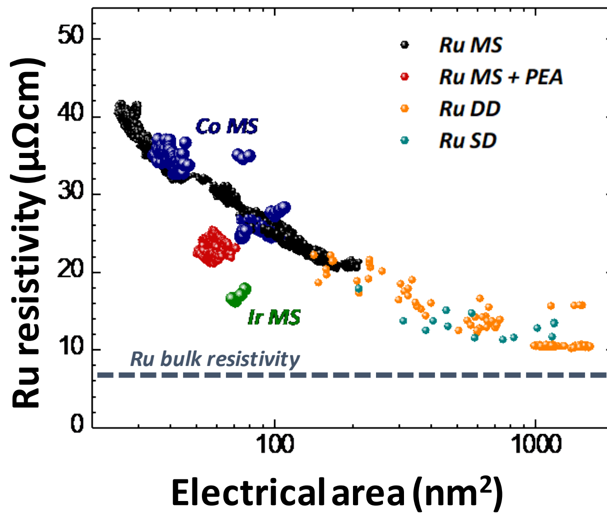

Figure D.1 Resistivity *vs.* electrical cross-sectional area for Ru interconnects obtained by different integration routes as indicated (MS: metal spacer [251]; PEA: post-etch anneal [252]; DD: dual damascene [240]; SD: single damascene [20]). Additional data for Co and Ir wires are also shown [252]. (All data shown here are generated during the course of this dissertation, except Ru SD and DD)

Bibliography

[1] K. Fuchs, "The conductivity of thin metallic films according to the electron theory of metals," *Mathematical Proceedings of the Cambridge Philosophical Society*, vol. 34, no. 01, pp. 100–108, Jan. 1938.

[2] E. H. Sondheimer, "The mean free path of electrons in metals," *Advances in Physics*, vol. 1, no. 1, pp. 1–42, 1952.

[3] X.-G. Zhang and W. H. Butler, "Conductivity of metallic films and multilayers," *Physical Review B*, vol. 51, no. 15, pp. 10085–10103, Apr. 1995.

[4] A. F. Mayadas, M. Shatzkes, and J. F. Janak, "Electrical Resistivity Model for Polycrystalline films: The Case of Specular Reflection at External Surfaces," *Applied Physics Letters*, vol. 14, no. 11, pp. 345–347, Jun. 1969.

[5] A. F. Mayadas and M. Shatzkes, "Electrical-resistivity model for polycrystalline films: the case of arbitrary reflection at external surfaces," *Physical review B*, vol. 1, no. 4, pp. 1382–1389, Feb. 1970.

[6] S. L. T. Jones *et al.*, "Electron transport properties of sub-3-nm diameter copper nanowires," *Physical Review B*, vol. 92, no. 11, p. 115413, Sep. 2015.

[7] A. E. Meyerovich and I. V. Ponomarev, "Surface roughness and size effects in quantized films," *Physical Review B*, vol. 65, no. 15, p. 155413, Mar. 2002.

[8] N. Trivedi and N. W. Ashcroft, "Quantum size effects in transport properties of metallic films," *Physical Review B*, vol. 38, no. 17, pp. 12298–12309, Dec. 1988.

[9] Z. Tešanović, M. V. Jarić, and S. Maekawa, "Quantum transport and surface scattering," *Physical review letters*, vol. 57, no. 21, pp. 2760–2763, Nov. 1986.

[10] R. C. Munoz and C. Arenas, "Size effects and charge transport in metals: Quantum theory of the resistivity of nanometric metallic structures arising from electron scattering by grain boundaries and by rough surfaces," *Applied Physics Reviews*, vol. 4, no. 1, p. 011102, Mar. 2017.

[11] P. Kapur, J. P. McVittie, and K. C. Saraswat, "Technology and reliability constrained future copper interconnects. I. Resistance modeling," *IEEE Transactions on Electron Devices*, vol. 49, no. 4, pp. 590–597, Apr. 2002.

[12] W. Steinhögl, G. Schindler, G. Steinlesberger, and M. Engelhardt, "Size-dependent resistivity of metallic wires in the mesoscopic range," *Physical Review B*, vol. 66, no. 7, Aug. 2002.

[13] S. M. Rossnagel and T. S. Kuan, "Alteration of Cu conductivity in the size effect regime," *Journal of Vacuum Science & Technology B: Microelectronics and Nanometer Structures*, vol. 22, no. 1, pp. 240–247, Jan. 2004.

[14] J. J. Plombon, E. Andideh, V. M. Dubin, and J. Maiz, "Influence of phonon, geometry, impurity, and grain size on Copper line resistivity," *Applied Physics Letters*, vol. 89, no. 11, p. 113124, Sep. 2006.

[15] S. Maîtrejean, R. Gers, T. Mourier, A. Toffoli, and G. Passemard, "Experimental measurements of electron scattering parameters in Cu narrow lines," *Microelectronic Engineering*, vol. 83, no. 11, pp. 2396–2401, Nov. 2006.

[16] F. Chen and D. Gardner, "Influence of line dimensions on the resistance of Cu interconnections," *IEEE Electron Device Letters*, vol. 19, no. 12, pp. 508–510, Dec. 1998.

[17] P. Kapur, G. Chandra, J. P. McVittie, and K. C. Saraswat, "Technology and reliability constrained future copper interconnects. II. Performance implications," *IEEE Transactions on Electron Devices*, vol. 49, no. 4, pp. 598–604, Apr. 2002.

[18] K. J. Kuhn, "Considerations for Ultimate CMOS Scaling," *IEEE Transactions on Electron Devices*, vol. 59, no. 7, pp. 1813–1828, Jul. 2012.

[19] A. Ceyhan and A. Naeemi, "Cu/Low-k Interconnect Technology Design and Benchmarking for Future Technology Nodes," *IEEE Transactions on Electron Devices*, vol. 60, no. 12, pp. 4041–4047, Dec. 2013.

[20] L. G. Wen *et al.*, "Atomic Layer Deposition of Ruthenium with TiN Interface for Sub-10 nm Advanced Interconnects beyond Copper," *ACS Applied Materials & Interfaces*, vol. 8, no. 39, pp. 26119–26125, Oct. 2016.

[21] W. Arden, "Future semiconductor material requirements and innovations as projected in the ITRS 2005 roadmap," *Materials Science and Engineering: B*, vol. 134, no. 2–3, pp. 104–108, Oct. 2006.

[22] G. E. Moore, "Cramming more components onto integrated circuits," *Electronics*, vol. 38, no. 8, pp. 114–117, Apr-1965.

[23] S. Borkar, "Design challenges of technology scaling," *IEEE micro*, vol. 19, no. 4, pp. 23–29, Aug. 1999.

[24] S. Thompson, "Mos scaling: Transistor challenges for the 21st century," *Intel Technology Journal*, May 1998.

[25] "International Roadmap for Devices and Systems, 2016 Edition, More Moore, White Paper," IEEE, More Moore, 2016.

[26] G. A. Brown, P. M. Zeitzoff, G. Bersuker, and H. R. Huff, "Scaling CMOS: materials & devices," *Materials today*, vol. 7, no. 1, pp. 20–25, Jan. 2004.

[27] Y. Shacham-Diamand, T. Osaka, M. Datta, and T. Ohba, Eds., *Advanced Nanoscale ULSI Interconnects: Fundamentals and Applications*. New York, NY: Springer New York, 2009.

[28] P. C. Andricacos, C. Uzoh, J. O. Dukovic, J. Horkans, and H. Deligianni, "Damascene copper electroplating for chip interconnections," *IBM Journal of Research and Development*, vol. 42, no. 5, pp. 567–574, Sep. 1998.

[29] R. Rosenberg, D. C. Edelstein, C.-K. Hu, and K. P. Rodbell, "Copper Metallization for High Performance Silicon Technology," *Annual Review of Materials Science*, vol. 30, no. 1, pp. 229–262, Aug. 2000.

[30] W. Volksen, R. D. Miller, and G. Dubois, "Low Dielectric Constant Materials," *Chemical Reviews*, vol. 110, no. 1, pp. 56–110, Jan. 2010.

[31] T. Angsten, T. Mayeshiba, H. Wu, and D. Morgan, "Elemental vacancy diffusion database from high-throughput first-principles calculations for fcc and hcp structures," *New Journal of Physics*, vol. 16, no. 1, p. 015018, Jan. 2014.

[32] B. Li, T. D. Sullivan, T. C. Lee, and D. Badami, "Reliability challenges for copper interconnects," *Microelectronics Reliability*, vol. 44, no. 3, pp. 365–380, Mar. 2004.

[33] T. Gupta, *Copper Interconnect Technology*. New York, NY: Springer New York, 2009.

[34] K. H. Brown, D. A. Grose, R. C. Lange, T. H. Ning, and P. A. Totta, "Advancing the state of the art in high-performance logic and array technology," *IBM Journal of Research and Development*, vol. 36, no. 5, pp. 821–828, Sep. 1992.

[35] M. Krishnan, J. W. Nalaskowski, and L. M. Cook, "Chemical Mechanical Planarization: Slurry Chemistry, Materials, and Mechanisms," *Chemical Reviews*, vol. 110, no. 1, pp. 178–204, Jan. 2010.

[36] H. Marom, J. Mullin, and M. Eizenberg, "Size-dependent resistivity of nanometric copper wires," *Physical Review B*, vol. 74, no. 4, p. 045411, Jul. 2006.

[37] J. M. Roberts, A. P. Kaushik, and J. S. Clarke, "Resistivity of sub-30 nm copper lines," in *2015 IEEE International Interconnect Technology Conference and 2015 IEEE Materials for Advanced Metallization Conference (IITC/MAM)*, 2015, pp. 341–344.

[38] J. R. Lloyd and J. J. Clement, "Electromigration in copper conductors," *Thin Solid Films*, vol. 262, no. 1–2, pp. 135–141, Jun. 1995.

[39] C.-K. Hu and J. M. E. Harper, "Copper interconnections and reliability," *Materials Chemistry and Physics*, vol. 52, no. 1, pp. 5–16, Jun. 1998.

[40] Y. Kitaoka, T. Tono, S. Yoshimoto, T. Hirahara, S. Hasegawa, and T. Ohba, "Direct detection of grain boundary scattering in damascene Cu wires by nanoscale four-point probe resistance measurements," *Applied Physics Letters*, vol. 95, no. 5, p. 052110, Aug. 2009.

[41] J.-W. Lim, K. Mimura, and M. Isshiki, "Thickness dependence of resistivity for Cu films deposited by ion beam deposition," *Applied Surface Science*, vol. 217, no. 1–4, pp. 95–99, Jul. 2003.

[42] J. S. Chawla, F. Gstrein, K. P. O'Brien, J. S. Clarke, and D. Gall, "Electron scattering at surfaces and grain boundaries in Cu thin films and wires," *Physical Review B*, vol. 84, no. 23, p. 235423, Dec. 2011.

[43] T. Sun *et al.*, "Dominant role of grain boundary scattering in the resistivity of nanometric Cu films," *Physical Review B*, vol. 79, no. 4, p. 041402, Jan. 2009.

[44] T. Sun *et al.*, "Surface and grain-boundary scattering in nanometric Cu films," *Physical Review B*, vol. 81, no. 15, p. 061503, Apr. 2010.

[45] W. Zhang *et al.*, "Influence of the electron mean free path on the resistivity of thin metal films," *Microelectronic Engineering*, vol. 76, no. 1–4, pp. 146–152, Oct. 2004.

[46] C. Pan and A. Naeemi, "A Proposal for a Novel Hybrid Interconnect Technology for the End of Roadmap," *IEEE Electron Device Letters*, vol. 35, no. 2, pp. 250–252, Feb. 2014.

[47] D. R. Frear, "Materials issues in area-array microelectronic packaging," *Journal of The Minerals, Metals & Materials Society*, vol. 51, no. 3, pp. 22–27, Mar. 1999.

[48] K. Sankaran, S. Clima, M. Mees, C. Adelmann, Z. Tökei, and G. Pourtois, "Exploring alternative metals to Cu and W for interconnects: An ab initio insight," in *IEEE International Interconnect Technology Conference*, 2014, pp. 193–196.

[49] K. Sankaran, S. Clima, M. Mees, and G. Pourtois, "Exploring Alternative Metals to Cu and W for Interconnects Applications Using Automated First-Principles Simulations," *ECS Journal of Solid State Science and Technology*, vol. 4, no. 1, pp. N3127–N3133, Jan. 2015.

[50] C. Adelmann *et al.*, "Alternative metals for advanced interconnects," in *IEEE International Interconnect Technology Conference*, 2014, pp. 173–176.

[51] D. Gall, "Electron mean free path in elemental metals," *Journal of Applied Physics*, vol. 119, no. 8, p. 085101, 2016.

[52] "Platinum Group Metals," *Chem230 Wiki*. [Online]. Available: http://chem230.wikia.com/wiki/Platinum_Group_Metals. [Accessed: 13-Apr-2017].

[53] D. Josell, S. H. Brongersma, and Z. Tőkei, "Size-Dependent Resistivity in Nanoscale Interconnects," *Annual Review of Materials Research*, vol. 39, no. 1, pp. 231–254, May 2009.

[54] J. S. Chawla and D. Gall, "Specular electron scattering at single-crystal Cu(001) surfaces," *Applied Physics Letters*, vol. 94, no. 25, p. 252101, Jun. 2009.

[55] R. L. Graham *et al.*, "Resistivity dominated by surface scattering in sub-50 nm Cu wires," *Applied Physics Letters*, vol. 96, no. 4, p. 042116, Jan. 2010.

[56] J. M. Camacho and A. I. Oliva, "Morphology and electrical resistivity of metallic nanostructures," *Microelectronics Journal*, vol. 36, no. 3–6, pp. 555–558, Mar. 2005.

[57] J. W. C. De Vries, "Temperature and thickness dependence of the resistivity of thin polycrystalline aluminium, cobalt, nickel, palladium, silver and gold films," *Thin Solid Films*, vol. 167, no. 1–2, pp. 25–32, 1988.

[58] M. Tay, K. Li, and Y. Wu, "Electrical transport properties of ultrathin metallic films," *Journal of Vacuum Science & Technology B: Microelectronics and Nanometer Structures*, vol. 23, no. 4, pp. 1412–1416, 2005.

[59] R. A. Brown, “A dislocation model of grain boundary electrical resistivity,” *Journal of Physics F: Metal Physics*, vol. 7, no. 8, pp. 1477–1488, 1977.

[60] T.-H. Kim *et al.*, “Large Discrete Resistance Jump at Grain Boundary in Copper Nanowire,” *Nano Letters*, vol. 10, no. 8, pp. 3096–3100, Aug. 2010.

[61] T. Nemoto, T. Fukino, S. Tsurekawa, X. Gu, A. Teramoto, and T. Ohmi, “In situ Observation of Grain Growth on Electroplated Cu Film by Electron Backscatter Diffraction,” *Japanese Journal of Applied Physics*, vol. 48, no. 6, p. 066507, Jun. 2009.

[62] P. Chaudhari, “Grain Growth and Stress Relief in Thin Films,” *Journal of Vacuum Science and Technology*, vol. 9, no. 1, pp. 520–522, Jan. 1972.

[63] J. M. E. Harper *et al.*, “Mechanisms for microstructure evolution in electroplated copper thin films near room temperature,” *Journal of Applied Physics*, vol. 86, no. 5, pp. 2516–2525, Sep. 1999.

[64] H. Lee, S. S. Wong, and S. D. Lopatin, “Correlation of stress and texture evolution during self- and thermal annealing of electroplated Cu films,” *Journal of Applied Physics*, vol. 93, no. 7, pp. 3796–3804, Apr. 2003.

[65] L. Vanasupa, Y.-C. Joo, P. R. Besser, and S. Pramanick, “Texture analysis of damascene-fabricated Cu lines by x-ray diffraction and electron backscatter diffraction and its impact on electromigration performance,” *Journal of Applied Physics*, vol. 85, no. 5, pp. 2583–2590, Mar. 1999.

[66] R. P. Vinci, E. M. Zielinski, and J. C. Bravman, “Thermal strain and stress in copper thin films,” *Thin solid films*, vol. 262, no. 1–2, pp. 142–153, 1995.

[67] S. B. Soffer, “Statistical Model for the Size Effect in Electrical Conduction,” *Journal of Applied Physics*, vol. 38, no. 4, pp. 1710–1715, Mar. 1967.

[68] K. Moors, “Electron transport and resistivity scaling in nanostructures,” PhD Thesis, Jan. 2017.

[69] B. Feldman, R. Deng, and S. T. Dunham, “Dependence of resistivity on surface profile in nanoscale metal films and wires,” *Journal of Applied Physics*, vol. 103, no. 11, p. 113715, Jun. 2008.

[70] F. Zahid, Y. Ke, D. Gall, and H. Guo, “Resistivity of thin Cu films coated with Ta, Ti, Ru, Al, and Pd barrier layers from first principles,” *Physical Review B*, vol. 81, no. 4, p. 045406, Jan. 2010.

[71] J. S. Chawla and D. Gall, "Specular electron scattering at single-crystal Cu(001) surfaces," *Applied Physics Letters*, vol. 94, no. 25, p. 252101, 2009.

[72] J. M. Ziman, *Electrons and Phonons: The Theory of Transport Phenomena in Solids*. Oxford, New York: Oxford University Press, 2001.

[73] S. Dutta *et al.*, "Thickness dependence of the resistivity of platinum-group metal thin films," *Journal of Applied Physics*, vol. 122, no. 2, p. 025107, Jul. 2017.

[74] H. J. Juretschke, "Electrical Conductivity of Thin Metallic Films with Unlike Surfaces," *Journal of Applied Physics*, vol. 37, no. 1, pp. 435–435, Jan. 1966.

[75] M. S. P. Lucas, "Electrical Conductivity of Thin Metallic Films with Unlike Surfaces," *Journal of Applied Physics*, vol. 36, no. 5, pp. 1632–1635, May 1965.

[76] R. Englman and E. H. Sondheimer, "The Electrical Conductivity of Anisotropic Thin Films," *Proceedings of the Physical Society. Section B*, vol. 69, no. 4, pp. 449–458, 1956.

[77] H. Abrams, "Grain size measurement by the intercept method," *Metallography*, vol. 4, no. 1, pp. 59–78, Feb. 1971.

[78] Y. F. Zhu, X. Y. Lang, W. T. Zheng, and Q. Jiang, "Electron Scattering and Electrical Conductance in Polycrystalline Metallic Films and Wires: Impact of Grain Boundary Scattering Related to Melting Point," *ACS Nano*, vol. 4, no. 7, pp. 3781–3788, Jul. 2010.

[79] R. A. Serway, J. W. Jewett, and V. Peroomian, *Physics for scientists and engineers with modern physics*, Ninth edition. Boston, MA: Brooks/Cole, Cengage Learning, 2014.

[80] S. K. Bandyopadhyay and A. K. Pal, "The effect of grain boundary scattering on the electron transport of aluminium films," *Journal of Physics D: Applied Physics*, vol. 12, no. 6, pp. 953–959, 1979.

[81] N. Artunç, M. D. Bilge, and G. Utlu, "The effects of grain boundary scattering on the electrical resistivity of single-layered silver and double-layered silver/chromium thin films," *Surface and Coatings Technology*, vol. 201, no. 19–20, pp. 8377–8381, Aug. 2007.

[82] J. W. C. De Vries, "Temperature and thickness dependence of the resistivity of thin polycrystalline aluminium, cobalt, nickel, palladium, silver and gold films," *Thin Solid Films*, vol. 167, no. 1–2, pp. 25–32, Dec. 1988.

[83] P. M. T. M. van Attekum, "Influence of grain boundaries and surface Debye temperature on the electrical resistance of thin gold films," *Physical Review B*, vol. 29, no. 2, pp. 645–650, 1984.

[84] G. Chen, P. Hui, K. Pita, P. Hing, and L. Kong, "Conductivity drop and crystallites redistribution in gold film," *Applied Physics A*, vol. 80, no. 3, pp. 659–665, Feb. 2005.

[85] J. W. C. De Vries, "Resistivity of thin Au films as a function of grain diameter and temperature," *Journal of Physics F: Metal Physics*, vol. 17, no. 9, pp. 1945–1952, 1987.

[86] K. Barmak *et al.*, "Surface and grain boundary scattering in nanometric Cu thin films: A quantitative analysis including twin boundaries," *Journal of Vacuum Science & Technology A: Vacuum, Surfaces, and Films*, vol. 32, no. 6, p. 061503, Nov. 2014.

[87] J.-W. Lim and M. Isshiki, "Electrical resistivity of Cu films deposited by ion beam deposition: Effects of grain size, impurities, and morphological defect," *Journal of Applied Physics*, vol. 99, no. 9, p. 094909, May 2006.

[88] G. Ramaswamy, A. K. Raychaudhuri, J. Goswami, and S. A. Shivashankar, "Large deviation from Matthiessen's rule in chemical vapour deposited copper films and its correlation with nanostructure," *Journal of Physics D: Applied Physics*, vol. 30, no. 5, pp. L5–L9, 1997.

[89] M. Fenn, G. Akuetey, and P. E. Donovan, "Electrical resistivity of Cu and Nb thin films," *Journal of Physics: Condensed Matter*, vol. 10, no. 8, pp. 1707–1720, 1998.

[90] A. Emre Yarimbiyik, H. A. Schafft, R. A. Allen, M. D. Vaudin, and M. E. Zaghloul, "Experimental and simulation studies of resistivity in nanoscale copper films," *Microelectronics Reliability*, vol. 49, no. 2, pp. 127–134, Feb. 2009.

[91] K. M. Mannan and K. R. Karim, "Grain boundary contribution to the electrical conductivity of polycrystalline Cu films," *Journal of Physics F: Metal Physics*, vol. 5, no. 9, pp. 1687–1693, 1975.

[92] W. Zhang *et al.*, "Surface and grain boundary scattering studied in beveled polycrystalline thin copper films," *Journal of Vacuum Science & Technology B: Microelectronics and Nanometer Structures*, vol. 22, no. 4, pp. 1830–1833, 2004.

[93] Y. P. Timalsina *et al.*, "Effects of nanoscale surface roughness on the resistivity of ultrathin epitaxial copper films," *Nanotechnology*, vol. 26, no. 7, p. 075704, Feb. 2015.

[94] Q. G. Zhang, B. Y. Cao, X. Zhang, M. Fujii, and K. Takahashi, "Size effects on the thermal conductivity of polycrystalline platinum nanofilms," *Journal of Physics: Condensed Matter*, vol. 18, no. 34, pp. 7937–7950, Aug. 2006.

[95] Q. G. Zhang, X. Zhang, B. Y. Cao, M. Fujii, K. Takahashi, and T. Ikuta, "Influence of grain boundary scattering on the electrical properties of platinum nanofilms," *Applied Physics Letters*, vol. 89, no. 11, p. 114102, 2006.

[96] Q. Jiang and H. M. Lu, "Size dependent interface energy and its applications," *Surface Science Reports*, vol. 63, no. 10, pp. 427–464, Oct. 2008.

[97] K. Moors, B. Sorée, Z. Tőkei, and W. Magnus, "Electron relaxation times and resistivity in metallic nanowires due to tilted grain boundary planes," in *EUROSOI-ULIS 2015: 2015 Joint International EUROSOI Workshop and International Conference on Ultimate Integration on Silicon*, 2015, pp. 201–204.

[98] N. A. Lanzillo, "Ab Initio evaluation of electron transport properties of Pt, Rh, Ir, and Pd nanowires for advanced interconnect applications," *Journal of Applied Physics*, vol. 121, no. 17, p. 175104, May 2017.

[99] C. Durkan and M. E. Welland, "Size effects in the electrical resistivity of polycrystalline nanowires," *Physical review B*, vol. 61, no. 20, p. 14215, 2000.

[100] D. Gall, "Electron mean free path in elemental metals," *Journal of Applied Physics*, vol. 119, no. 8, p. 085101, Feb. 2016.

[101] E. M. Savitskij, P. V. Gel'd, and V. P. Polyakova, "Kinetic and thermal properties of poly- and monocrystalline ruthenium at high temperatures," *Doklady Akademii Nauk SSSR*, vol. 229, no. 4, pp. 841–844, 1976.

[102] N. V. Volkenshtejn, V. E. Startsev, V. I. Cherepanov, V. M. Azhazha, G. P. Kovtun, and V. A. Elenskij, "Electric resistance anisotropy of ruthenium and rhenium single crystals at 2-300 K," *Fizika Metallov i Metallovedenie*, vol. 45, no. 6, pp. 1187–1199, 1978.

[103] T. Ando, A. B. Fowler, and F. Stern, "Electronic properties of two-dimensional systems," *Rev. Mod. Phys.*, vol. 54, no. 2, pp. 437–672, Apr. 1982.

[104] M. De Clercq *et al.*, "Resistivity scaling model for metals with conduction band anisotropy," *Phys. Rev. Materials*, vol. 2, no. 3, p. 033801, Mar. 2018.

[105] "Personal communication with Kristof Moors."

[106] "Personal communication with Kiroubanand Sankaran."

[107] Y. Zhou, S. Sreekala, P. M. Ajayan, and S. K. Nayak, "Resistance of copper nanowires and comparison with carbon nanotube bundles for interconnect applications using first principles calculations," *Journal of Physics: Condensed Matter*, vol. 20, no. 9, p. 095209, Mar. 2008.

[108] O. V. Pedreira *et al.*, "Reliability study on cobalt and ruthenium as alternative metals for advanced interconnects," in *2017 IEEE International Reliability Physics Symposium (IRPS)*, 2017, pp. 6B-2.1-6B–2.8.

[109] F. W. Mont *et al.*, "Cobalt interconnect on same copper barrier process integration at the 7nm node," in *2017 IEEE International Interconnect Technology Conference (IITC)*, 2017, pp. 1–3.

[110] N. Bekiaris *et al.*, "Cobalt fill for advanced interconnects," in *2017 IEEE International Interconnect Technology Conference (IITC)*, 2017, pp. 1–3.

[111] V. Kamineni *et al.*, "Tungsten and cobalt metallization: A material study for MOL local interconnects," in *2016 IEEE International Interconnect Technology Conference / Advanced Metallization Conference (IITC/AMC)*, 2016, pp. 105–107.

[112] C. K. Hu *et al.*, "Electromigration and resistivity in on-chip Cu, Co and Ru damascene nanowires," in *2017 IEEE International Interconnect Technology Conference (IITC)*, 2017, pp. 1–3.

[113] K. L. Lin *et al.*, "Nickel silicide for interconnects," in *2015 IEEE International Interconnect Technology Conference and 2015 IEEE Materials for Advanced Metallization Conference (IITC/MAM)*, 2015, pp. 169–172.

[114] S. Linderoth, P. V. Hendriksen, M. Mogensen, and N. Langvad, "Investigations of metallic alloys for use as interconnects in solid oxide fuel cell stacks," *Journal of materials science*, vol. 31, no. 19, pp. 5077–5082, 1996.

[115] G. Braeckelmann, R. Venkatraman, C. Capasso, and M. Herrick, "Integration and reliability of copper magnesium alloys for multilevel interconnects," in *Proceedings of the IEEE 2000 International Interconnect Technology Conference (Cat. No.00EX407)*, 2000, pp. 236–238.

[116] C.-K. Hu and B. Luther, "Electromigration in two-level interconnects of Cu and Al alloys," *Materials Chemistry and Physics*, vol. 41, no. 1, pp. 1–7, 1995.

[117] M. Han, S. Peng, Z. Wang, Z. Yang, and X. Chen, "Properties of Fe–Cr based alloys as interconnects in a solid oxide fuel cell," *Journal of Power Sources*, vol. 164, no. 1, pp. 278–283, Jan. 2007.

[118] A. P. Peter *et al.*, “Selective chemical vapor synthesis of Cu3Ge: Process optimization and film properties,” *Intermetallics*, vol. 34, pp. 35–42, Mar. 2013.

[119] L. Dong *et al.*, “Dielectrophoretically controlled fabrication of single-crystal nickel silicide nanowire interconnects,” *Nano Letters*, vol. 5, no. 10, pp. 2112–2115, 2005.

[120] Y.-L. Chueh, M.-T. Ko, L.-J. Chou, L.-J. Chen, C.-S. Wu, and C.-D. Chen, “TaSi2 Nanowires: A Potential Field Emitter and Interconnect,” *Nano Letters*, vol. 6, no. 8, pp. 1637–1644, Aug. 2006.

[121] M. H. Lin and A. S. Oates, “Electromigration in Dual-Damascene CuMn Alloy IC Interconnects,” *IEEE Transactions on Device and Materials Reliability*, vol. 13, no. 1, pp. 330–332, Mar. 2013.

[122] M. Ronay, “Self-encapsulated silver alloys for interconnects,” US7527188 B2, 05-May-2009.

[123] C.-C. Wei, “Titanium silicide local interconnect process,” US5173450 A, 22-Dec-1992.

[124] R. Schinella and W. Herndon, “Methods for forming metal/metal silicide semiconductor device interconnect system,” US3777364 A, 11-Dec-1973.

[125] A. Naeemi and J. D. Meindl, “Carbon Nanotube Interconnects,” *Annual Review of Materials Research*, vol. 39, no. 1, pp. 255–275, 2009.

[126] F. Kreupl *et al.*, “Carbon nanotubes in interconnect applications,” *Microelectronic Engineering*, vol. 64, no. 1, pp. 399–408, 2002.

[127] X. Chen *et al.*, “Fully Integrated Graphene and Carbon Nanotube Interconnects for Gigahertz High-Speed CMOS Electronics,” *IEEE Transactions on Electron Devices*, vol. 57, no. 11, pp. 3137–3143, Nov. 2010.

[128] A. Todri-Sanial, J. Dijon, and A. Maffucci, Eds., *Carbon Nanotubes for Interconnects*. Cham: Springer International Publishing, 2017.

[129] Q. Shao, G. Liu, D. Teweldebrhan, and A. A. Balandin, “High-temperature quenching of electrical resistance in graphene interconnects,” *Applied Physics Letters*, vol. 92, no. 20, p. 202108, May 2008.

[130] R.-H. Kim *et al.*, “Stretchable, Transparent Graphene Interconnects for Arrays of Microscale Inorganic Light Emitting Diodes on Rubber Substrates,” *Nano Letters*, vol. 11, no. 9, pp. 3881–3886, Sep. 2011.

[131] D. A. B. Miller, "Rationale and challenges for optical interconnects to electronic chips," *Proceedings of the IEEE*, vol. 88, no. 6, pp. 728–749, Jun. 2000.

[132] J. S. Levy, A. Gondarenko, M. A. Foster, A. C. Turner-Foster, A. L. Gaeta, and M. Lipson, "CMOS-compatible multiple-wavelength oscillator for on-chip optical interconnects," *Nature Photonics*, vol. 4, no. 1, pp. 37–40, Jan. 2010.

[133] D. A. B. Miller, "Device Requirements for Optical Interconnects to Silicon Chips," *Proceedings of the IEEE*, vol. 97, no. 7, pp. 1166–1185, Jul. 2009.

[134] "Ruthenium Price History." [Online]. Available: https://www.quandl.com. [Accessed: 31-Aug-2017].

[135] F. J. Humphreys, "A new analysis of recovery, recrystallisation, and grain growth," *Materials Science and Technology*, vol. 15, no. 1, pp. 37–44, Jan. 1999.

[136] W. D. Callister, *Materials science and engineering: an introduction*, 7th ed. New York: John Wiley & Sons, 2007.

[137] J. E. Burke and D. Turnbull, "Recrystallization and grain growth," *Progress in Metal Physics*, vol. 3, pp. 220–292, Jan. 1952.

[138] R. D. Doherty *et al.*, "Current issues in recrystallization: A review," *Materials Today*, vol. 1, no. 2, pp. 219–274, 1998.

[139] F. C. Campbell, *Elements of Metallurgy and Engineering Alloys*. Materials Park, Ohio: ASM International, 2008.

[140] F. J. Humphreys and M. Hatherly, *Recrystallization and related annealing phenomena*, 1st ed. Oxford, OX, UK ; Tarrytown, N.Y., U.S.A: Pergamon, 1995.

[141] K. Lucke and K. Detert, "A quantitative theory of grain-boundary motion and recrystallization in the presence of impurities - ScienceDirect," *Acta Metallurgica*, vol. 5, no. 11, pp. 628–637, Nov. 1957.

[142] R. D. Doherty, "Recrystallization and texture," *Progress in Materials Science*, vol. 42, no. 1, pp. 39–58, Jan. 1997.

[143] J. A. Thornton, "Influence of substrate temperature and deposition rate on structure of thick sputtered Cu coatings," *Journal of Vacuum Science and Technology*, vol. 12, no. 4, pp. 830–835, Jul. 1975.

[144] X. Yu, J. Rong, Z. Zhan, Z. Liu, and J. Liu, "Effects of grain size and thermodynamic energy on the lattice parameters of metallic nanomaterials," *Materials & Design*, vol. 83, no. Supplement C, pp. 159–163, Oct. 2015.

[145] H. Z. Yu and C. V. Thompson, "Grain growth and complex stress evolution during Volmer–Weber growth of polycrystalline thin films," *Acta Materialia*, vol. 67, no. Supplement C, pp. 189–198, Apr. 2014.

[146] R. Koch, "Stress in Evaporated and Sputtered Thin Films – A Comparison," *Surface and Coatings Technology*, vol. 204, no. 12, pp. 1973–1982, Mar. 2010.

[147] C. V. Thompson and R. Carel, "Stress and grain growth in thin films," *Journal of the Mechanics and Physics of Solids*, vol. 44, no. 5, pp. 657–673, 1996.

[148] R. Methaapanon, S. M. Geyer, S. Brennan, and S. F. Bent, "Size Dependent Effects in Nucleation of Ru and Ru Oxide Thin Films by Atomic Layer Deposition Measured by Synchrotron Radiation X-ray Diffraction," *Chem. Mater.*, vol. 25, no. 17, pp. 3458–3463, Sep. 2013.

[149] P. Scherrer, "Bestimmung der Größe und der inneren Struktur von Kolloidteilchen mittels Röntgenstrahlen," *Nachrichten von der Gesellschaft der Wissenschaften zu Göttingen, Mathematisch-Physikalische Klasse*, vol. 1918, pp. 98–100, 1918.

[150] R. Carel, "Grain Growth and Texure Evolution in Thin Films," PhD Thesis, Massachusetts Institute of Technology, 1995.

[151] E. Chason, "A kinetic analysis of residual stress evolution in polycrystalline thin films," *Thin Solid Films*, vol. 526, no. Supplement C, pp. 1–14, Dec. 2012.

[152] E. Chason and P. R. Guduru, "Tutorial: Understanding residual stress in polycrystalline thin films through real-time measurements and physical models," *Journal of Applied Physics*, vol. 119, no. 19, p. 191101, May 2016.

[153] D. Magnfält, A. Fillon, R. D. Boyd, U. Helmersson, K. Sarakinos, and G. Abadias, "Compressive intrinsic stress originates in the grain boundaries of dense refractory polycrystalline thin films," *Journal of Applied Physics*, vol. 119, no. 5, p. 055305, Feb. 2016.

[154] E. Chason, J. W. Shin, S. J. Hearne, and L. B. Freund, "Kinetic model for dependence of thin film stress on growth rate, temperature, and microstructure," *Journal of Applied Physics*, vol. 111, no. 8, p. 083520, Apr. 2012.

[155] D. Magnfält, Linköpings universitet, and kemi och biologi Institutionen för fysik, "Fundamental processes in thin film growth: the origin of compressive stress and the dynamics of the early growth stages," Department of Physics, Chemistry and Biology (IFM), Linköping University, Linköping, 2014.

[156] E. Le Bourhis, "Appendix 12: X-Ray Diffraction Analysis of Thin-Film Residual Stresses," in *Glass*, Wiley-VCH Verlag GmbH & Co. KGaA, 2007, pp. 335–339.

[157] F. M. d'Heurle, "Aluminum films deposited by rf sputtering," *Metallurgical and Materials Transactions B*, vol. 1, no. 3, pp. 725–732, 1970.

[158] P. Yan, E. Spiller, and P. Mirkarimi, "Characterization of ruthenium thin films as capping layer for extreme ultraviolet lithography mask blanks," *Journal of Vacuum Science & Technology B: Microelectronics and Nanometer Structures*, vol. 25, no. 6, pp. 1859–1866, 2007.

[159] T. Hur'yeva, M. Lisker, and E. P. Burte, "Ruthenium Films Deposited by Liquid-Delivery MOCVD Using Bis(ethylcyclopentadienyl)ruthenium with Toluene as the Solvent," *Chem. Vap. Deposition*, vol. 12, no. 7, pp. 429–434, Jul. 2006.

[160] M. Ohring, *The Materials Science of Thin Films*. Academic Press, 1992.

[161] Rui Huang, W. Robl, H. Ceric, T. Detzel, and G. Dehm, "Stress, Sheet Resistance, and Microstructure Evolution of Electroplated Cu Films During Self-Annealing," *IEEE Transactions on Device and Materials Reliability*, vol. 10, no. 1, pp. 47–54, Mar. 2010.

[162] M. Zacharias, J. Bläsing, P. Veit, L. Tsybeskov, K. Hirschman, and P. M. Fauchet, "Thermal crystallization of amorphous Si/SiO2 superlattices," *Applied Physics Letters*, vol. 74, no. 18, pp. 2614–2616, May 1999.

[163] M. Zacharias and P. Streitenberger, "Crystallization of amorphous superlattices in the limit of ultrathin films with oxide interfaces," *Physical Review B*, vol. 62, no. 12, pp. 8391–8396, 2000.

[164] X. Nie, F. Ma, D. Ma, and K. Xu, "Thermodynamics and kinetic behaviors of thickness-dependent crystallization in high-k thin films deposited by atomic layer deposition," *Journal of Vacuum Science & Technology A: Vacuum, Surfaces, and Films*, vol. 33, no. 1, p. 01A140, Jan. 2015.

[165] D. Biswas, M. N. Singh, A. K. Sinha, S. Bhattacharyya, and S. Chakraborty, "Effect of excess hafnium on HfO2 crystallization temperature and leakage current behavior of HfO2/Si metal-oxide-semiconductor devices," *Journal of Vacuum Science & Technology B, Nanotechnology and Microelectronics: Materials, Processing, Measurement, and Phenomena*, vol. 34, no. 2, p. 022201, Feb. 2016.

[166] V. Miikkulainen, M. Leskelä, M. Ritala, and R. L. Puurunen, "Crystallinity of inorganic films grown by atomic layer deposition: Overview and general trends," *Journal of Applied Physics*, vol. 113, no. 2, p. 021301, Jan. 2013.

[167] R. E. Reed-Hill, *Physical metallurgy principles*, 2nd ed. New York : Van Nostrand, 1972.

[168] R. Behrisch and K. Wittmaack, Eds., *Sputtering by Particle Bombardment III: Characteristics of Sputtered Particles, Technical Applications*. Berlin Heidelberg: Springer-Verlag, 1991.

[169] Y. Zhang, J. R. G. Evans, and S. Yang, "Corrected Values for Boiling Points and Enthalpies of Vaporization of Elements in Handbooks," *J. Chem. Eng. Data*, vol. 56, no. 2, pp. 328–337, Feb. 2011.

[170] J.-H. Joo *et al.*, "Investigation of Ruthenium Electrodes for (Ba,Sr)TiO3 Thin Films," *Japanese Journal of Applied Physics*, vol. 37, no. 6R, pp. 3396–3401, Jun. 1998.

[171] R. W. Siegel, "Positron Annihilation Spectroscopy," *Annual Review of Materials Science*, vol. 10, no. 1, pp. 393–425, 1980.

[172] B. P. Uberuaga, L. J. Vernon, E. Martinez, and A. F. Voter, "The relationship between grain boundary structure, defect mobility, and grain boundary sink efficiency," *Scientific Reports*, vol. 5, p. 9095, Mar. 2015.

[173] M. A. Tschopp, K. N. Solanki, F. Gao, X. Sun, M. A. Khaleel, and M. F. Horstemeyer, "Probing grain boundary sink strength at the nanoscale: Energetics and length scales of vacancy and interstitial absorption by grain boundaries in a-Fe," *Phys. Rev. B*, vol. 85, no. 6, p. 064108, Feb. 2012.

[174] M. Nomura and J. B. Adams, "Self-diffusion along twist grain boundaries in Cu," *Journal of Materials Research*, vol. 7, no. 12, pp. 3202–3212, Dec. 1992.

[175] M. Nomura and J. B. Adams, "Interstitial diffusion along twist grain boundaries in Cu," *Journal of Materials Research*, vol. 10, no. 11, pp. 2916–2924, Nov. 1995.

[176] M. R. Sørensen, Y. Mishin, and A. F. Voter, "Diffusion mechanisms in Cu grain boundaries," *Physical Review B*, vol. 62, no. 6, pp. 3658–3673, Aug. 2000.

[177] T. Frolov, D. L. Olmsted, M. Asta, and Y. Mishin, "Structural phase transformations in metallic grain boundaries," *Nature Communications*, vol. 4, p. 1899, May 2013.

[178] A. Uedono, T. Suzuki, and T. Nakamura, "Vacancy-type defects in electroplated Cu films probed by using a monoenergetic positron beam," *Journal of Applied Physics*, vol. 95, no. 3, pp. 913–918, Feb. 2004.

[179] A. Russell and K. L. Lee, *Structure-Property Relations in Nonferrous Metals*. John Wiley & Sons, 2005.

[180] V. Sorkin and Y. W. Zhang, "Mechanical properties and failure behavior of phosphorene with grain boundaries," *Nanotechnology*, vol. 28, no. 7, p. 075704, Feb. 2017.

[181] P. J. Roussel *et al.*, "Semi-empirical interconnect resistance model for advanced technology nodes: A model apt for materials selection based upon test line resistance measurements," in *2016 IEEE International Reliability Physics Symposium (IRPS)*, 2016, p. IT-2-1-IT-2-5.

[182] P. Kapur, J. P. McVittie, and K. C. Saraswat, "Technology and reliability constrained future copper interconnects. I. Resistance modeling," *IEEE Transactions on Electron Devices*, vol. 49, no. 4, pp. 590–597, Apr. 2002.

[183] G. Hegde, R. C. Bowen, and M. S. Rodder, "Lower limits of line resistance in nanocrystalline back end of line Cu interconnects," *Applied Physics Letters*, vol. 109, no. 19, p. 193106, Nov. 2016.

[184] G. Hegde, M. Povolotskyi, T. Kubis, J. Charles, and G. Klimeck, "An environment-dependent semi-empirical tight binding model suitable for electron transport in bulk metals, metal alloys, metallic interfaces, and metallic nanostructures. II. Application—Effect of quantum confinement and homogeneous strain on Cu conductance," *Journal of Applied Physics*, vol. 115, no. 12, p. 123704, Mar. 2014.

[185] K. Moors, B. Sorée, Z. Tőkei, and W. Magnus, "Resistivity scaling and electron relaxation times in metallic nanowires," *Journal of Applied Physics*, vol. 116, no. 6, p. 063714, Aug. 2014.

[186] K. Moors, B. Sorée, and W. Magnus, "Modeling surface roughness scattering in metallic nanowires," *Journal of Applied Physics*, vol. 118, no. 12, p. 124307, Sep. 2015.

[187] H. Marom, M. Ritterband, and M. Eizenberg, "The contribution of grain boundary scattering versus surface scattering to the resistivity of thin polycrystalline films," *Thin Solid Films*, vol. 510, no. 1–2, pp. 62–67, Jul. 2006.

[188] J. E. Sanchez and E. Arzt, "On the pinning of grain boundary motion by surface grooves," *Scripta Metallurgica et Materialia*, vol. 26, no. 9, pp. 1325–1330, May 1992.

[189] I. Petrov, P. B. Barna, L. Hultman, and J. E. Greene, "Microstructural evolution during film growth," *Journal of Vacuum Science & Technology A: Vacuum, Surfaces, and Films*, vol. 21, no. 5, pp. S117–S128, Sep. 2003.

[190] M. César, D. Liu, D. Gall, and H. Guo, "Calculated Resistances of Single Grain Boundaries in Copper," *Phys. Rev. Applied*, vol. 2, no. 4, p. 044007, Oct. 2014.

[191] "Structural Dependence of Grain Boundary Resistivity in Copper Nanowires," *Jpn. J. Appl. Phys.*, vol. 50, no. 8S3, p. 08LB09, Aug. 2011.

[192] L. Lu, Y. Shen, X. Chen, L. Qian, and K. Lu, "Ultrahigh Strength and High Electrical Conductivity in Copper," *Science*, vol. 304, no. 5669, pp. 422–426, Apr. 2004.

[193] R. Henriquez *et al.*, "Electron grain boundary scattering and the resistivity of nanometric metallic structures," *Physical Review B*, vol. 82, no. 11, p. 113409, Sep. 2010.

[194] J. M. Rickman and K. Barmak, "Resistivity in rough metallic thin films: A Monte Carlo study," *Journal of Applied Physics*, vol. 112, no. 1, p. 013704, Jul. 2012.

[195] J. S. Chawla, F. Zahid, H. Guo, and D. Gall, "Effect of O2 adsorption on electron scattering at Cu(001) surfaces," *Applied Physics Letters*, vol. 97, no. 13, p. 132106, Sep. 2010.

[196] W. Wu, S. H. Brongersma, M. Van Hove, and K. Maex, "Influence of surface and grain-boundary scattering on the resistivity of copper in reduced dimensions," *Applied Physics Letters*, vol. 84, no. 15, pp. 2838–2840, Apr. 2004.

[197] M. Leskelä and M. Ritala, "Atomic Layer Deposition Chemistry: Recent Developments and Future Challenges," *Angewandte Chemie International Edition*, vol. 42, no. 45, pp. 5548–5554, Nov. 2003.

[198] S. K. Kim, J. H. Han, G. H. Kim, and C. S. Hwang, "Investigation on the Growth Initiation of Ru Thin Films by Atomic Layer Deposition," *Chem. Mater.*, vol. 22, no. 9, pp. 2850–2856, May 2010.

[199] S.-S. Yim, D.-J. Lee, K.-S. Kim, S.-H. Kim, T.-S. Yoon, and K.-B. Kim, "Nucleation kinetics of Ru on silicon oxide and silicon nitride surfaces deposited by atomic layer deposition," *Journal of Applied Physics*, vol. 103, no. 11, p. 113509, Jun. 2008.

[200] K. J. Park, D. B. Terry, S. M. Stewart, and G. N. Parsons, "In Situ Auger Electron Spectroscopy Study of Atomic Layer Deposition: Growth Initiation and Interface Formation Reactions during Ruthenium ALD on Si−H, SiO_2, and HfO_2 Surfaces," *Langmuir*, vol. 23, no. 11, pp. 6106–6112, May 2007.

[201] J. Hämäläinen, M. Ritala, and M. Leskelä, "Atomic Layer Deposition of Noble Metals and Their Oxides," *Chemistry of Materials*, vol. 26, no. 1, pp. 786–801, Jan. 2014.

[202] T. Aaltonen, P. Alén, M. Ritala, and M. Leskelä, "Ruthenium thin films grown by atomic layer deposition," *Chemical Vapor Deposition*, vol. 9, no. 1, pp. 45–49, 2003.

[203] A. Schneider *et al.*, "Minimizing the Carbon Content of Thin Ruthenium Films by MOCVD Precursor Complex Design and Process Control," *Chemical Vapor Deposition*, vol. 13, no. 8, pp. 389–395, Aug. 2007.

[204] T.-K. Eom *et al.*, "Low Temperature Atomic Layer Deposition of Ruthenium Thin Films Using Isopropylmethylbenzene-Cyclohexadiene-Ruthenium and O[sub 2]," *Electrochemical and Solid-State Letters*, vol. 12, no. 11, pp. D85–D88, 2009.

[205] M. Popovici *et al.*, "Atomic Layer Deposition of Ruthenium Thin Films from (Ethylbenzyl) (1-Ethyl-1,4-cyclohexadienyl) Ru: Process Characteristics, Surface Chemistry, and Film Properties," *Chemistry of Materials*, vol. 29, no. 11, pp. 4654–4666, Jun. 2017.

[206] C.-K. Hu *et al.*, "Microstructure, impurity and metal cap effects on Cu electromigration," 2014, pp. 67–78.

[207] K. Masuda-Jindo, "Impurity segregation at grain boundaries in metals: Effects of applied stress," *Materials Letters*, vol. 3, no. 4, pp. 151–156, 1985.

[208] S. Hu, J. Nozawa, H. Koizumi, K. Fujiwara, and S. Uda, "Grain Boundary Segregation of Impurities During Polycrystalline Colloidal Crystallization," *Crystal Growth & Design*, vol. 15, no. 12, pp. 5685–5692, Dec. 2015.

[209] D. Avau, W. Vandervorst, and H. E. Maes, "Transient effects during SIMS depth profiling with oxygen," *Surf. Interface Anal.*, vol. 11, no. 10, pp. 522–528, Jul. 1988.

[210] M. I. Mendelev and D. J. Srolovitz, "Impurity effects on grain boundary migration," *Modelling Simul. Mater. Sci. Eng.*, vol. 10, no. 6, p. R79, 2002.

[211] M. César, D. Gall, and H. Guo, "Reducing Grain-Boundary Resistivity of Copper Nanowires by Doping," *Physical Review Applied*, vol. 5, no. 5, p. 054018, May 2016.

[212] A. Pyzyna *et al.*, “Resistivity of copper interconnects at 28 nm pitch and copper cross-sectional area below 100 nm2,” in *2017 IEEE International Interconnect Technology Conference (IITC)*, 2017, pp. 1–3.

[213] T.-R. Yew, M.-C. Liu, W. Lur, and S.-W. Sun, “Dual damascene process,” US5801094 A, 01-Sep-1998.

[214] J. S. Chawla *et al.*, “Resistance and electromigration performance of 6 nm wires,” in *2016 IEEE International Interconnect Technology Conference / Advanced Metallization Conference (IITC/AMC)*, 2016, pp. 63–65.

[215] X. Zhang *et al.*, “Ruthenium interconnect resistivity and reliability at 48 nm pitch,” in *2016 IEEE International Interconnect Technology Conference / Advanced Metallization Conference (IITC/AMC)*, 2016, pp. 31–33.

[216] M. Maenhoudt, J. Versluijs, H. Struyf, J. V. Olmen, and M. V. Hove, “Double patterning scheme for sub-0.25 k1 single damascene structures at NA=0.75, λ=193nm,” presented at the Optical Microlithography XVIII, 2004, vol. 5754, pp. 1508–1519.

[217] T. Furukawa, M. C. Hakey, S. J. Holmes, D. V. Horak, C. W. K. III, and P. H. Mitchell, “Method for forming quadruple density sidewall image transfer (SIT) structures,” US6875703 B1, 05-Apr-2005.

[218] H. Duan, D. Winston, J. K. W. Yang, B. M. Cord, V. R. Manfrinato, and K. K. Berggren, “Sub-10-nm half-pitch electron-beam lithography by using poly(methyl methacrylate) as a negative resist,” *Journal of Vacuum Science & Technology B, Nanotechnology and Microelectronics: Materials, Processing, Measurement, and Phenomena*, vol. 28, no. 6, p. C6C58-C6C62, Nov. 2010.

[219] W. Chao, J. Kim, E. H. Anderson, P. Fischer, S. Rekawa, and D. T. Attwood, “Double patterning HSQ processes of zone plates for 10 nm diffraction limitedperformance,” Ernest Orlando Lawrence Berkeley National Laboratory, Berkeley, CA (US), 2009.

[220] D. C. Flanders and A. E. White, “Application of ≅100 Å linewidth structures fabricated by shadowing techniques,” *Journal of Vacuum Science and Technology*, vol. 19, no. 4, pp. 892–896, Nov. 1981.

[221] N. Giordano, “Experimental study of localization in thin wires,” *Physical Review B*, vol. 22, no. 12, pp. 5635–5654, 1980.

[222] A. J. M. Mackus, S. A. F. Dielissen, J. J. L. Mulders, and W. M. M. Kessels, “Nanopatterning by direct-write atomic layer deposition,” *Nanoscale*, vol. 4, no. 15, pp. 4477–4480, 2012.

[223] S. Kodambaka, J. Tersoff, M. C. Reuter, and F. M. Ross, "Diameter-Independent Kinetics in the Vapor-Liquid-Solid Growth of Si Nanowires," *Physical Review Letters*, vol. 96, no. 9, p. 096105, Mar. 2006.

[224] C.-J. Kim *et al.*, "Spontaneous Chemical Vapor Growth of NiSi Nanowires and Their Metallic Properties," *Advanced Materials*, vol. 19, no. 21, pp. 3637–3642, Nov. 2007.

[225] E. K. Lee, B. L. Choi, Y. D. Park, Y. Kuk, S. Y. Kwon, and H. J. Kim, "Device fabrication with solid–liquid–solid grown silicon nanowires," *Nanotechnology*, vol. 19, no. 18, p. 185701, May 2008.

[226] J. Swerts, S. V. Elshocht, and A. Delabie, "Method for Selectively Depositing Noble Metals on Metal/Metal Nitride Substrates," US20130084700 A1, 04-Apr-2013.

[227] W.-H. Kim, S.-J. Park, J.-Y. Son, and H. Kim, "Ru nanostructure fabrication using an anodic aluminum oxide nanotemplate and highly conformal Ru atomic layer deposition," *Nanotechnology*, vol. 19, no. 4, p. 045302, Jan. 2008.

[228] L. G. Wen *et al.*, "Ruthenium metallization for advanced interconnects," in *2016 IEEE International Interconnect Technology Conference / Advanced Metallization Conference (IITC/AMC)*, 2016, pp. 34–36.

[229] H. Li, S. Jin, J. Proost, M. Van Hove, L. Froyen, and K. Maex, "A new approach for the measurement of resistivity and cross-sectional area of an aluminium interconnect line: principle and applications," in *Proc. Conf. ULSI Technol. XIII*, 1997, pp. 197–203.

[230] "Email communication with Dr. Takeshi Nogami, IBM (US)."

[231] C. Adelmann *et al.*, "Alternative metals for advanced interconnects," in *IEEE International Interconnect Technology Conference*, 2014, pp. 173–176.

[232] R. Rosenberg, D. C. Edelstein, C.-K. Hu, and K. P. Rodbell, "Copper metallization for high performance silicon technology," *Annual review of materials science*, vol. 30, no. 1, pp. 229–262, 2000.

[233] C. M. Tan and A. Roy, "Electromigration in ULSI interconnects," *Materials Science and Engineering: R: Reports*, vol. 58, no. 1–2, pp. 1–75, Oct. 2007.

[234] J. W. McPherson, *Reliability Physics and Engineering*. Boston, MA: Springer US, 2010.

[235] R. L. de Orio, H. Ceric, J. Cervenka, and S. Selberherr, "The effect of copper grain size statistics on the electromigration lifetime distribution," in *Simulation of Semiconductor Processes and Devices, 2009. SISPAD'09. International Conference on*, 2009, pp. 1–4.

[236] J. R. Black, "Electromigration—A brief survey and some recent results," *IEEE Transactions on Electron Devices*, vol. 16, no. 4, pp. 338–347, 1969.

[237] J. von Hagen, G. Antonin, J. Fazekas, L. Head, and H. Schafft, "New SWEAT method for fast, accurate and stable electromigration testing on wafer level," in *Integrated Reliability Workshop Final Report, 2000 IEEE International*, 2000, pp. 85–89.

[238] B. J. Root and T. Turner, "Wafer Level Electromigration Tests for Production Monitoring," in *23rd International Reliability Physics Symposium*, 1985, pp. 100–107.

[239] Y. Murakami, J. Li, and T. Shimoda, "Highly conductive ruthenium oxide thin films by a low-temperature solution process and green laser annealing," *Materials Letters*, vol. 152, pp. 121–124, Aug. 2015.

[240] "imec internal data."

[241] R. Dimmich and F. Warkusz, "Electrical conductivity of thin wires," *Active and passive electronic components*, vol. 12, no. 2, pp. 103–109, 1986.

[242] G. C. Schwartz and K. V. Srikrishnan, Eds., *Handbook of semiconductor interconnection technology*, 2nd ed. Boca Raton, FL: CRC/Taylor & Francis, 2006.

[243] M. H. van der Veen *et al.*, "Damascene Benchmark of Ru, Co and Cu in Scaled Dimensions," in *2018 IEEE International Interconnect Technology Conference (IITC)*, 2018, pp. 172–174.

[244] C. Auth *et al.*, "A 10nm high performance and low-power CMOS technology featuring 3rd generation FinFET transistors, Self-Aligned Quad Patterning, contact over active gate and cobalt local interconnects," in *2017 IEEE International Electron Devices Meeting (IEDM)*, 2017, pp. 29.1.1-29.1.4.

[245] S. Narasimha, "A 7nm CMOS Technology Platform for Mobile and High Performance Compute Application," presented at the IEDM, 2017.

[246] E. Glickman and M. Molotskii, "On the effect of grain boundary segregation on electromigration driving force in thin metal films," *Materials Letters*, vol. 26, no. 1–2, pp. 65–68, 1996.

[247] X.-Y. Liu, C.-L. Liu, and L. J. Borucki, "A new investigation of copper's role in enhancing Al–Cu interconnect electromigration resistance from an atomistic view," *Acta materialia*, vol. 47, no. 11, pp. 3227–3231, 1999.

[248] "Personal communication with Johan Meerschaut."

[249] D. Nečas and P. Klapetek, "One-dimensional autocorrelation and power spectrum density functions of irregular regions," *Ultramicroscopy*, vol. 124, pp. 13–19, Jan. 2013.

[250] M. Raposo, Q. Ferreira, and P. A. Ribeiro, "A guide for atomic force microscopy analysis of soft-condensed matter," *Modern research and educational topics in microscopy*, vol. 1, pp. 758–769, 2007.

[251] S. Dutta *et al.*, "Highly Scaled Ruthenium Interconnects," *IEEE Electron Device Letters*, vol. 38, no. 7, pp. 949–951, Jul. 2017.

[252] "unpublished."

List of Publications

- **S. Dutta**, K. Sankaran, K. Moors, G. Pourtois, S. Van Elshocht, J. Bommels, W. Vandervorst, Z. Tokei, and C. Adelmann, "Thickness dependence of the resistivity of platinum-group metal thin films," *Journal of Applied Physics*, vol. 122, no. 2, p. 025107, Jul. 2017, doi: 10.1063/1.4992089.

- **S. Dutta**, S. Kundu, A. Gupta, G. Jamieson, J. F. G. Granados, J. Bömmels, C. J. Wilson, Z. Tőkei, and C. Adelmann, "Highly Scaled Ruthenium Interconnects," *IEEE Electron Device Letters*, vol. 38, no. 7, pp. 949-951, 2017, doi: 10.1109/LED.2017.2709248

- **S. Dutta**, K. Moors, M. Vandemaele, C. Adelmann, "Finite Size Effects in Highly Scaled Ruthenium Interconnects," in IEEE Electron Device Letters, vol. 39, no. 2, pp. 268-271, Jan 2018. doi: 10.1109/LED.2017.2788889.

- **S. Dutta**, S. Beyne, A. Gupta, S. Kundu, Hugo Bender, S. Van Elshocht, G. Jamieson, W. Vandervorst, J. Bömmels, C. J. Wilson, Z. Tőkei, and C. Adelmann, "Sub-100 nm^2 Cobalt Interconnects," in IEEE Electron Device Letters, vol. 39, no. 5, pp. 731-734, April 2018. doi: 10.1109/LED.2018.2821923. **[Editor's Pick]**

- **S. Dutta**, S. Kundu, L. Wen, G. Jamieson, K. Croes, A. Gupta, J. Bömmels, C. J.Wilson, C. Adelmann, and Z. Tőkei, "Ruthenium interconnects with 58 nm2 cross-section area using a metal-spacer process," in *Proceedings of IEEE International Interconnect Technology Conference (IITC)*, May 2017, pp. 1–3, doi: 10.1109/IITC-AMC.2017.7968937. **[S. C. Sun Best Student Paper]**

- M. Popovici, B. Groven, K. Marcoen, Q. M. Phung, **S. Dutta**, J. Swerts, J. Meersschaut, J. A. van den Berg, A. Franquet, A. Moussa, K. Vanstreels, P. Lagrain, H. Bender, M. Jurczak, S. Van Elshocht, A. Delabie, and C. Adelmann, "Atomic Layer Deposition of Ruthenium Thin Films from (ethylbenzyl)(1-ethyl-1, 4-cyclohexadienyl) Ru: Process Characteristics, Surface Chemistry, and Film Properties," *Chemistry of Materials*, vol. 29, no. 11, pp. 4654–4666, Jun. 2017, doi: 10.1021/acs.chemmater.6b05437.

- L. G. Wen, P. Roussel, O. V. Pedreira, B. Briggs, B. Groven, **S. Dutta**, M. Popovici, N. Heylen, I. Ciofi, K. Vanstreels, F. W. Østerberg, O. Hansen, D. H. Petersen, K. Opsomer, C. Detavernie, C. J. Wilson, S. Van Elshocht, K. Croes, J. Bömmels, Z. Tokei, and C. Adelmann, "Atomic layer deposition of ruthenium with TiN interface for sub-10 nm advanced interconnects beyond copper," *ACS Applied Materials Interfaces*, vol. 8, no. 39, pp. 26119–26125, Oct. 2016, doi: 10.1021/acsami.6b07181.

- F. W. Østerberg, M. L. Witthøft, **S. Dutta**, J. Meersschaut, C. Adelmann, P. F. Nielsen, O. Hansen, and D. H. Petersen, "Hall effect measurement for precise sheet resistance and thickness evaluation of Ruthenium thin films using non-equidistant four-point probes," AIP Advances 8, p. 055206 (2018) doi: 10.1063/1.5010399

- M. De Clercq, K. Moors, K. Sankaran, **S. Dutta**, C. Adelmann, W. Magnus, and B. Sorée, "Resistivity scaling model for metals with conduction band anisotropy," Phys. Rev. Materials vol. 2, no. 3, p. 033801, Mar 2018, doi: 10.1103/PhysRevMaterials.2.033801.

- S. Beyne, **S. Dutta**, O. V. Pedreira, N. Bosman, C. Adelmann, I. De Wolf, Z. Tokei, and K. Croes, "The first Observation of p-type Electromigration Failure in full Ruthenium Interconnects," in *Proceedings of IEEE International Reliability Physics Symposium (IRPS),* Jun 2018, doi: 10.1109/IRPS.2018.8353638

- C. Adelmann, K. Sankaran, **S. Dutta**, A. Gupta, S. Kundu, G. Jamieson, K. Moors, N. Pinna, I. Ciofi, S. Van Eishocht, J. Bömmels, G. Boccardi, C. J. Wilson, G. Pourtois, and Z. Tőkei, "Alternative Metals: From AB Initio Screening to Calibrated Narrow Line Models," in *Proceedings of IEEE International Interconnect Technology Conference (IITC)*, Jun 2018, pp. 154–156, doi: 10.1109/IITC.2018.8456484.

- B. Briggs, C. J. Wilson, K. Devriendt, M. H. van der Veen, S. Decoster, S. Paolillo, J. Versluijs, E. Kesters, F. Sebaai, N. Jourdan, Z. El-Mekki, N. Heylen, P. Verdonck, D. Wan, O. V. Pedreira, K. Croes, **S. Dutta**, J. Ryckaert, A. Mallik, S. Lariviere, J. Bömmels, and Z. T˝okei, "N5 technology node dual-damascene interconnects enabled using multi patterning," in *Proceedings of IEEE International Interconnect Technology Conference (IITC)*, May 2017, pp. 1–3, doi: 10.1109/IITC-AMC.2017. 7968983.

- L. G. Wen, C. Adelmann, O. V. Pedreira, **S. Dutta**, M. Popovici, B. Briggs, N. Heylen, K. Vanstreels, C. J. Wilson, S. Van Elshocht, K. Croes, J. Bömmels, and Z. Tokei, "Ruthenium metallization for advanced interconnects," in *Proceedings of IEEE International Interconnect Technology Conference (IITC/AMC)*, May 2016, pp. 34–36, doi: 10.1109/IITC-AMC.2016.7507651

- A. P. Peter, H. Yu, **S. Dutta**, E. Rosseel, S. Van Elshocht, K. Paulussen, A. Moussa, I. Vaesan, M. Schaekers, "Characterization of ultra-thin nickel–silicide films synthesized using the solid state reaction of Ni with an underlying Si:P substrate (P: 0.7 to 4.0%)," *Microelectronic Engineering*, vol. 157, pp. 52–59, May 2016, doi.org/10.1016/j.mee.2016.02.049

- A. P. Peter, T. Witters, **S. Dutta**, A. Hikavvy, I. Vaesen, S. Van Elshocht, M. Schaekers "Phase analysis and thermal stability of thin films synthesized via solid state reaction of Ni with Si1−xGex substrate," *Microelectronic Engineering*, vol. 149, pp. 46–51, Jan. 2016, doi.org/10.1016/j.mee.2015.09.008